REVIEW ARTICLE | JANUARY 09 2026

Ferroelectric and ferroionic multifunctional quantum sensors: Incursion into applications

Beatriz M. Gomes ; Tomás Prior ; Ângela Freitas ; António B. Vale ; Beatriz A. Maia ; Hugo Lebre ; Manuela C. Baptista ; Raquel Dantas ; M. Helena Braga

Appl. Phys. Rev. 13, 011306 (2026)
https://doi.org/10.1063/5.0251263

Applied Physics Reviews REVIEW pubs.aip.org/aip/are

Ferroelectric and ferroionic multifunctional quantum sensors: Incursion into applications

Cite as: Appl. Phys. Rev. **13**, 011306 (2026); doi: 10.1063/5.0251263
Submitted: 2 August 2025 · Accepted: 18 December 2025 ·
Published Online: 9 January 2026

Beatriz M. Gomes,[1,2,3] Tomás Prior,[1,2] Ângela Freitas,[1,2,3] António B. Vale,[1,2] Beatriz A. Maia,[1,2,3] Hugo Lebre,[1,2] Manuela C. Baptista,[1,2,3] Raquel Dantas,[2,4] and M. Helena Braga[1,2,3,a)]

AFFILIATIONS

[1]Faculty of Engineering, University of Porto, R. Dr. Roberto Frias, s/n, 4200-465 Porto, Portugal
[2]MatER, Materials for Energy Research Laboratory, University of Porto, Portugal
[3]LAETA, Institute of Science and Innovation in Mechanical and Industrial Engineering, R. Dr. Roberto Frias s/n, 4200-465 Porto, Portugal
[4]Department of Chemistry, CICECO-Aveiro Institute of Materials, University of Aveiro, 3810-393 Aveiro, Portugal

[a)]**Author to whom correspondence should be addressed:** mbraga@fe.up.pt

ABSTRACT

Ferroelectric materials are poised to drive the next technological leap through their emergent functionalities, including negative capacitance and resistance, charge accumulation without transport, and spontaneous polarization switching. The discovery of ferroionic material-systems that combine room-temperature ferroelectricity and fast ionic conductivity has opened an unprecedented avenue for multifunctional devices that merge the territories of electronics and ionics. These hybrid materials enable the direct coupling of ionic and electronic order parameters, allowing long-range electrostatic interactions, wireless field communication, and energy transduction across solid–solid and solid–air interfaces. Such capabilities offer potential solutions to long-standing challenges, including the Boltzmann limit in transistor subthreshold operation, voltage amplification without power dissipation, and nonvolatile polarization states with ionic reconfigurability. Beyond conventional applications, ferroionics support a new generation of quantum sensors and adaptive devices, spanning optical, electrical, mechanical, thermal, and magnetic domains. This review provides a comprehensive overview of the conceptual foundations, theoretical frameworks, and experimental progress underlying ferroionic systems, highlighting their role as a bridge between ferroelectrics, solid electrolytes, and correlated quantum materials. Finally, perspectives are offered on how ferroionic coupling may reshape device physics and enable sustainable, self-powered information and energy technologies.

TABLE OF CONTENTS

NOMENCLATURE

AC	Alternating current
AFM	Atomic force microscopy
AFM-IR	Atomic force microscopy-infrared
AgI	Silver iodide
α-IGZO	Amorphous indium gallium zinc oxide
Al	Aluminum
ALD	Atomic layer deposition
Al_2O_3	Aluminum oxide
Au	Gold
B3LYP	Becke's 3-parameter exchange and the Lee–Yang–Parr correlation functional
$Ba_xSr_{1-x}TiO_3$, BST	Barium strontium titanate
bpm	Beats per minute
BNNT	Boron nitride nanotube
BNT	$Bi_{0.5}Na_{0.5}TiO_3$—bismuth sodium titanate
BTO	$BaTiO_3$—barium titanate
c-AFM	Conductive atomic force microscopy
CC	Current collector
CCPS	$CuCrP_2S_6$
CH_3	Methyl
$CH_3NH_3^+$, MA	Methylammonium
CIPS	$CuInP_2S_6$
cKPFM	Contact Kelvin probe force microscopy
CMOS	Complementary metal–oxide–semiconductor
Cr	Chromium
CsFAMAPbBrI	$Cs_{0.05}(FA_{0.83}MA_{0.17})_{0.95}PbI_{3-x}Br$, FA = formamidinium, MA = methylammonium
$CsPbBr_3$	Cesium lead bromide or cesium lead tribromide
Cs_4SnBr_6	Cesium tin(II) bromide
Cu	Copper
Cu^+	Cuprous or copper(I) ion
$CuInP_2S_6$	Copper indium thiophosphate
CVD	Chemical vapor deposition
D	Debye
DC	Direct current
DFT	Density functional theory
E_a	Activation energy
EA^+–$CH_3CH_2NH_3^+$	Ethylammonium
$(EATMA)PbBr_4$	$(EATMA)^+ = A^+$ organic ammonium cation, n = 1 Ruddlesden–Popper perovskite with formula type: A_2PbBr_4
eFBG	Etched fiber Bragg grating
ELF	Electron localization function+
EOM	Electro-optic modulator
EPSC	Excitatory postsynaptic current
E-skin	Electronic skin
ETL	Electron transport layer
eV	Electron-volt
FA^+–$CH(NH_2)_2^+$	Formamidinium ion
$FAPbI_3$	Formamidinium lead triiodide
FBG	Fiber Bragg grating
FeFETs	Ferroelectric field-effect transistors
FeRAM	Ferroelectric random-access memory
FET	Field-effect transistor
FETI	Ferroelectric topological insulator
FGT	FGT or Fe_3GeTe_2 is iron germanium telluride
FTJ	Ferroelectric tunnel junctions
FTO	Fluorine-doped tin oxide
GB	Grain boundaries
Gu	Guanidinium or $[C(NH2)_3]^+$
$GuSnBr_4$	Guanidinium tin tetrabromide
HAADF	High-angle annular dark-field
hBN	Hexagonal boron nitride
H_c	Coercive field
HEC	Hydroxy ethyl cellulose
HfO_2	Hafnium oxide or hafnium dioxide
H_2O	Water
HP	High polarization
HR-TEM	High-resolution transmission electron microscopy
HTL	Hole transport layer
I–V	Current–voltage
I_i^-	Interstitial halide
I_{max}	Maximum current
$I_{max,with\ strain}$	Maximum current with strain
$I_{max,without\ strain}$	Maximum current without strain
α-In_2Se_3	Indium(III) selenide, or just indium selenide or indium sesquiselenide
IPSC	Inhibitory postsynaptic current
IR	Infrared
ITO	Indium tin oxide
$LaNiO_3$	Lanthanum nickel oxide
LCD	Liquid-crystal display
LED	Light-emitting diode
$LiFePO_4$, LFP	Lithium iron phosphate
Li	Lithium
LP	Low polarization
LPFM	Lateral piezo-response force microscopy
LSMO	LSMO or $La_{0.7}Sr_{0.3}MnO_3$ is lanthanum strontium manganese oxide
LTD	Long-term depression
LTM	Long-term memory
LTP	Long-term plasticity
LX	Localized excitons

MA^+–$CH_3NH_3^+$	Methylammonium ion
$MAPbI_3$/ $CH_3NH_3PbI_3$	Methylammonium lead iodide
$MAPbBr_3$	Methylammonium lead bromide
MNIST	Modified National Institute of Standards and Technology
MOS	Metal–oxide–semiconductor
MoS_2	Molybdenite
MXene	Class of two-dimensional inorganic compounds, along with MBorenes, that consist of atomically thin layers of transition metal carbides, nitrides, or carbonitrides
Na	Sodium
NDR	Negative differential resistance
Ni	Nickel
NLO	Non-linear optics
NV	Nitrogen-vacancy
O_2	Oxygen
OCV	Open circuit voltage
OIHPS	Hybrid organic–inorganic halide perovskites
P-E	Polarization-electric field
PAN	Peroxyacyl nitrate
Pb	Lead
PbI_6	Lead(VI) hexa-iodide
$PbTiO_3$, PTO	Lead(II) titanate
Pd	Palladium
PDA	Polydiacetylenes
PDMS	Polydimethylsiloxane
$PdSe_2$	Palladium diselenide
PET	Polyethylene terephthalate
PFBA	perfluorobenzylammonium
PFM	Piezo-response force microscopy
PL	Photoluminescence
PMMA	Poly(methyl methacrylate)
PMN-PT	Lead magnesium niobate-lead titanate
PPF	Paired-pulse facilitation
ppm	parts per million
Pt	Platinum
PTIR	Photothermal induced resonance
PTS	Pyroelectric thermal sensors
PU	Polyurethane
PVA	Polyvinyl acetate
PVDF	Polyvinylidene fluoride
P(VDF-HFP)	Poly(vinylidene fluoride-co-hexafluoropropylene)
PVDF-TrFE	Trifluoroethylene or VF_3
PZT	$Pb(Zr_xTi_{1-x})O_3$–lead zirconium titanate
$(P_2S_6)^{4-}$	Thiophosphate anions
rGO	Reduced graphene oxide
RIU	Refractive index unit
S	Spin
SAED	Selected area electron diffraction
Sb	Antimony
SEM	Scanning electron microscopy
SG	Source–gate
SHG	Second harmonic generation
Si-MRR	Silicon microring resonator
SKP	Scanning Kelvin probe
$SnSe_2$	Tin(IV) selenide
SPP	Surface plasmon polariton
$SrTiO_3$, STO	Strontium titanate
STDP	Spike-time-dependent plasticity
STM	Short-term memory
STP	Short-term plasticity
SWIR	Short-wave infrared
T_c	Curie temperature
TCR	Temperature coefficient of resistance
TE	Transverse electric mode
TEM	Transmission electron microscopy
TER	Tunneling electroresistance
TGA	Thermogravimetric analysis
Ti	Titanium
TMA–$(CH_3)_3NH^+$	Trimethylammonium
TMC	Transition metal chalcogenides
TMDs	Transition metal dichalcogenides
TMP	Trimethylphosphanium
TOF-FLI	Time-of-flight fluorescence lifetime imaging
TOF-SIMS	Time-of-flight secondary ion mass spectrometry
V_{cpd} (in Volt)	Work function from contact potential difference
vdW	van der Waals
V_I^+	Iodide vacancies
v-MoS_2	Vertically grown MoS_2
VSe_2	Vanadium diselenide
WS_2	Tungsten disulfide
WSe_2	Tungsten diselenide
WTe_2	Tungsten ditelluride
X	Halide anion
ZnS	Zinc sulfide
ZrO_2	Zirconium oxide or zirconium dioxide
1D-CNN	One-dimensional convolutional neural network
1T undistorted, non-ferroelectric	Undistorted, non-ferroelectric. A trigonal (tetragonal coordination) polymorph of MoS_2 with octahedral coordination of the Mo atoms. This is different from the more common 2H phase, which has trigonal prismatic coordination
1T'distorted, non-ferroelectric	A distorted version of the 1T phase where Mo atoms shift to form zigzag chains. This phase often shows properties like topological behavior or charge density waves but retains inversion symmetry, so it is not ferroelectric
1T" further distorted, ferroelectric	A further distortion of the 1T′ structure. This distortion breaks inversion symmetry, which is a required condition for ferroelectricity. Therefore, 1T″-MoS_2 is ferroelectric
2D	Two-dimensional
2DS	2D semiconductor
2H	Hexagonal crystal phase

3D	Three-dimensional
3R	Rhombohedral crystal phase
6-31G*	B3LYP hybrid functional with the 6-31G Gaussian basis set

I. INTRODUCTION

Ferroelectric materials have attracted considerable attention across materials science, condensed matter physics, and nanodevice community due to their potential for scalable and energy-efficient device applications[1] (Fig. 1). In a crystalline material, ferroelectric polarization arises from the spontaneous alignment of electric dipoles, creating distinct regions separated by domain walls. The structure and energy of these walls are determined by the balance of internal forces. This polarization can be reversed by an external electric field and is lost above the Curie temperature, when the material transitions into a paraelectric state.[2–4] The ferroelectric behavior compares ferromagnetic, responsible for the designation "ferro," which comes from iron, "ferrum" in Latin.

However, at the nanoscale, the polarization behavior becomes significantly more complex. In thin films or materials with mobile defects, polarization is not governed solely by lattice and electronic factors, it is also strongly influenced by ionic motion.[5] Alternatively, ferroelectric materials are not only crystalline, but they are also amorphous.[6] The migration of ions, such as vacancies and interstitials, can locally alter the internal electric field and interact dynamically with ferroelectric polarization.[7]

More recently, ferroionic materials, combining conventional ferroelectric properties with ionic conductivity, have emerged as promising candidates for next-generation technologies. These materials exhibit *ferroionic states*, characterized by the intrinsic coupling between ferroelectric polarization and ionic dynamics at the nanoscale.[8] This interplay leads to complex behaviors, where ionic redistribution and polarization are strongly interdependent. Furthermore, these effects can be actively modulated by external stimuli such as electric fields and electrochemical bias.[9]

Understanding this coupling is crucial for future applications, as it determines the stability, switching behavior, and reliability of energy harvesting and storage devices based on these materials.

Ionic mechanisms in ferroionic materials refer to the role of ions (both cations—positive charges—and anions—negative charges) in determining the polarized states of ferroelectric materials.[10] The ionic transport mechanism in ferroionic materials, as described by Morozovska *et al.*,[11] is primarily driven by the mobility of surface ionic charges and their strong coupling with the bulk ferroelectric polarization.

One of the most extensively studied ferroionic is $CuInP_2S_6$ (CIPS). In this compound, the mobile Cu^+ ions play a key role in its ferroelectric behavior. The migration of Cu^+ ions between the weakly bonded van der Waals layers induces local dipoles, contributing to the spontaneous polarization characteristic of ferroelectricity in CIPS.[7] As in an electrolyte, the rate of ion migration depends on the activation energy E_a, which is the minimum energy required for ions to move through the material, Eq. (1). The ionic conductivity $\sigma(T)$ is, therefore,

$$\ln[\sigma(T)] = \ln\sigma_0 - \frac{E_a}{k_B T}, \tag{1}$$

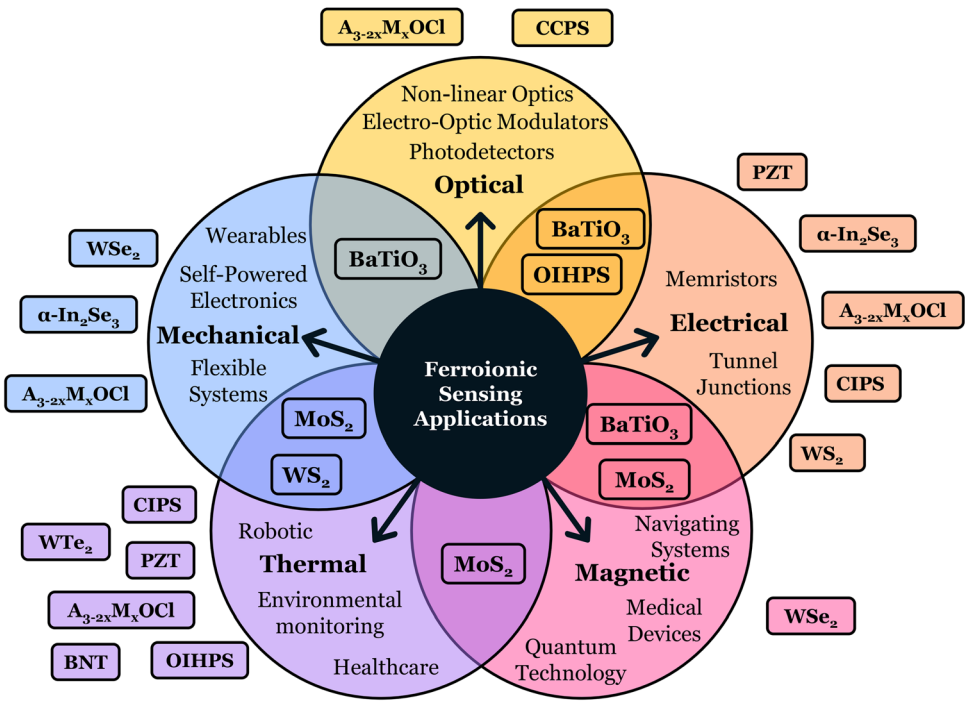

FIG. 1. Schematics representative of ferroionics quantum sensing, its applications in thermal, magnetic, electrical, optical, and mechanical devices, and corresponding main active materials. $A_{3-2x}M_xOCl$ (A = Li, Na, K; M = Mg, Ca, Sr, Ba; $0 \leq x \leq 0.1$); BNT: $Bi_{0.5}Na_{0.5}TiO_3$; CIPS: $CuInP_2S_6$ CCPS: $CuCrP_2S_6$; OIHPS: hybrid organic–inorganic halide perovskites; PZT: $Pb(Zr_xTi_{1-x})O_3$. Schematics designed for this study.

where σ_0 is the ionic conductivity at "infinite" temperature, k_B is the Boltzmann constant, and T is the absolute temperature. With rising temperature, more ionic carriers gain enough energy to overcome the activation barrier, increasing conductivity.[12]

The charge polarization varies upon applying an electric field, leading to charge separation. This effect can alter how ions and electrons move throughout the material. As shown by Sanchez *et al.*, induced electronic polarization can significantly impact ionic conduction, creating a two-way interaction that adds another layer of tunability for sensing applications[13] and eventually leading to the amorphization of the ferroionic.

Remnant polarization is the residual electric polarization left in a material after the external field is turned off; it will likely influence how ions move inside the material, which directly impacts the sensitivity and behavior of ferroionic quantum sensors.[14]

Another layer of control comes from defect chemistry with the intentional introduction or manipulation of imperfections like vacancies in the material's structure. These defects can be engineered to adjust both ionic and electronic properties.[15,16] This means ferroionics conductivity, sensitivity, and even long-term stability can be fine-tuned.[15] Finally, the interplay between dielectric and electrochemical properties provides an extra degree of flexibility. Morozovska *et al.* suggested this coupling allows for sensors that can adapt to changing environmental conditions while maintaining high performance and precision.[17]

Due to the interplay of electrical, ionic, thermal, and mechanical responses, ferroionic materials are promising candidates for multifunctional sensing applications.[18] A deep understanding of how these coupled mechanisms influence each other is essential for advancing next-generation ferroionic quantum sensors.

This study presents a state-of-the-art review of ferroelectric and ferroionic materials. It begins with an overview of the theoretical concepts required to understand their behavior. The discussion then moves to materials of interest, starting with some of the most promising van der Waals compounds, including MoS_2, WTe_2, and $CuInP_2S_6$ (CIPS), followed by a review of perovskites, which include $BaTiO_3$ and hybrid organic-inorganic compounds like $MAPbI_3$. The review continues with an analysis of an emerging class of amorphous electrolytes, $A_{3-2x}M_xOCl$, where $A = Li^+$, Na^+, or K^+, and $M = Mg^{2+}$, Ca^{2+}, Sr^{2+}, or Ba^{2+}, highlighting their ferroionic nature. Following this material overview, a section on quantum sensors, their applications, and performance divided into the optical, electrical, mechanical, thermal, and magnetic fields is presented (Fig. 1, Table I).

II. FERROELECTRIC AND FERROIONIC MATERIALS FOR QUANTUM SENSING

To date, the majority of commercially available ferroelectric devices is based on $Pb(Zr_xTi_{1-x})O_3$, PZT. In 1999, Fujitsu commercialized the first integrated circuits with an embedded ferroelectric random-access memory, with PZT.[19,20] However, as device dimensions continue to shrink, conventional ferroelectrics such as PZT exhibit pronounced size-dependent depolarization effects, resulting in a significant reduction or complete loss of polarization at thicknesses below ~130 nm.[21]

Zirconium and Hafnium oxides are of the group IV of the transition metal oxides with widespread technological relevance.[22] ZrO_2 is a stable ceramic with a dielectric constant of approximately $\varepsilon_r \approx 16$ and low leakage current, making it suitable for MOS devices.[22] HfO_2 offers a higher dielectric constant ($\varepsilon_r \approx 20 - 30$), strong thermal and chemical stability, and an orthorhombic ferroelectric phase crucial for non-volatile memories such as FeFETs and CMOS components. Gomes *et al.*[22] comparative simulations and experiments show that ZrO_2 responds by equalizing with different interfacial Fermi levels, favoring energy-storage applications, whereas HfO_2 (in powder) displays polarization consistent with its ferroelectric nature.[22] Temperature-dependent conductivity and Hall effect measurements reported by the authors showcased polaronic and defect-mediated transport in both oxides, with thermal transitions linked to carrier activation and internal reorganization.

In 2011, Böscke *et al.* reported the discovery of ferroelectricity in ultrathin films of HfO_2, placing this material as promising alternative to traditional ferroelectrics.[23] In HfO_2 ferroelectrics, the ferroelectric properties strongly depend on the concentration of oxygen vacancies, which are the most common intrinsic defects in hafnium oxide.[24] Oxygen vacancies play a key role in stabilizing specific polymorphs and thereby shaping the resulting ferroelectric behavior of HfO_2.[24] Moreover, the switching speed and endurance of ferroelectric memory devices are closely linked to the concentration and redistribution of oxygen vacancies.[24] Since the first report of ferroelectricity in thin films of HfO_2, numerous HfO_2-based ferroelectrics have been demonstrated. By fabricating a 50 nm $HfO_2/ZrO_2/HfO_2$ multilayer using atomic layer deposition (ALD), Yan *et al.* reported the thickest ferroelectric HfO_2-based stack reported to date.[25] The authors propose that the polar phase induced in the otherwise paraelectric ZrO_2 layer helps stabilize the ferroelectric phase in HfO_2.[25] The film achieves a remanent polarization of 9 $\mu C\,cm^{-2}$ and exhibits accelerated wake-up behavior, the increase in ferroelectric polarization that occurs after initial electric-field cycling, attributed to its higher breakdown strength.[25] Li *et al.*[26] showed that ferroelectric switching in HfO_2–ZrO_2 systems can be optimized by varying the ZrO_2 ratio.[26] Devices with lower ZrO_2 content exhibited a higher coercive field yet a shorter switching time, with the switching times decreasing by a factor of 10 while the strength of the coercive field increased by only ~37%.[26] This effect was explained by the lower uniformity of local fields in materials with lower ZrO_2 content, according to an inhomogeneous field mechanism model.[26]

The use of HfO_2-based ferroelectrics offers several advantages, as these materials are fully compatible with silicon and CMOS technologies while maintaining robust ferroelectricity even at thicknesses below 10 nm.[27] Furthermore, their compatibility with deposition techniques such as ALD enables the fabrication of uniform, conformal, and scalable ferroelectric films suitable for advanced three-dimensional device architectures.[21] Reflecting this potential, GlobalFoundries has recently reported ongoing development of HfO_2-based FeFETs with the goal of future commercialization.[27]

The future of FeFETs and FeRAM is closely linked to the integration of ferroionic materials, with lot of research being done in the lab and at pilot scale. In the following subsection, we explore the main classes of ferroelectric and ferroionic materials (Table I), beginning with a discussion of layered van der Waals materials and perovskite structures.

A. Layered van der Waals materials

Van der Waals (vdW) materials consist of atomic layers held together by weak interlayer forces. They can be considered two-dimensional (2D). These layers interact across vdW gaps, defined

TABLE I. Map of the ferroelectric and ferroionic nature of the materials discussed in this study. Symbol correspondence: optical; electrical; mechanical; thermal; and magnetic applications.

Designation	Material	Ferroelectric	Induced ferroelectricity	Ferroionic	Induced ferroionic	Ref.
Layered van der Waals	MoS_2		✓			28
	WS_2		✓			29
	WTe_2	✓				30
	WSe_2		✓			31, 32
	CIPS $CuInP_2S_6$	✓		✓		33, 34
	CCPS $CuCrP_2S_6$	✓			✓	35, 36
Inorganic perovskites	BTO $BaTiO_3$	✓			✓	37, 38, 39
	PZT $Pb(Zr_xTi_{1-x})O_3$	✓				40, 41
Organic inorganic halide perovskites (OIHPS)	$MAPbI_3$	✓		✓		42
Glassy and antiperovskite	$A_{3-2x}M_xOCl$	✓		✓		6

as the shortest distance between adjacent planes. Such materials have emerged as a powerful platform for exploring novel physical phenomena beyond the capabilities of traditional three-dimensional crystals.[30]

While early research was centered around graphene due to its exceptional charge mobility and mechanical strength, the absence of a bandgap in pristine graphene limited its application in conventional electronics. This challenge spurred a broader search for layered

materials with tailored properties, particularly those that could support switchable electrical polarization.[30]

In this context, ferroelectricity in 2D van der Waals (vdW) materials has emerged as a rapidly expanding and exciting field of research.[30]

Ferroelectric materials, exhibiting spontaneous electric polarization, can switch between two or more stable states due to broken inversion symmetry in the crystal lattice.

Although vdW ferroelectrics share the same fundamental polarization mechanisms as conventional ferroelectrics, their phase transition dynamics allow for classification into displacive, order–disorder, or mixed-type ferroelectricity.[43] A key distinction lies in the source of polarization: while conventional ferroelectrics typically rely on bulk lattice distortions, vdW ferroelectrics often derive polarization from interlayer effects, such as sliding ferroelectricity—a mechanism in which polarization arises from the relative displacement between stacked atomic layers. Structural differences further distinguish vdW ferroelectrics from traditional ones. Van der Waals ferroelectrics possess layered architectures with strong in-plane covalent bonds and weak interlayer vdW interactions.[43] In contrast, conventional ferroelectrics, such as oxide-based and polymer-based materials, exhibit rigid three-dimensional crystal lattices, characterized by strong ionic or covalent bonding throughout the structure.

Another significant advantage of vdW ferroelectrics is their robustness against depolarization fields. These fields are generated by unscreened bound charges at interfaces, producing an internal electric field that opposes the material's polarization. In conventional ultrathin ferroelectrics, especially perovskite oxides, such depolarization fields are known to strongly suppress ferroelectricity. However, vdW ferroelectrics demonstrate excellent immunity to this effect, enabling the realization of stable ferroelectricity down to the atomic scale.

While still a relatively underexplored frontier, naturally occurring and synthetic vdW materials, robust ferroelectricity can persist down to a few atomic layers, sometimes even at room temperature.[30] These findings are unlocking exciting opportunities for low-power memory devices, reconfigurable logic, and neuromorphic computing, demonstrating that 2D ferroelectrics are not just scientific curiosities, but promising candidates for future nanoelectronic and flexible technologies.[30]

1. Transition metal chalcogenides

Transition metal chalcogenides (TMCs) are compounds of transition or post-transition metals with chalcogen anions (S, Se, Te), forming layered van der Waals crystals, low-dimensional chains, and three-dimensional frameworks with tunable electronic structure, strong light-matter interaction, and rich catalytic behavior, which supports applications in optoelectronics, electrochemical energy storage, and infrared nonlinear optics.[44,45]

a. In_2Se_3. Indium Selenide is an example of a layered polymorphic material with two ferroelectric phases (α and γ) and a multiferroic phase (β').[46,47] It consists of a quintuple-layer structure arranged in sequence $Se - In - Se - In - Se$. The interlayer spacing between the central Se layer and the adjacent In layers is unequal, breaking inversion symmetry. Ferroelectricity in $\alpha - In2Se3$ originates from the displacement of the central Se layer (Fig. 2). This enables the simultaneous reversal of both out-of-plane and in-plane polarization

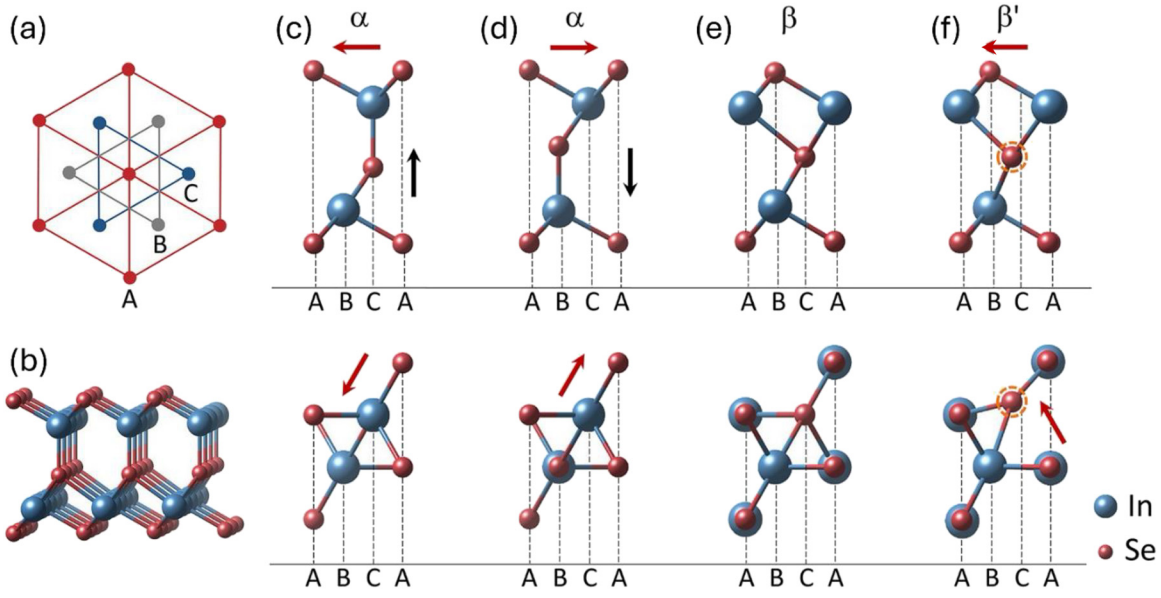

FIG. 2. Structures of 2D In_2Se_3 obtained by first-principles simulations. (a) Top view of the crystal structure of monolayer In_2Se_3. Each layer of In_2Se_3 contains only one element, and the atoms in each layer are located at one of the A, B, and C sites. (b) 3D structure of α phase with upward polarization. (c)–(f) Side and top views of ferroelectric α phase with different polarizations, paraelectric β phase, and distorted β' phase, respectively. The red and black arrows mark the directions of in-plane and out-of-plane polarizations, respectively. Reproduced with permission from Huang *et al.*, InfoMat **4**, e12341 (2022). Copyright 2022 Author(s), licensed under a Creative Commons Attribution (CC BY 4.0) license.

in a coupled manner. The coordinated switching is driven by a lateral shift of the Se atoms, which alters their interlayer spacing with neighboring In atoms in both directions,[48] (Fig. 2). The transition between phases can be achieved by both the choice of synthesis route and external factors such as temperature, electric fields, light, and strain.[46] In this way, the ferroelectric, piezoelectric, and ferroelastic properties of the material can be tuned by external stimuli.

Tang *et al.*[49] reported that the strength and orientation of spontaneous polarization and optical absorbance of the ferroelectric $\beta - In_2Se_3$ monolayer were significantly influenced by the applied strain on the material.[49] With polarization magnitudes higher than typical values for $\alpha - In_2Se_3$, Xu *et al.*[50] showed that the antiferroelectric distortion in $\beta' - In_2Se_3$ produced a strain on the few-layers thick material, demonstrating the presence of ferroelastic domains.[50] On a different approach, He *et al.*[51] explored the mediation of the ferroelectric behavior in α-In_2Se_3 by proton insertion. This unexpected behavior was explained by the formation of metastable H^+-In_2Se_3 phases that retained the polar behavior of the original material.[51] Recently, Long *et al.*[52] have identified the presence of a previously unknown regime where both ferroelectricity and defect migration regulate the switching behavior of $\beta' - In_2Se_3$. They highlight that by controlling the Se vacancy rates through synthesis variation or postgrowth doping, the polarity of the material can be tuned.[52] Together, these works show distinct ferroionic behavior in In_2Se_3 and highlight the potential for extrinsic and intrinsic ion migration to be a viable way of modulating ferroelectric properties.

Transition metal dichalcogenides (TMDs) are a class of layered materials (Fig. 3) with the general formula MX_2, where M is a transition metal from groups 4, 5, or 6 of the periodic table and X is a chalcogen element (such as sulfur, selenium, and tellurium). These materials share a structural similarity with graphite, consisting of weakly bonded layers that allow for easy separation. Individual TMD layers can be isolated from the bulk material through techniques such as mechanical exfoliation, liquid-phase exfoliation, and ion intercalation.

b. MoS_2 (Table I). Molybdenite (MoS_2) is a widely abundant 2D material that, in its 2H polytype, consists of layers stacked in an ABA manner, with high-quality, large crystals readily available. Bulk MoS_2 is an n-type semiconductor with an indirect bandgap of approximately 1.3 eV, which transitions to a direct bandgap of 1.85–1.90 eV when reduced to a single layer.[53] Additionally, a monolayer MoS_2 exhibits high carrier mobility (40–120 $cm^2V^{-1}s^{-1}$ at room temperature)[54] and a large on/off ratio, making it highly suitable for field-effect transistors (FETs). It also demonstrates high photoresponse (up to ~1000 A/W)[55] and exceptional mechanical resilience, with a breaking strain of 6%–11%.[56] Despite MoS_2 not being a naturally occurring ferroelectric, ferroelectric properties can be engineered (Fig. 3). Lipatov *et al.*[57] reported the first direct experimental observation of ferroelectricity in two-dimensional (2D) 1T″-phase MoS_2, a previously unconfirmed property despite theoretical predictions. The metastable 1T″ phase was synthesized from the common 2H phase via chemical lithiation and verified its non-centrosymmetric P3m1 crystal structure, which supports out-of-plane spontaneous polarization.[57] Using scanning probe microscopy techniques, it was demonstrated that this polarization can be mechanically switched—via local pressure from an AFM tip—thanks to the flexoelectric effect. First-principles calculations confirmed the polar structure and predicted semiconducting behavior in monolayers and metallicity in multilayers, classifying 1T″-MoS_2 as a rare *polar metal*.[57] Meng *et al.*[28] reported sliding induced multiple polarization states in 2D MoS_2 (Fig. 3, Table I). This study demonstrates that sliding ferroelectricity in rhombohedral (3R) MoS_2 enables multiple stable polarization states, a mechanism distinct from conventional ion-displacement ferroelectricity.[28] Using dual-gate FET and density functional theory (DFT) simulations, the researchers show that while bilayer 3R MoS_2 exhibits conventional binary polarization, multilayer structures (three or more layers) reveal intermediate polarization states due to sequential interfacial dipole switching.[28] A generalized model is proposed, showing that the number of stable polarization states scales exponentially with layer number, offering a new strategy for designing multistate, high-temperature, and robust ferroelectric devices based on two-dimensional materials.

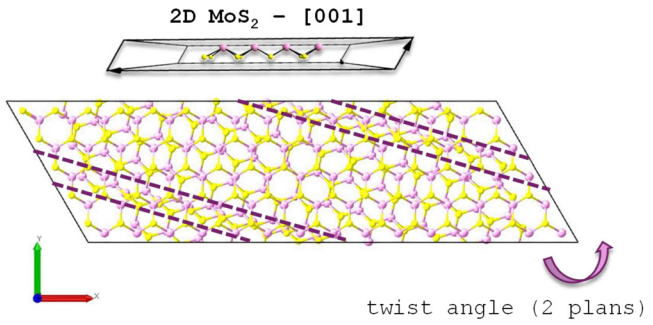

FIG. 3. Symmetry breaking mechanism to polarize MoS_2 planes, inducing ferroelectricity. Schematics obtained for this study.

c. WS_2. WS_2 is an n-type semiconductor with an indirect bandgap of approximately 1.3 eV.[58] When thinned down to a single layer, it transitions to a direct bandgap semiconductor with a bandgap of ~2 eV.[58] This material has attracted significant attention for spin-orbitronics applications due to its exceptionally strong spin–orbit coupling, with the valence band of monolayer WS_2 exhibiting a spin–orbit splitting of approximately 420 meV, nearly three times greater than that of monolayer MoS_2 (~150 meV).[59–61] Similar to MoS_2, this material does not inherently exhibit ferroelectricity in its bulk monolayer form. However, sliding ferroelectricity has already been reported for this material (Fig. 3, Table I). Molino *et al.* reported ferroelectric switching for a marginally twisted bilayer, demonstrated by scanning tunneling microscope at room temperature.[29] Sliding ferroelectricity in 3R MoS_2 enables multiple stable polarization states by interlayer sliding, unlike conventional ferroelectric mechanisms.[29] Through experiments and DFT simulations, it reveals that while bilayers show binary switching, multilayer structures exhibit intermediate states due to sequential dipole flipping.[29] A generalized model shows that the number of stable states increases exponentially with layer count, suggesting a new approach for developing multistate, high-temperature, and reliable ferroelectric devices using 2D materials.

d. WTe_2 (Table I). WTe_2 belongs to the family of TMDs and naturally crystallizes in a non-centrosymmetric orthorhombic structure with a polar space group $Pmn2_1$.[30] Unlike most TMDs, which are typically semiconductors, WTe_2 exhibits Weyl semimetal behavior in its

native crystal phase. A Weyl semimetal is a class of topological quantum materials in which the conduction and valence bands intersect at discrete points in momentum space known as Weyl nodes.[30] Around these nodes, electrons behave as Weyl fermions, massless, chiral quasiparticles originally predicted in high-energy physics.[30] In addition to its topological properties, WTe_2 has been identified as a rare example of a metallic material exhibiting ferroelectricity, a *polar metal*, making it a member of a small but growing group of ferroelectric Weyl semimetals.[30] This is particularly intriguing because ferroelectricity and metallicity are traditionally considered mutually exclusive: in metals, the presence of free electrons typically screens internal electrostatic fields, suppressing the long-range dipole ordering required for ferroelectricity. The latter ferroelectrics were previously designated as "polar metals" as referred to previously herein.[62–64] However, in WTe_2, ferroelectric-like polarization persists, likely due to its low carrier density and strong lattice asymmetry, challenging conventional understanding and opening new avenues in topological and ferroic material research. Finally, ferroelectric domains in WTe_2 thin films have been experimentally observed using PFM.[30]

e. WSe_2 (Table I). WSe_2 is a p-type semiconductor with an indirect bandgap of ~1.3 eV. Monolayer WSe_2 has a direct bandgap. WSe_2 is not intrinsically ferroelectric in its natural state, but can exhibit ferroelectric-like properties under engineered conditions, especially in heterostructures or when influenced by external fields or strain. Hassan *et al.*[31] reported twist-controlled ferroelectricity in WSe_2 bilayers. This study demonstrates that bilayer WSe_2 exhibits room-temperature ferroelectricity when the layers are twisted within a small angle range ($0° < \theta < 3°$) (Fig. 3, Table I), which vanishes for $\theta \geq 4°$, due to a commensurate-to-incommensurate transition in moiré superlattices.[31] The twist angle controls inversion symmetry breaking and enables the formation of electrically switchable dipoles, confirmed via hysteresis in transport measurements. Zhou *et al.* reported enhanced polarizability and tunable diamagnetic shifts from charged localized emitters in WSe_2 on a relaxor ferroelectric.[32] This study demonstrates that charged localized excitons (LXs) in monolayer WSe_2, when placed on a relaxor ferroelectric substrate (PMN-PT), exhibit highly enhanced polarizability and strong coupling to local ferroelectric domains.[32] This interaction enables a giant quantum-confined Stark effect (shifting and splitting of atomic or molecular energy levels), significant energy tunability, and strain-dependent modulation of optical and magnetic properties, including diamagnetic shift and g-factor—all under extremely small strain variations (~0.05%).[32] Unlike neutral excitons, the charged LXs display nonzero and strain-tunable circular polarization even at zero magnetic field, highlighting their sensitivity to local electric fields and spin-valley dynamics.

2. Transition metal thiophosphates

a. CIPS (Table I). Copper indium thiophosphate (CIPS) is part of the transition metal thiophosphate family, $Cu^{I}M^{III}P_2S_6$ (M^{III} = In, Cr, or V), recognized for its vdW layered structure (Fig. 4).[7] These compounds typically consist of metal cations embedded in thiophosphate anions $(P_2S_6)^{4-}$, with general formulas including $M^{4+}[P_2X_6]^{4-}$ $[M^{2+}]_2[P_2X_6]^{4-}$, and $M^{1+}M^{3+}[P_2S_6]^{4-}$.[7] Maisonneuve *et al.*[65] determined the crystal structure of CIPS at room temperature, confirming a monoclinic symmetry with a layered vdW configuration. Structurally,

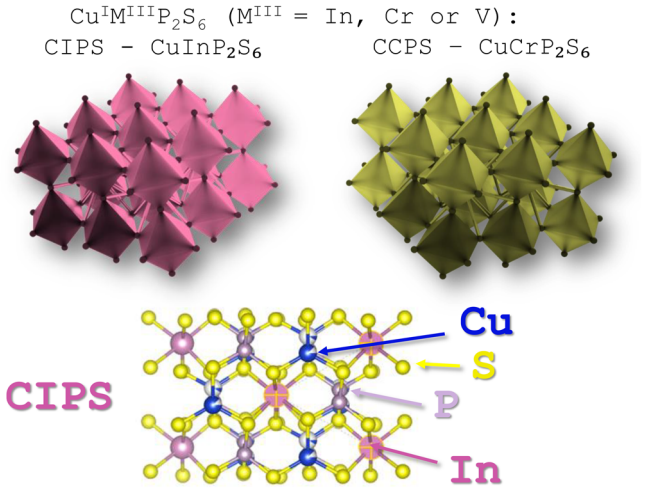

FIG. 4. Crystal structures of CIPS and CCPS. These compounds typically consist of metal cations embedded in thiophosphate anions $(P_2S_6)^{4-}$, with general formulas including $M^{4+}[P_2X_6]^{4-}$ $[M^{2+}]_2[P_2X_6]^{4-}$, and $M^{1+}M^{3+}[P_2S_6]^{4-}$ (M^{III} = In, Cr, or V).[7] Schematics designed for this study.

it resembles compounds of the $Cu^{I}M^{III}P_2S_6$ type, featuring a dense sulfur framework in an ABC stacking sequence.[7] Within this framework, Cu^+, In^{3+}, and P–P pairs occupy octahedral voids, forming a network of alternating CuS_6, InS_6, and P_2S_6 units (Fig. 4).[65] The ability of Cu^+ and In^{3+} ions to shift vertically within these octahedra induces spontaneous electric dipole moments, originating from out-of-plane ferroelectric behavior. Due to weak interlayer coupling and variations in Cu^+ and P–P positions between adjacent layers, the full unit cell of CIPS includes two stacked layers to capture its true symmetry.[65]

CIPS exhibits room-temperature ferroelectricity, characterized by spontaneous electric polarization in the absence of an external electric field (Fig. 5).[7] This behavior was first confirmed by Simon *et al.* in 1994, using a combination of x-ray diffraction, calorimetry, and dielectric measurements.[33] Based on their findings, the Curie temperature (T_c) of CIPS was determined to be approximately 315 K (42 °C).[33] Below this threshold, the material exhibits ferroelectric behavior, while above it, it transitions into a paraelectric state, losing its spontaneous polarization. Since its discovery, several strategies have been employed to increase the Curie temperature of CIPS. These include applying hydrostatic pressure, which raises T_C to approximately 360 K (87 °C);[66–68] developing indium-rich compositions, achieving T_C = 330 K (57 °C);[69] and inducing chemical phase separation, resulting in a T_c of approximately 338 K (65 °C).[70] These findings demonstrate that the ferroelectric behavior of CIPS's is tunable through both compositional adjustments and external stimuli (Fig. 5).

As expected, CIPS also displays ionic conductivity, Eq. (1), due to the movement of Cu^+ ions across the layers [Fig. 5(e)].[65] In crystal CIPS, Cu^+ ions are not in centro-symmetric positions; instead, there is an out-of-plane order phenomenon, which leads to spontaneous polarization and the formation of ferroelectric phases (Fig. 5).[7] The origin of ferroelectricity in CIPS lies in the displacement instability of Cu^+ ions. These ions shift asymmetrically within the sulfur-centered octahedral voids, generating intrinsic dipole moments. This same displacement mechanism is also responsible for CIPS' Cu^+ ions long-range

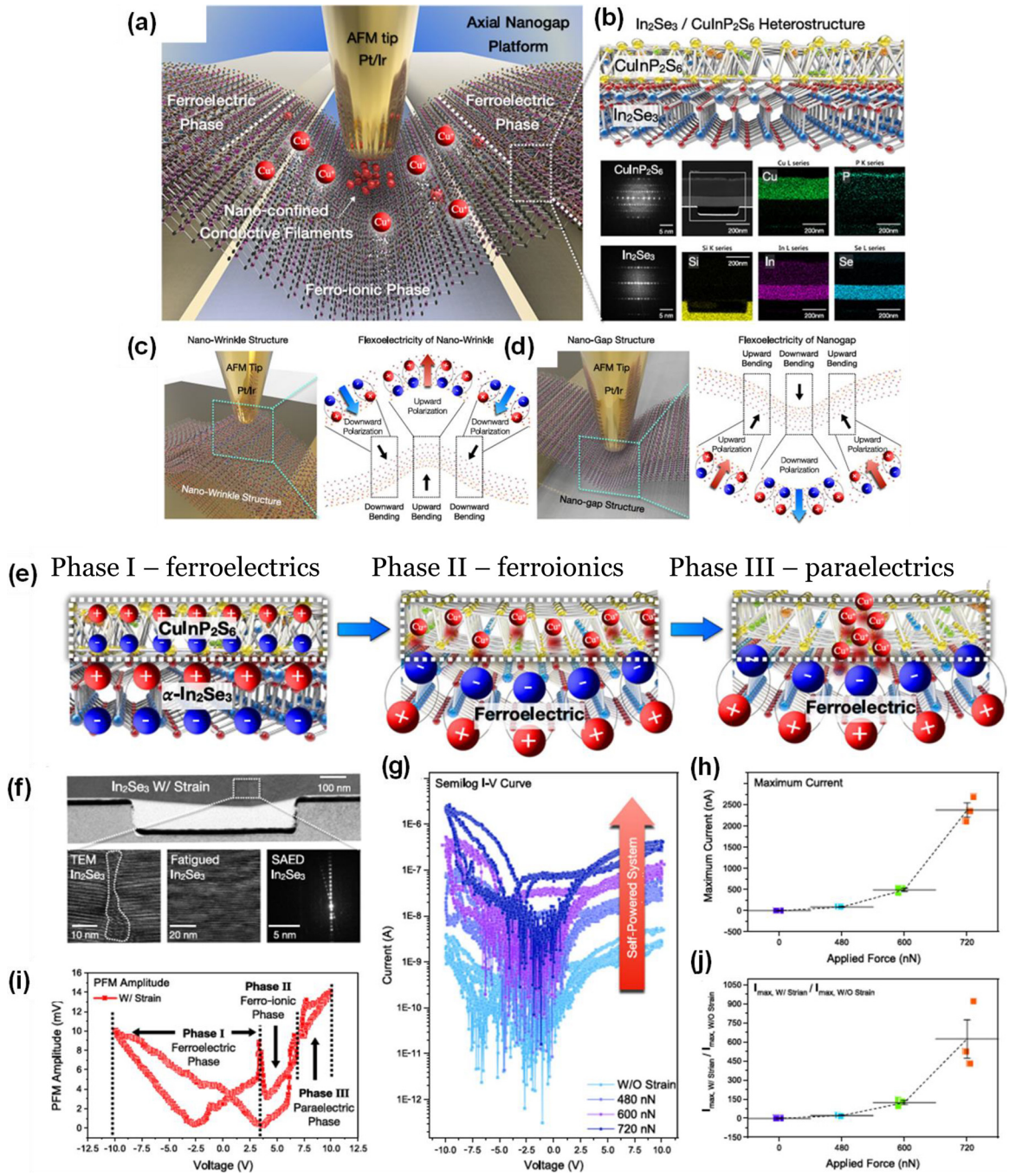

FIG. 5. Universal axial nanogap platform for programmable flexoelectric engineering. (a) Schematic illustration of a free-standing 2D ferroionic memristor designed for spatial confinement of conductive filaments. (b) Free-standing 2D α-In_2Se_3/$CuInP_2S_6$ heterostructure, along with its cross-sectional transmission electron microscope TEM image and selected area electron diffraction (SAED) mapping. Local domain mapping highlights flexoelectric behavior and strain distribution. Schematics illustrate local strain-induced flexoelectric fields: (c) in a nanowrinkle structure and (d) in a nanogap region. Self-powered 2D ferroionic conduction via spatial flexoelectric nanomanipulation. (e) Ferroelectric, ferroionic, and paraelectric phase transition mechanism in the α-In_2Se_3/$CuInP_2S_6$ heterostructure, demonstrating its potential for flexoelectric energy storage. (f) Cross-sectional TEM image and corresponding SAED pattern of a mechanically bent In_2Se_3 lattice, revealing nanoscale flexoelectric effects. The self-powered ferroionic conduction system is experimentally validated through: (g) Semi-logarithmic I–V characteristics. (h) Distribution of maximum current (I_{max}). (i) Piezoresponse force microscopy (PFM) amplitude hysteresis under nanoscale mechanical bending, indicating a reduced conduction threshold. (j) Ratio of $I_{max,with\ strain}$ to $I_{max,without\ strain}$, demonstrating strain-enhanced conductivity. Reproduced with permission from Lee *et al.*, Nat. Commun. **15**, 5162 (2024). Copyright 2024 Author(s), licensed under a Creative Commons Attribution (CC BY 4.0) license.[18]

migration, especially along the vdW gaps between layers. When the temperature is lower than the T_c, copper ions undergo a jump migration in the metastable state, which is accompanied by a deformable coupling with the thiophosphate anion, resulting in ionic conduction.[7]

Additionally, it is also found that the ionic conductivity of CIPS is related to the dielectric relaxation process. Under the action of an external electric field, the ionic response time inside the material is correlated with the change in the dielectric constant. The direct confirmation of Cu^+ conduction was performed by Zhou *et al.* in 2020 using scanning electron microscopy (SEM) to analyze the composition of a cross-sectioned CIPS capacitor under prolonged direct current stress, and the accumulation of Cu atoms at the cathode interface was observed.[7]

Unlike conventional ferroelectric materials, which typically exhibit a double-well potential associated with two degenerate polarization states, CIPS features a quadruple-well potential.[7,71] This unique characteristic stems from its layered vdW structure, which enables Cu^+ ions to occupy four energetically favorable positions across the layers. The relatively low energy barriers separating these sites give rise to more intricate polarization dynamics and switching behavior.[7,71] These four states are categorized into two low polarization (±LP) and two high polarization (±HP) states, distinguished by their parallel or antiparallel orientations relative to the z-axis.[7,71]

CIPS also shows a negative piezoelectric effect, an uncommon phenomenon where the crystal contracts instead of expanding along the direction of the applied electric field.[72] This contrasts with most ferroelectrics, which exhibit positive longitudinal piezoelectricity. Similar to what has been observed in ferroelectric polymers, like PVDF, theoretical predictions and experimental data suggest that the contraction in CIPS is linked to the large, field-responsive displacement of Cu^+ ions and the associated reduction in lattice dimensions.[72,73] This behavior is thought to be a hallmark of low-dimensional ferroelectrics.

Finally, although most ferroelectrics exhibit polarization aligned with the direction of the applied electric field, CIPS demonstrates anomalous ferroelectric switching. As Neumayer *et al.*[74] reported, in CIPS the polarization can switch against the applied field direction.[74] This counterintuitive behavior is attributed to interlayer Cu^+ migration across vdW gaps, suggesting a strong coupling between ionic mobility and ferroelectric polarization. Such switching dynamics highlights the complex interplay between structure, charge displacement, and ionic transport in CIPS.[74]

b. CCPS (Table I). $CuCrP_2S_6$ (CCPS), a member of the transition metal thiophosphates family, has traditionally been regarded as an antiferroelectric material. However, recent studies suggest that it also exhibits out-of-plane ferroelectricity. Cho *et al.*[35] proposed a procedure to obtain highly tunable ferroelectric and antiferroelectric properties on CCPS. They demonstrated controllable switching of spontaneous polarization via external poling fields, concluding that the observed local ferroelectric behavior and defect-dipole polarization depend on the uniaxial quadruple potential well. The authors highlight, however, the need for direct observation of polarization in nanoscale devices. Lo *et al.*[36] reported the direct observation of polarization states in 2D $CuCrP_2S_6$. Using polarization-electric hysteresis tests showed moderate remnant polarization of 14.97 $\mu C\,cm^{-2}$ and saturation polarization values of 16.05 $\mu C\,cm^{-2}$.[36] The presence of ferroelectric domains was further verified via PFM. An external electric field was applied through conductive PFM tips, effectively writing a phase contrast in CCPS nanoflakes. Second harmonic generation (SHG) nonlinear optical process indicated that the non-centrosymmetric nature of CCPS was responsible for its ferroelectric characteristic. This indirect measure was complemented by direct observation using scanning transmission electron microscopy along with high-angle annular dark-field (HAADF) imaging. These techniques confirmed, through direct observation, that the off-center ordering of Cu ions resulted in non-zero net polarization below the T_c, while this polarization disappeared above T_c. These findings were in agreement with DFT simulations, strengthening the conclusions of the physical measurements. Liu *et al.*[75] demonstrated the out-of-plane ferroelectricity and hysteresis loop of 2D $CuCrP_2S_6$ using PFM. The origin of such behavior was revealed through second harmonic generation (SHG), which showed the presence of a non-centrosymmetric structure due to the shift of Cu^+ ions in the sulfur octahedron.[75]

B. Perovskites

Perovskite oxides follow the general chemical formula ABX_3, where A and B are cations of different sizes, and X is typically an anion, such as oxygen (Fig. 6). Some of the most well-known perovskite oxides include barium titanate ($BaTiO_3$) and lead zirconate titanate (PZT). Lately, hybrid perovskites, which incorporate both organic and inorganic components, have attracted significant attention. A common feature among these materials is their ferroelectric nature, the ability to exhibit a switchable electric polarization under an external electric field.

1. BTO (Table I)

Barium titanate ($BaTiO_3$, BTO) is one of the most widely studied ferroelectric perovskite oxides. In the crystal structure of $BaTiO_3$, barium (Ba^{2+}) ions occupy the corners of the unit cell, titanium (Ti^{4+}) is located at the body center, and oxygen (O^{2-}) atoms sit at the face centers.[76] Under the application of a coercive electric field, the Ti^{4+} ion

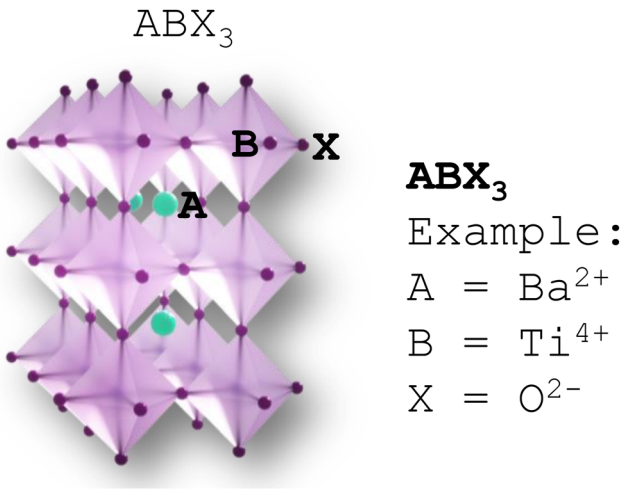

FIG. 6. Schematic structure of a perovskite ABX_3. Schematics designed for this study.

can shift off-center relative to the surrounding oxygen octahedra. Due to the small ionic radius and high positive charge of the Ti^{4+} ion, its off-center displacement within the oxygen octahedron results in the storage of significant potential energy, which underlies the ferroelectric behavior of the material.[76] $BaTiO_3$ exhibits a T_c of approximately 400 K (127 °C), above which it transitions to a paraelectric phase.[76] Strontium titanate ($SrTiO_3$, STO), another perovskite oxide, has a much lower T_c ~105 K (−168 °C) and is thus paraelectric at room temperature.[76] Notably, partial substitution of barium with strontium leads to the formation of barium strontium titanate ($Ba_xSr_{1-x}TiO_3$, BST).[76] The ferroelectric properties of BST can be finely tuned by adjusting the barium-to-strontium molar ratio (x), allowing for tailored dielectric and ferroelectric characteristics suitable for a wide range of applications.[37] These materials are examples of solid solutions formed between $BaTiO_3$ and $SrTiO_3$, and their tunability has made them attractive for use in capacitors, actuators, and other electronic devices.

2. PZT (Table I)

Lead zirconate titanate is a well-known class of ferroelectric perovskites with the chemical formula $Pb(Zr_xTi_{1-x})O_3$. It exhibits tunable T_c and piezoelectric properties, which can be adjusted by varying the Zr/Ti ratio. The T_c typically falls below 673 K (400 °C) and generally decreases with increasing zirconium content.[40] Structurally, PZT adopts the perovskite crystal structure, where lead (Pb^{2+}) ions occupy the corners of the unit cell, oxygen ions are located at the face centers, and titanium (Ti^{4+}) and zirconium (Zr^{4+}) ions reside at the center of the unit cell.[77] Doping PZT with other elements (such as La and Nb) is a common strategy to tailor its properties, including modifying the T_c, enhancing piezoelectric coefficients, and optimizing other electrical characteristics.[40]

3. $MAPbI_3$ (Table I)

In hybrid halide perovskite structure, A is an organic/inorganic cation, B is a metal cation, typically lead (Pb^{2+}) or tin (Sn^{2+}), and X is a halide anion, such as iodine (I-), bromine (Br-), and chlorine (Cl-). The organic cation occupies the A-site, while the metal cation and halide anions form an octahedral framework.[78] The use of organic cations in hybrid perovskites serves several purposes. Organic cations, such as methylammonium ($CH_3NH_3^+$–MA) and formamidinium ($HC(NH_2)_2^+$–FA), are relatively small and can fit within the perovskite lattice without disrupting its structure (Fig. 7).[79] These cations contribute to the material's electronic properties, influencing the bandgap and charge carrier dynamics.[78] The organic component introduces flexibility in tuning the material's optoelectronic characteristics, which is not easily achievable with purely inorganic perovskites.[80]

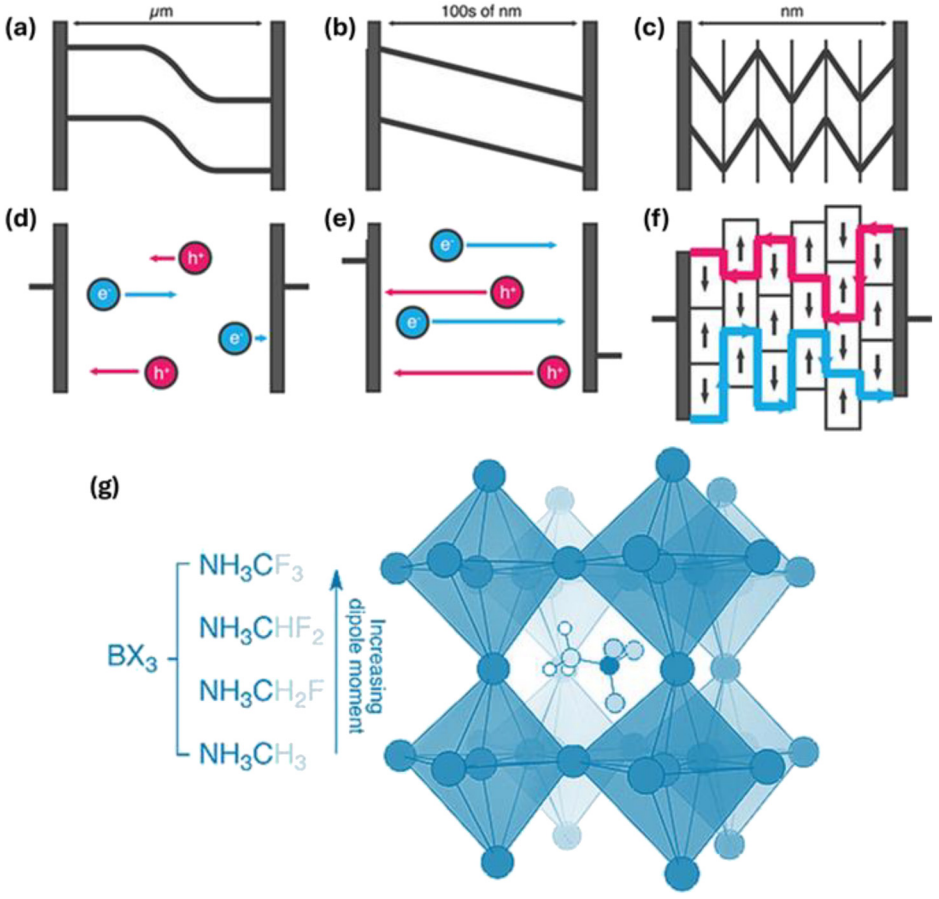

FIG. 7. Schematics of charge separation pathways in different junction types. Illustrations show the one-dimensional built-in potential profiles (top panels) and corresponding two-dimensional charge separation pathways for electrons and holes (bottom panels) in: (a) and (d) a conventional macroscopic p–n junction, (b) and (e) a single-domain ferroelectric thin film, and (c) and (f) a multidomain ferroelectric thin film. In the proposed multidomain ferroelectric structure—relevant for hybrid perovskites—electrons preferentially migrate along potential minima, while holes follow pathways along potential maxima, corresponding to antiphase domain boundaries. (g) Substantial enhancement in dipole moment—from 2.3D to 6.6D (calculated in vacuum using B3LYP/6-31G*)—is observed with increasing levels of methyl-fluorination. Reproduced with permission from Frost *et al.*, Nano Lett. **14**, 2584 − 2590 (2014). Copyright 2014 Author(s), licensed under a Creative Commons Attribution (CC BY 4.0) license.[81]

Hybrid halide perovskites are primarily used in optoelectronic applications, such as solar cells, light-emitting diodes (LEDs), photodetectors, and lasers.[78] Their popularity in these applications stems from their favorable optoelectronic properties, including high absorption, high charge carrier mobility ($25\,cm^2V^{-1}s^{-1}$),[82] and tunable bandgaps.[83] These characteristics make them highly efficient at converting light into electrical energy or vice versa. For example, in solar cells, hybrid perovskites can achieve high power conversion efficiencies due to their ability to absorb a broad range of sunlight and efficiently transport charge carriers.[84] Similarly, in LEDs, their tunable bandgap allows for light emission across a wide range of wavelengths, making them suitable for displays and lighting.[85]

In perovskite solar cells, hysteresis is a commonly observed phenomenon, where the electrical output depends on the direction of the voltage scan and the device's measurement history. This results in discrepancies in the current–voltage (I–V) characteristics, complicating accurate performance evaluation. This variability makes it difficult to compare results across studies or assess the true potential of perovskite solar cells for practical applications.[86] This hysteresis has been attributed to various phenomena, including trapping/detrapping of charges, ferroelectric effects, unbalanced charge transport, and ionic migration.[87–89] While no definitive explanation has been universally accepted, ongoing research continues to explore these mechanisms in detail. In this

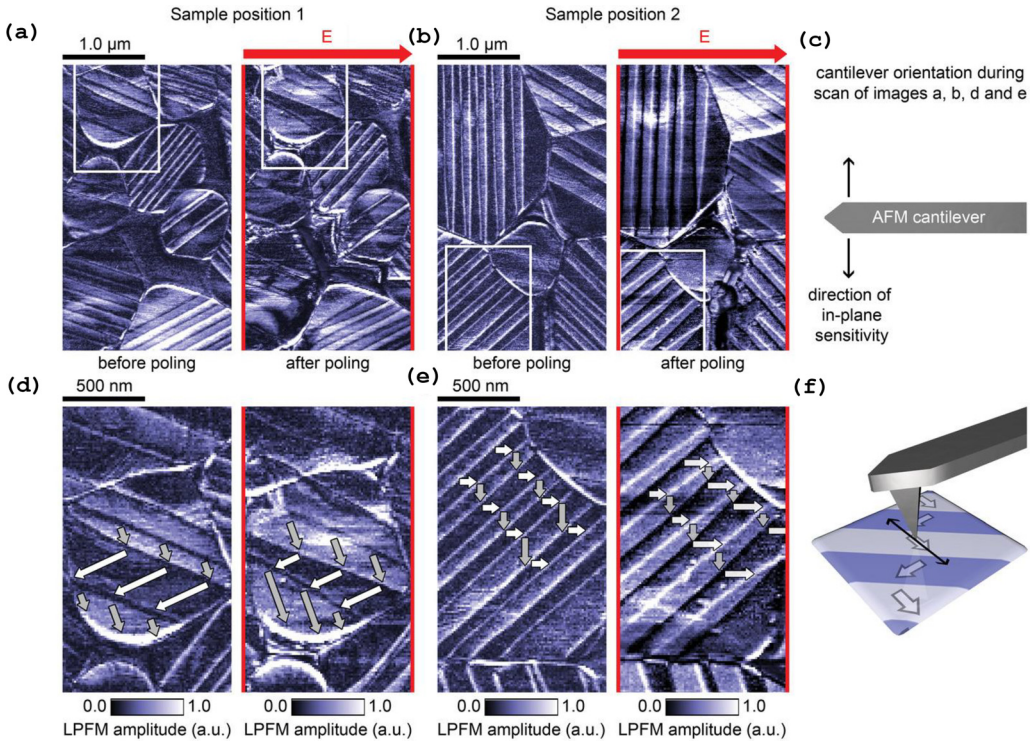

FIG. 8. (a) Lateral piezoresponse force microscopy (LPFM) amplitude images of a $MAPbI_3$ thin film before (left) and after (right) poling. Following poling at $E = +4.5\,V\,\mu m^{-1}$ for 11 min, notable changes in domain size and morphology are observed. (b) Second scanned region exhibits similar domain evolution after poling. (c) Schematic top view of the AFM cantilever orientation during scanning, indicating LPFM sensitivity directions relative to the sample's piezoresponse. (d) and (e) Enlarged views of the white-framed regions in (a) and (b), highlighting domain widening and narrowing induced by poling. Gray and white arrows mark the deduced polarization directions, based on the correlation between LPFM amplitude, cantilever sensitivity, and the applied electric field direction. Arrow lengths correspond to the projected width of each domain along its polarization direction. (f) Diagram illustrating the interaction between the sample's polarization direction and the torsional response of the cantilever (black arrows), which underpins the LPFM signal. (g) Current–electric field (I–E) sweep of a representative $MAPbI_3$ thin film, measured between two laterally aligned Au electrodes forming a 5 μm-wide and 10 mm-long channel, displays Schottky-diode-like behavior. At an onset field of $\pm 1.6\,V\,\mu m^{-1}$, the conductivity increases. When the sweep direction is reversed, the film sustains its enhanced conductivity. (h) During DC poling at $+2\,V\,\mu m^{-1}$ for 10 min, the conductivity initially rises before gradually diminishing to a steady-state current of approximately 120 nA. (i) Following DC poling, the I–E sweeps demonstrate a reduced onset field ($E_{on} = +0.5\,V\,\mu m^{-1}$), and the device effectively blocks charge carriers under reverse bias conditions. (j) Applying a subsequent negative DC poling bias of $-2\,V\,\mu m^{-1}$ results in the sample current rising from -1 to -110 nA within the first 6 min. (k) I–E sweep characteristics are inverted compared with those obtained under forward poling. The schematics beneath each I–E curve illustrate the proposed formation of a net built-in field within the perovskite grains after poling. (l) Illustration of the proposed mechanisms governing the electronic behavior of $MAPbI_3$ thin films: the schematic depicts the interplay between ferroelectric polarization within perovskite grains, ionic and electronic screening charges, grain boundary effects, and metal–semiconductor interfaces, all contributing to the complex electronic response of $MAPbI_3$ thin films. Perovskite grains can form Schottky contacts with gold electrodes (highlighted in red), resulting in diode-like behavior during I–V measurements. Following poling, the remnant lateral ferroelectric polarization of individual grains induces the accumulation of screening charges at grain boundaries and establishes a net macroscopic polarization along the poling direction. Reproduced with permission from Röhm *et al.*, Adv. Funct. Mater. **30**, 1908657 (2020). Copyright 2020 Author(s), licensed under a Creative Commons Attribution (CC BY 4.0) license.[101]

discussion, an overview of the studied phenomena will be provided, examining how some of these effects, often seen as challenges in solar cells, could be leveraged for use in ferroionic devices such as memristors, transistors, and sensors. In these applications, hysteresis is often a desirable feature, enabling memory effects, switching behavior, and signal modulation.[90] This effect coupled with their optoelectronic properties makes them ideal for sensors and neuromorphic devices, which combine both photonic and electric inputs.[90]

The spontaneous polarization of perovskites was first proposed as an explanation for the hysteresis observed in the $MAPbI_3$ system, based on polarization-electric field (P-E) measurements[91,92] and PFM.[93,94] These techniques supported the interpretation of hysteresis using a ferroelectric diode model.[95] However, subsequent studies[91,96] revealed that the polarization loop was strongly frequency-dependent and diminished rapidly at room temperature, which is inconsistent with the presence of a bulk ferroelectric phase.

Two primary effects can contribute to electric polarization in hybrid perovskites (Fig. 7). The first, common to all perovskite structures, involves the displacement of lattice sites to non-centrosymmetric positions. For instance, the shift of the B cation from the center of the BX_6 octahedron creates a charge asymmetry, leading to spontaneous polarization, which alone can result in a weakly polarized lattice.[81] Theoretical simulations suggest that the size of the A-site cation, which is larger in organic molecules, can enhance this effect. Specifically, the calculated lattice polarization for $MAPbI_3$ is approximately 8 $\mu C\,cm^{-2}$, while for $FAPbI_3$, it is 63 $\mu C\,cm^{-2}$, due to the larger size of the formamidinium molecule.[81] Other studies have focused on the displacement of iodide atoms caused by the polar nature of MA^+, suggesting that a ferroelectric phase could be possible at room temperature.[42]

The second effect arises from the permanent dipole nature of the A-site cation. Methylammonium has a molecular dipole moment of 2.29 Debye,[81] which can be oriented by an internal or external electric field [Figs. 7(a) and 7(f)]. The former effect is significantly stronger and would account for most of the ferroelectric behavior if spontaneous dipole ordering occurs.[91] However, a high degree of dynamic disorder in the A-site cations and the absence of a polar space group structure at room temperature were observed by neutron diffraction and time-resolved SHG measurements.[97,98]

Despite these findings, several studies have demonstrated the possibility of inducing remnant polarization and switching in hybrid perovskites.[99,100] Rohm *et al.*[101] applied a small DC voltage across a $MAPbI_3$ perovskite for several minutes (a process known as "poling") and observed nanoscale ferroelectric domains and macroscopic remnant polarization [Figs. 8(a) and 8(f)], which modulated the nonlinear I–V curves. It was noted that the applied poling fields ($E = 2$ V μm^{-1}) were comparable in magnitude to those generated during normal operation under light absorption, suggesting that some level of self-induced poling might occur during standard operation and contribute to the observed I–V hysteresis [Figs. 8(g) and 8(k)].[101] The authors also emphasized the importance of aligning the poling field with the direction of perovskite grains [Fig. 8(l)],[101] a factor overlooked in earlier studies,[96] which often resulted in no remnant field or even the destruction of domains. Complementing this, Saraf *et al.*[102] used conductive atomic force microscopy (c-AFM) to demonstrate the presence of intrinsic spontaneous polarization, along which the photocurrent is notably enhanced. This enhancement increased further with

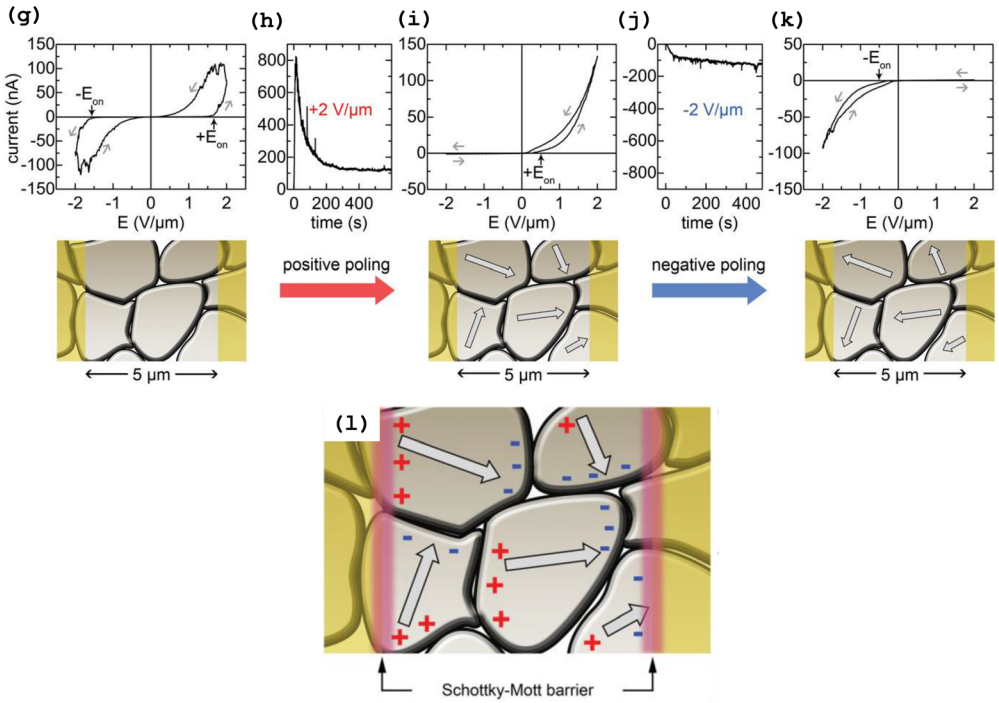

FIG. 8. (*Continued.*)

electrical poling and disappeared following a temperature-induced phase transition from the tetragonal to the cubic phase. These observations support the conclusion that ferroelectric behavior is responsible for the increased photocurrent (Figs. 6 and 7).

Studies on multi-cationic halide perovskites,[103,104] employing techniques such as contact Kelvin probe force microscopy (cKPFM), band excitation PFM, and dynamic-strain-based scanning probe microscopy, have provided strong evidence for photo-enhanced polarization and the presence of ferroelectric domains. These effects are often obscured by fast ionic migration, leading to many studies failing to detect such effects. Still, ferroelectricity has been associated with beneficial secondary effects such as more efficient charge transport along domain walls, through the so-called "ferroelectric highways" [Figs. 7(a) and 7(f)],[81] and improving open circuit voltage.[105]

The elusive nature of ferroelectricity in hybrid perovskites has led many researchers to explore alternative explanations for I–V hysteresis. Numerous studies have pointed to ionic migration and accumulation at the electrodes as primary contributors.[106–109]

Among the migrating species, halide ions are the most mobile due to their low activation energies, which range from $0.08 \leq E_a$ (eV) ≤ 0.68 depending on the perovskite composition and migration pathway.[110] Experimental studies on methylammonium lead iodide $MAPbI_3$ ($CH_3NH_3PbI_3$) report activation energies of $0.14 \leq E_a$ (eV) ≤ 0.30 for I- migration (Table II), while theoretical calculations suggest slightly higher values around 0.5 eV, with migration occurring primarily through vacancy-mediated mechanisms along the edges of PbI_6 octahedra. In mixed-halide systems, bromide (Br-) and chloride (Cl-) are less mobile, due to stronger lattice confinement and hydrogen bonding.[107] Organic cations, such as MA^+ and formamidinium cation FA^+ ($FAPbI_3$), also migrate but with higher activation energies compared to halides. MA^+ exhibits activation energies $0.36 \leq E_a$ (eV) ≤ 1.24 (Table II), while FA^+ is generally considered to be more

TABLE II. Summary of hybrid organic inorganic perovskites identifying the mobile species and activation energies of these perovskites obtained via DFT simulations or experimentally.

Characterization method	Material and condition	Mobile species	Activation energy [eV]	Ref.
DFT simulation	$MAPbI_3$	I^-	0.58	119
		Pb^{2+}	2.31	
		MA^+	0.84	
DFT simulation	$MAPbI_3$	I^-	0.08	109
		Pb^{2+}	0.80	
		MA^+	0.46	
	$MAPbBr_3$	Br^-	0.09	
		MA^+	0.56	
DFT simulation	$MAPbI_3$	I^-	0.32(0.44)	120
		MA^+	0.57(0.89)	
	$FAPbI_3$	I^-	0.48(0.55)	
		FA^+	0.59(0.61)	
DFT simulation	MAPbI3	I^-	0.34	107
		MA^+	0.74	
	$MAPbBr_xI_{3-x}$	Br^-	0.33	
		I^-	0.46–0.52	
		MA^+	0.80	
DFT simulation	$MAPbI_3$	H^+	0.29	121
Temperature dependent transient test (impedance)	$MAPbI_3$	MA^+	0.58	122
	$MA_xFA_{1-x}PbI_3$	MA^+/FA^+	0.63	
	$FAPbI_3$	FA^+	0.22	
Temperature dependent transient test (PL)	$MAPbBr_xI_{3-x}$	I^-/Br^- (attributed)	0.27	113
Temperature dependent transient test (PL)	$MAPbI_3$	I^-	0.14	123
Temperature dependent transient test (PL)	$MAPbI_3$	I^- (attributed)	0.19	124
Temperature dependent transient test (conductivity)	$MAPbI_3$	MA^+ (attributed)	0.36	125
Temperature dependent transient test (current)	$MAPbI_3$	Bulk	0.4	126
Temperature dependent transient test (current)	$MAPbI_3$	MA^+/I^- (attributed)	0.15–0.82 (light dependent)	127
	$MAPbI_3$	H^+ (attributed)	0.06–0.13	
Temperature dependent transient test (current)	$MAPbI_3$	Bulk	0.26	128
	$MAPbI_3$ film	Bulk	0.08 (light)	
	$MAPbI_3$ plate	Bulk	0.21 (light)	
Temperature dependent transient test (current)	$MAPbI_3$	Bulk	0.43	129

TABLE II. (*Continued.*)

Characterization method	Material and condition	Mobile species	Activation energy [eV]	Ref.
Temperature dependent transient test (current)	$MAPbCl_xI_{3-x}$	I^- (attributed)	0.23–0.31	130
Temperature dependent transient test (current)	$MAPbI_3$	Bulk	0.314 (1 sun)	131
		Bulk	0.341 (0.1–0.2 sun)	
	$MAPbBr_3$	Bulk	0.168 (1 sun)	
Temperature dependent transient test (current)	$MAPbI_3$ large grain	Bulk	0.5 (dark)	132
		Bulk	0.14 (light)	
	$MAPbI_3$ small grain	Bulk	0.27 (dark)	
		Bulk	0.08 (light)	
	$MAPbI_3$ single crystal	Bulk	1.05 (dark)	
		Bulk	0.47 (light)	
Temperature dependent transient test (voltage)	$MAPbI_3$	Bulk	0.68	119
Temperature dependent transient test (voltage)	$MAPbI_3$	Bulk	0.58	133

stable due to its larger size. Both are influenced by illumination, moisture and temperature.[111] In contrast, B-site cations like Pb^{2+} are effectively immobile under normal operating conditions, with activation energies as high as 2.31 eV, making their contribution to ion migration negligible unless the material undergoes severe degradation or under iodide rich synthesis conditions.[112] Mixed-halide perovskites, such as $MAPbBr_xI_{3-x}$, exhibit modified migration barriers due to lattice strain and altered defect chemistry. With the addition of Br-, the activation energy for I- migration increases from 0.34 to 0.46 eV.[113] Similarly, mixed-cation systems (e.g., $FA^+/MA^+/Cs^+$) show suppressed ion migration, as different-sized cations distort the lattice and raise energy barriers (Fig. 9).[111]

Extrinsic ions, introduced from external layers or environmental exposure, complicate the migration dynamics. Although difficult to directly measure, protons (H^+), originating from moisture or residual solvents, are highly mobile, with activation energies as low as 0.29 eV, contributing to device degradation through transient hydrogen bonding (Fig. 9).[114] Alkali metal ions, such as Li^+ from doped hole-transport layers, can migrate into the perovskite lattice, altering its electronic properties (Fig. 9).[115] Metal electrode ions, including Ag^+ and Au^+, diffuse under bias, forming halide salts (e.g., AgI) and accelerating interfacial degradation (Fig. 9).[116,117] In more extreme situations, the migration of iodide vacancies in AgI has been shown to form conductive filaments, which can be used for resistive switching devices.[118] Overall, the hierarchy of ion mobility in perovskites follows the trend I- > Br- > Cl- for anions and $MA^+ > FA^+ > Cs^+$ for cations, with extrinsic species like H^+ and Li^+ exhibiting high mobility under certain conditions (Fig. 9). Finally, it is worth noting that the potential barrier for ion migration in these perovskites is asymmetric, indicating the presence of dipoles, possibly resulting from the ferroelectric nature of these structures.[112]

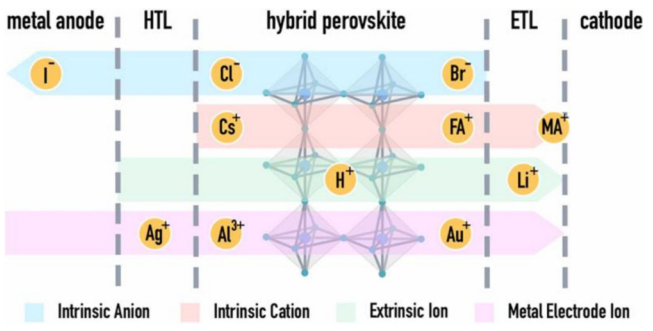

FIG. 9. Diffusion behavior and migration pathways of ions in perovskite solar cells. HTL: hole transport layer; ETL: electron transport layer. Reproduced with permission from Yan *et al.*, Nano Today **44**, 101503 (2022). Copyright 2022 Elsevier.[111]

The mixed ionic-electronic conductivity of perovskites enables directional ion migration under an applied electric field. Charged defects such as iodide vacancies (V_I^+) and interstitial halides (I_i^-) migrate toward oppositely charged electrodes, forming interfacial accumulation and space-charge regions.[111] This phenomenon has been directly observed via photothermal-induced resonance (PTIR) microscopy and TOF-SIMS, revealing segregation of MA^+ and halide ions near the respective electrodes.[111] Xiao *et al.* investigated ion accumulation in both lateral and vertical configurations, confirming that electrical poling induces significant ion migration.[134] Further evidence comes from Shao *et al.*, who combined AFM with macroscopic electrical measurements to demonstrate that poling redistributes ions along grain boundaries, contributing to strong hysteresis effects that could be exploited in photoelectric memory devices.[135] AFM-IR spectroscopy has provided high-resolution imaging of MA^+ electromigration, with increasing absorption intensity near the cathode under prolonged poling, confirming long-range MA^+ drift (Fig. 10).[136] Lan *et al.*[99] using KPFM revealed that perovskite polarization led to faster response times (reduced from 25 to 13 ms) and a tenfold increase in photocurrent in forward-poled $MAPbBr_3$ photodetectors.

Studies have demonstrated that illumination reduces the E_a for ion migration [Eq. (1)], for instance, E_a for I- migration drops from ~0.58 eV in the dark to ~0.22 eV under light. This photo-acceleration is attributed to excess charge carriers that weaken ionic bonds and facilitate defect-mediated hopping.[110] Similar electronic-ionic processes explain the photo-demixing of mixed-halide

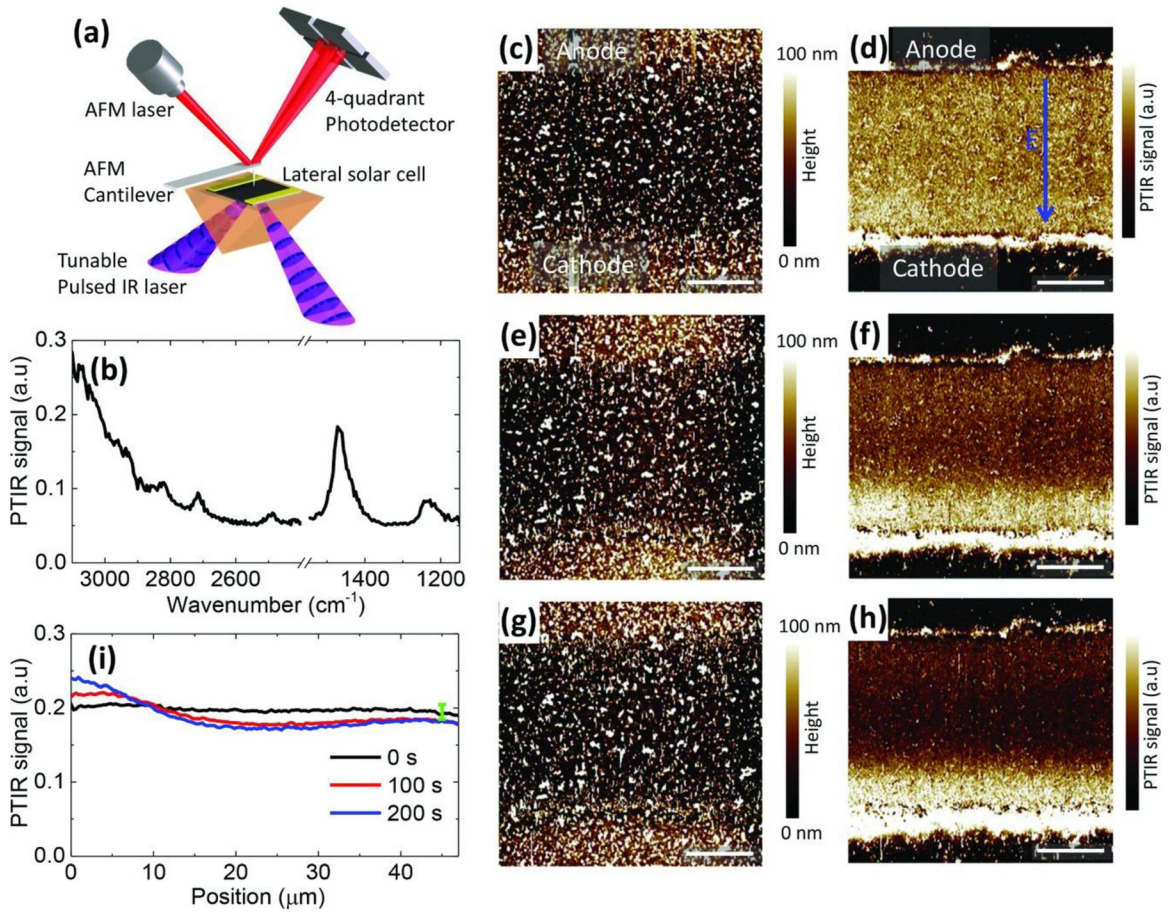

FIG. 10. (a) Schematic representation of the photothermal-induced resonance (PTIR) measurement setup. (b) Representative absorption spectrum recorded at the center of the device. (c), (e), and (g) AFM topography maps ($80 \times 80\ \mu m^2$) of the $MAPbI_3$ film over the same sample area: (c) before poling, (e) after 100 s, and (g) after 200 s of electrical poling. The applied poling field was $1.6\ V\ \mu m^{-1}$. (d), (f), and (h) Corresponding PTIR maps showing the absorption of the CH_3 asymmetric deformation mode of the methylammonium (MA^+) ion at $1468\ cm^{-1}$, captured (d) before, (f) after 100 s, and (h) after 200 s of poling. (i) Line-averaged PTIR intensity profiles (based on 256 vertical lines) from the perovskite region before and after poling, highlighting the redistribution of MA^+ ions. Error bars indicate uncertainties in the background level across different scans. All scale bars represent 20 μm. Reproduced with permission from Yuan *et al.*, Adv. Energy Mater. **5**, 1500615 (2015), Copyright 2015 Wiley.[136]

perovskites, where illumination reversibly forms iodide-rich and bromide-rich domains.[137]

Tsai *et al.* observed an expanded lattice structure with illumination in mixed cation perovskite films,[138] while Shao *et al.* revealed morphology-dependent effects, showing that noncompact perovskite films exhibit severe light soaking compared to compact counterparts.[139] The light soaking phenomenon was further explained by Zhao *et al.*[140] as resulting from defect reduction at interfaces through ion migration, thereby improving the heterojunction.[140] DeQuilettes *et al.*[124] reported photo-induced halide redistribution in the vertical direction using TOF-SIMS measurements.[124] It was observed that there was a decrease in iodide levels after light soaking and proposed a gradient trap-filling mechanism, where an induced electric field drives ion migration to fill vacancies.[124] Such light-induced ionic conductivity can be orders of magnitude higher than in the dark conditions, following consistent trends across different A-site cations.[141] Notably, these measured values represent apparent conductivity that may be influenced by concurrent electronic processes during polarization measurements (Fig. 11). These effects significantly impact device optoelectronics and degradation pathways while simultaneously enabling novel control of ionic behavior through optoelectronic stimuli.[142]

4. 2D OIHPs

Two-dimensional OIHPs are layered halide frameworks described by the general formulation $(A')_m (A)_{n-1} B_n X_{3n+1}$, where A' is a bulky spacer cation, A is a small A-site cation, B is a metal such as Pb and Sn, and X is a halide[144] (Fig. 12). They arise when bulky spacer cations insert between slabs of corner-sharing BX_6 octahedra, replacing the interfacial A sites. The result is a stack of quantum-well-like inorganic layers, separated by insulating spacer layers. In the Ruddlesden–Popper formulation, $n = 2$ and $\delta = 0$ (no X vacancies). For $n = 1$ the material is a pure 2D perovskite with a single octahedral layer between spacer sheets. For $1 < n < 4$ the structure contains multiple stacked

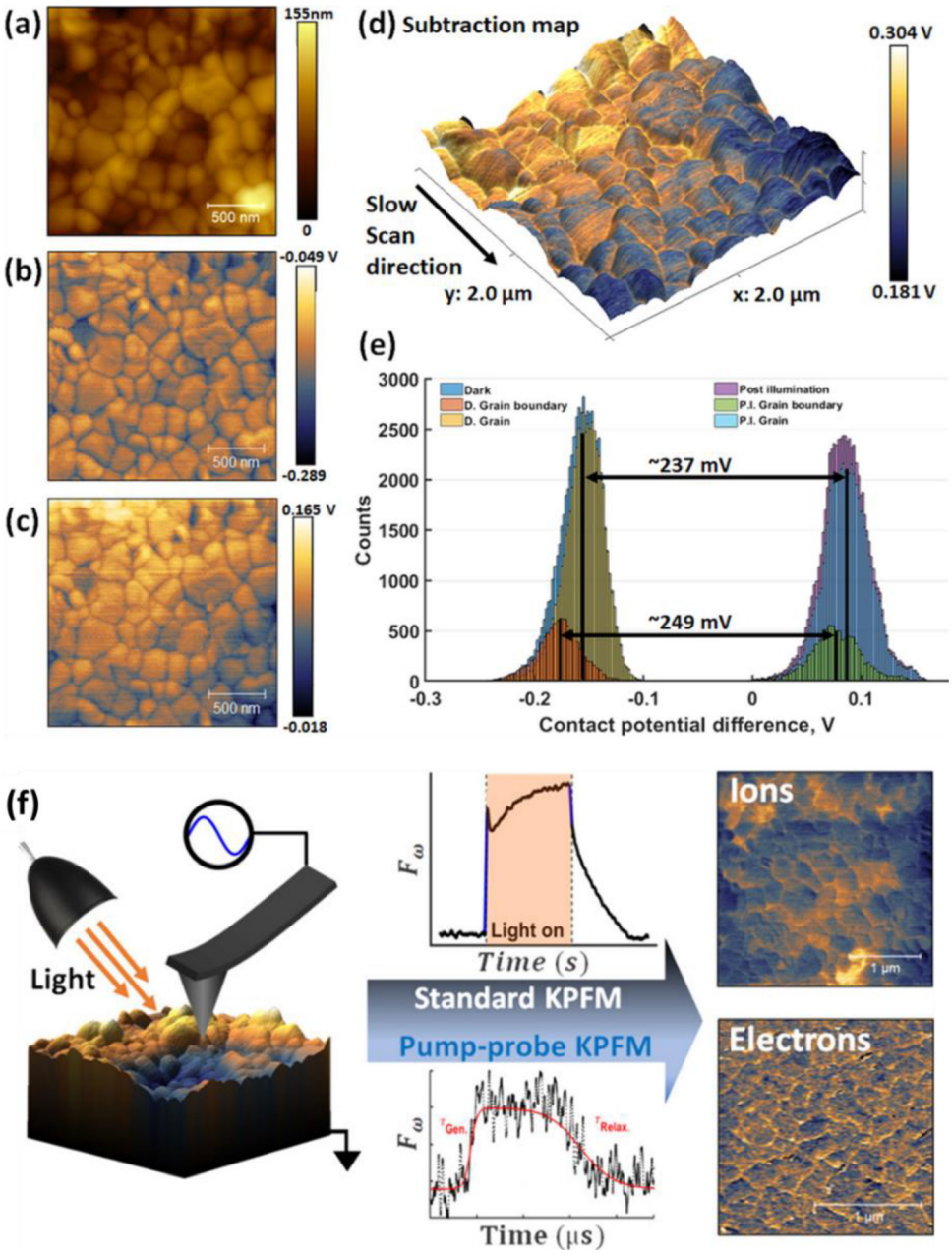

FIG. 11. Initial dark and relaxed closed-loop KPFM analysis of CsFAMAPbBrI. (a) Topography channel plotting surface height. (b) KPFM image prior to light pulse plotting V_{cpd}. (c) KPFM image seconds after the light pulse plotting V_{cpd}. (d) 3D topography overlaid with the calculated ΔV_{cpd} map. (e) Histograms of before and after V_{cpd} maps, separated into grain and GB responses. The double arrows indicate the difference between the mean values of the distributions. (f) Connection diagrams for Kelvin probe force microscopy (KPFM). Measurements: schematics of the setup for conventional and pump–probe KPFM measurements. In both configurations, an electrically driven AFM probe is employed to probe the electrostatic response of the perovskite material under illumination. Reproduced with permission from Toth *et al.*, ACS Appl. Mater. Interfaces **12**(42), 48057–48066 (2020). Copyright 2020 Author(s), licensed under a Creative Commons Attribution (CC BY 4.0) license.[143]

octahedral layers and is often termed quasi-2D or 2D/3D. Compared with fully 3D perovskites, these layered phases were introduced to boost device stability against moisture, heat, and ion migration.[144] Their reduced symmetry and inherent layering can also induce significant ferroelectricity, which, when coupled with their high photosensitivity, results in anomalous photovoltaic behavior and switchable functionalities.[145–147]

Ferroelectricity in 2D hybrid perovskites arises primarily from the dipolar character of the bulky spacer cation together with its substantial rotational freedom[148,149] (Fig. 12). This freedom creates pairs

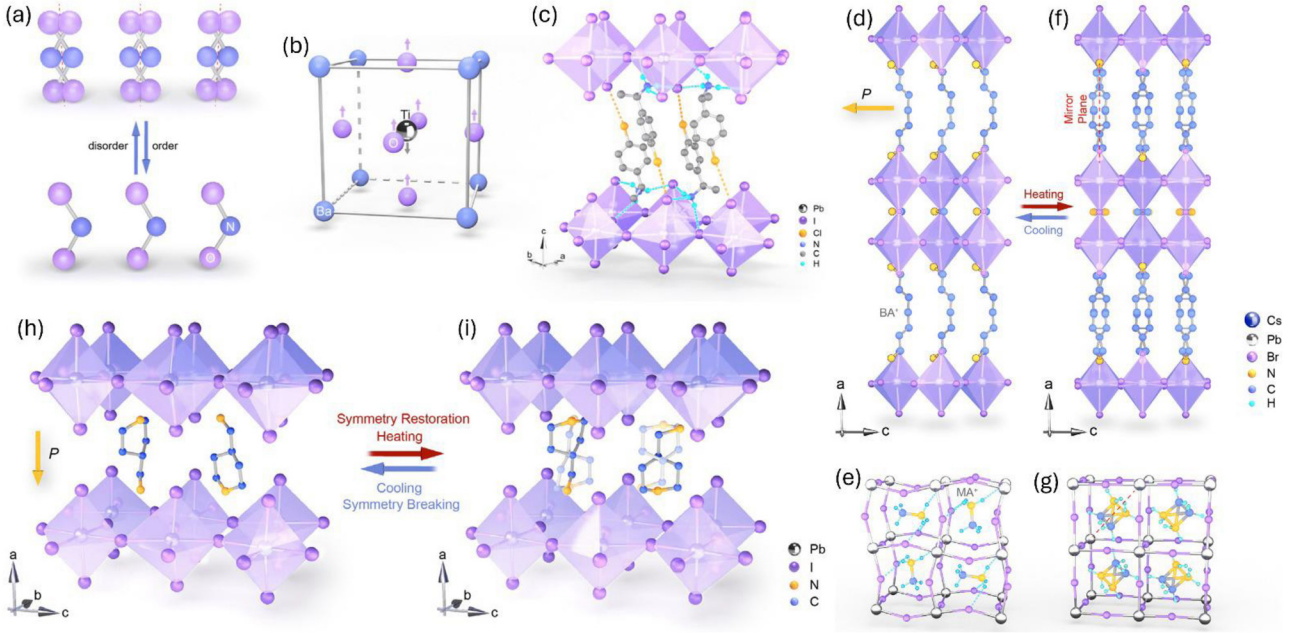

FIG. 12. (a)–(c) Types of ferroelectric mechanisms: (a) order–disorder; (b) displacive; and (c) mixed order–disorder and displacive. (d)–(g) Example of on-plane ferroelectricity: paraelectric–ferroelectric transition driven by the concerted motions of BA^+ organic cations and the inorganic anion cage in 2D hybrid perovskites (d) $(BA)_2(MA)Pb_2Br_7$ ferroelectric phase viewed along the b-axis. (e) Corresponding $PbBr_6$ framework with MA^+ at the ferroelectric phase. (f) $(BA)_2(MA)Pb_2Br_7$ at the paraelectric phase. (g) Corresponding $PbBr_6$ octahedra with MA^+ at the paraelectric phase. (h)–(i) Example of out-of-plane ferroelectricity: (h) Asymmetrical crystal structure of $(AMP)PbI_4$ crystal [AMP = 4-(aminomethyl)piperidinium] at the ferroelectric phase. The out-of-plane spontaneous polarization is along the a-axis; (i) Symmetry crystal structure of $(AMP)PbI_4$ at the paraelectric phase. The yellow arrows indicate the direction of spontaneous electric polarization. Reproduced with permission from Leng *et al.*, Trends Chem. **3**, 716 (2021). Copyright 2021 Elsevier.[150]

of energetically stable, off-center positions for the cations. Above the Curie temperature, the molecules rotate freely and, on average, occupy centrosymmetric sites with the mirror plane along the a-axis [Fig. 12(f)]. In this state, the dipolar fields cancel, so no net polarization appears. Below the Curie temperature, rotational motion is quenched, and the cations lock into one of the stable positions. Spontaneous in-plane polarization ($\vec{P}$ lies in the same plane as the layers) emerges when the dipolar molecules align uniformly along a single c-axis direction [Fig. 12(d)].[150] Out-of-plane polarization can occur when the A'-cation's rotational axis lies in the b–c plane and the molecular dipole moment points perpendicular to the layered framework [Figs. 12(h) and 12(i)].

The dependence of polarization on the A' spacer molecule enables tunability by altering the molecular composition. A common strategy to enhance polarization strength is fluorine substitution on the benzene ring of the widely used benzylammonium (BA) molecule. Zhang *et al.*[151] reported that the BA-based perfluorinated derivative $(PFBA)_2PbBr_4$ (PFBA = perfluorobenzylammonium) exhibits substantially stronger second-harmonic generation, larger spontaneous polarization, and a higher Curie temperature than any other fluorinated variant. Zhang *et al.*[152] further showed that replacing trimethylammonium (TMA) in $(EATMA)PbBr_4$ with the larger, heavier trimethylphosphanium (TMP) raises the rotational energy barrier sufficiently to enable a ferroelectric phase below 534 K. Park *et al.*[153] introduced a lead-free alternative with a spontaneous polarization of 10 $\mu C\,cm^{-2}$, exceeding typical values for lead-based counterparts.[154]

Recently, Hu *et al.*[155] have demonstrated ferroelectricity in both bulk quasi-2D hybrid perovskites and their derived monolayers, with devices showing switchable polarization alongside photoelectric functionality, a behavior uncommon in conventional ferroelectrics, which typically lose ferroelectricity at ultrathin or monolayer thickness. The latter properties point to a promising pathway for ultrathin, efficient photonic and ferroelectric devices.

C. $A_{3-2x}M_xOCl$, where A = Li^+, Na^+, or K^+, and M = Mg^{2+}, Ca^{2+}, Sr^{2+}, or Ba^{2+}

A novel family of materials has emerged in the field of battery technology, defined by the general formula $A_{3-2x}M_xOCl$, where A = Li^+, Na^+, or K^+, and M = Mg^{2+}, Ca^{2+}, Sr^{2+}, Ba^{2+}.[6,63,64,156–161] These electrolytes have attracted considerable interest due to their unique self-charging behavior, which is attributed to their intrinsic ferroelectric/ferroionic properties (Fig. 13).[6]

The first report on this class of materials was published in 2015 by Braga *et al.*,[162] who synthesized these glassy and semi-amorphous compounds via water-mediated wet synthesis.[162] The crystalline version of these electrolytes is the lithium-rich antiperovskite Li_3OCl,[162] with a "reversed" perovskite structure A = O^{2-}, B = Cl-, and X = Li^+. Doping with Ba^{2+} had the objective of creating vacancies (one for each Ba^{2+} ion), resulting in increased lithium ion conduction as the activation energy for creating vacancies is avoided.[162] The study reported an ionic conductivity approximately 25 mS cm^{-1} at room temperature for the $Li_{2.99}Ba_{0.005}OCl$,[162] a significant increase when compared to the

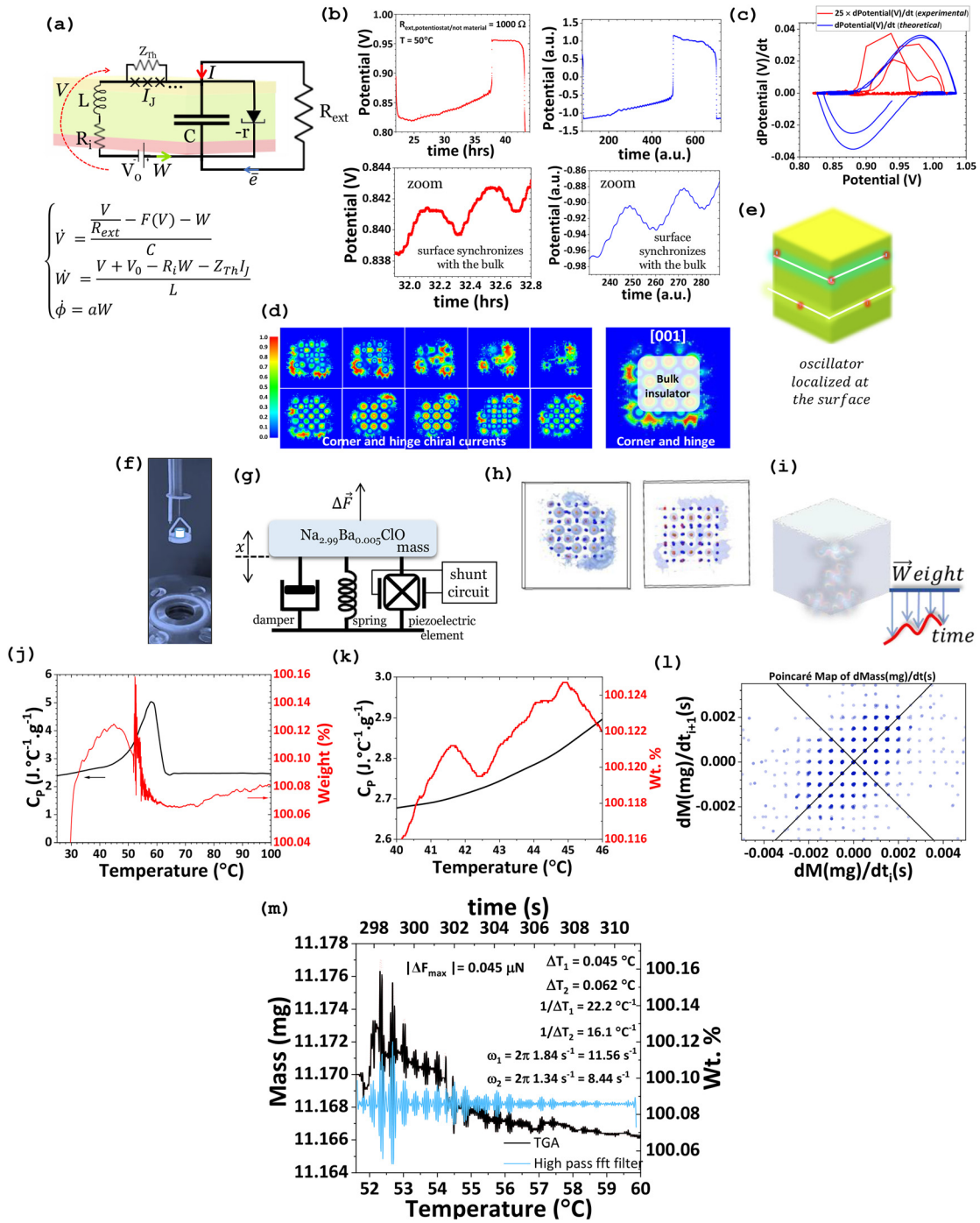

FIG. 13. (a) Equivalent circuit simulating the Zn/$Na_{2.99}Ba_{0.005}ClO$/Cu self-charging battery cell. (b) Zn/$Na_{2.99}Ba_{0.005}ClO$/Cu battery cell discharge with an external resistor of 1000 Ω showing self-charge (red) and matching simulations (blue). (c) Simulated phase portrait of (b). (d) Vortices in the electron localization function (ELF) are analyzed through DFT simulations of $(Na_3ClO)_{27}$ slices along the [001] cube surface. (e) 3D adaptation from (d) representing the FETI. (f) TGA platinum sample holder and crucible containing Na^+—ferroelectric electrolyte topologic insulator FETI. (g) Mechanical model of self-oscillating $Na_{2.99}Ba_{0.005}ClO$ via surface polarization. (h) $(Na_3ClO)_{27}$ 3D nanoparticle with surface localized edge electrons (in light blue), which generate electric fields and drive sample oscillations. (i) Schematics for the mechanical surface waves in the FETI; (j) Self-excited mechanical surface waves at the glass transition. (k) "Shapiro" steps on a Ferroionic electrolyte. (l) Poincaré map showing coherent piezoelectric states under Floquet dynamics. (m) Detailed view of the beat patterns from (j). Reproduced with permission from M. H. Braga, Chem. Commun. **60**, 5395–5398 (2024). Copyright 2024 Author(s), licensed under a Creative Commons Attribution (CC BY 4.0) license.[64]

highest reported value of conductivity for Li_3OCl to 1 mS cm^{-1} at room temperature.[163] Since the first synthesis,[162] based on simulations,[164] the ferroionic-electrolyte has been implemented in different all-solid-state devices.

Anode-less cells incorporating $Li_{2.99}Ba_{0.005}OCl$ as the solid-state electrolyte, LFP as the cathode, and no anode have been reported by Baptista *et al.*[161] During charging, Li metal was nucleated directly onto the current collector (CC) surface. These batteries were tested at different temperatures, with nucleation layers added to reduce the overpotential associated with Li nucleation on the Cu CC.[161] Recently, the same research group have demonstrated cells connected in series, advancing this technology toward real-world applications, where batteries typically consist of multiple cells associated in series.[159]

The ferroelectric nature of these electrolytes arises from the displacement of alkali metal ions (Li^+, Na^+, K^+) within the solid matrix.[6,63] This mechanism is analogous to the ferroelectricity observed in CIPS, which originates from Cu^+ ion displacement along the van der Waals layers.[7] Like CIPS, this family of electrolytes combines ionic conductivity with ferroelectricity at room temperature, traditional ferroionic behavior.[7] When incorporated in battery architectures, this family of electrolytes has showcased self-charging behavior.[63,64,156–158] The self-charging effect arises from an electronic feedback current that flows in the opposite direction to the discharging current through the surface.[63,64] When this feedback current exceeds the discharge current, the cell undergoes self-charging.[6] This phenomenon is made possible by the ferroionic behavior of the material and topologic metallic behavior, like in *polar metals*. Notably, the feedback current does not screen the bulk charge stored on the solid electrolyte, as noticed herein for TMDs, CIPS, and OIHPS (Fig. 1, Table I); otherwise, the battery cells with these electrolytes would short-circuit. Rather travels along its surface, suggesting the appearance of exotic surface states.[64] These surface phenomena are consistent with the characteristics of ferroelectric topological insulators (FETI).[165]

III. SENSING AND APPLICATIONS

Ferroionic materials provide a versatile platform for multifunctional devices, where the coexistence of ferroelectric polarization and ionic dynamics enables rich cross-coupled responses to diverse external stimuli. Beyond their promising role in optoelectronic sensing, these materials have demonstrated remarkable performance in electrically driven memristors, ferroelectric field-effect transistors, and tunnel junctions, as well as in mechanical, thermal, and magnetic sensing.[135,166–169] Such broad functionality arises from the strong coupling between electronic, ionic, and lattice degrees of freedom, which allows precise modulation of charge transport, optical transmission, and polarization states. Representative ferroionic systems, including perovskites (e.g., BTO, PZT, $Bi_{1-x}Sm_xFeO_3$, $MAPbI_3$, and $MAPbX_3$), chalcogenides (e.g., CIPS, α-In_2Se_3, MoS_2, WSe_2, and WS_2), and solid electrolytes (e.g., $A_{2.99}Ba_{0.005}OCl$, A = Li, Na, and K), have been engineered to exploit these coupled responses across optical, electrical, mechanical, thermal, and magnetic domains. This section reviews recent advances in these directions, highlighting how ferroionic materials enable adaptive, energy-efficient, and multifunctional sensing architectures for next-generation of integrated technologies.

A. Optical

The integration of ferroelectric and ferroionic materials into optical devices introduces novel functionalities that extend beyond traditional performance limits in detection, signal modulation, and data storage technologies.[170] The inherent coupling between electric polarization and mobile ionic species in ferroionic materials enables dynamic control of optical properties in response to external stimuli, making them attractive for next-generation optoelectronic systems.[169]

While conventional three-dimensional magnetic thin films have historically been used in tunable optical components, recent advances highlight the superior potential of 2D ferroionic materials.[171,172] These materials offer enhanced tunability, reduced footprints, and seamless compatibility with silicon-based photonic platforms.[169] This subsection explores key device functionalities enabled by ferroionic effects, organized into the following subcategories: photodetectors, electro-optic modulators, and nonlinear optical phenomena (Fig. 14).

1. Photodetectors

The interplay between ferroelectric polarization and ionic conduction in ferroionic materials enhances the tunability and sensitivity in photodetectors, as changes in polarization can dynamically modulate interfacial barriers and light–matter interactions. Such characteristics are particularly valuable for designing multifunctional photodetectors that integrate memory and sensing capabilities within a single device.[170]

a. CCPS (Table I). Dushaq *et al.*[169] demonstrated ionotronic modulation in a silicon photonic platform by incorporating multilayer $CuCrP_2S_6$ (CCPS), a ferroionic two-dimensional material, into microring resonators (Fig. 15). Although the primary focus was on electro-optic tuning, the ferroionic mechanisms underlying the optical modulation have direct implications for photodetector development; specifically, electric-field-driven ionic migration and polarization-dependent changes in refractive index. These processes can be harnessed to design bias-tunable photodetectors where light exposure dynamically alters local ionic configurations, leading to shifts in optical or electronic response. Such hybrid platforms hold

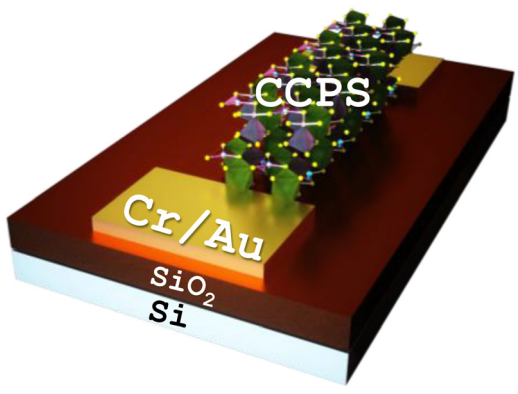

FIG. 14. Optical sensor Au/CCPS/Au (schematics designed for this study). Symmetric planar device cell.

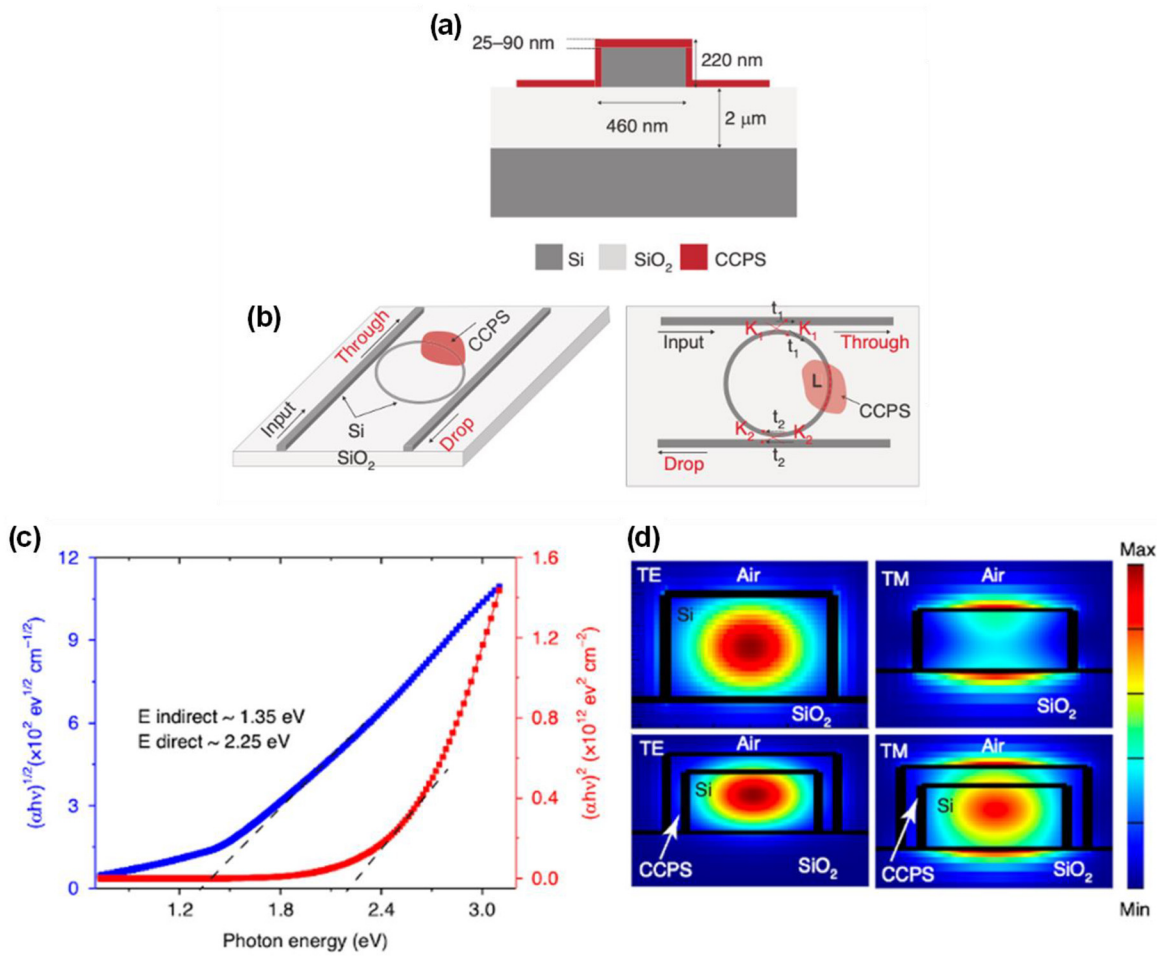

FIG. 15. Schematic of the photonic design and CCPS integration. (a) Cross-sectional view illustrating the key design parameters. (b) Three-dimensional and cross-sectional representations of the silicon microring resonator (Si-MRR) integrated with the carrier-concentration programmable structure (CCPS). Optical properties and light–CCPS interaction. (c) Tauc plots for direct and indirect transitions, derived from the absorption coefficient obtained via high-resolution spectroscopic ellipsometry. (d) Electric field intensity profiles ($|E|^2$) for TE and TM modes in a bare silicon waveguide (top panel) and in a silicon waveguide integrated with a 65 nm CCPS layer (bottom panel) at a wavelength of 1310 nm. Reproduced with permission from Dushaq *et al.*, Light Sci. Appl. **13**(92), 2047–7538 (2024). Copyright 2024 Author(s), licensed under a Creative Commons Attribution (CC BY 4.0) license.[169]

promise for multifunctional photonic components capable of both light detection and signal modulation.[169]

b. BTO (Table I). Tenreiro *et al.*[39] investigated a ferroionic memristive device composed of a $La_{0.7}Sr_{0.3}MnO_3/BaTiO_3/In_2O_3{:}SnO_2$ (90:10) heterostructure, where a 3 nm-thick $BaTiO_3$ ferroelectric barrier plays a central role. The device exhibits a nonvolatile resistive switching behavior driven by modulation of the Schottky barrier at the $La_{0.7}Sr_{0.3}MnO_3/BaTiO_3$ interface. Importantly, under ultraviolet illumination (3.3 eV), the device shows a photovoltaic response that varies with the resistive state. The open circuit voltage (OCV) scales linearly with the resistance, allowing for optical readout of the memristive state. This capability enables resistive state sensing at light intensities as low as 20 mW cm^{-2} and temperatures down to 100 K (−173 °C), showcasing the potential for optoelectronic memory-sensor integration.[39]

c. $MAPbI_3$ (Table I). Liu *et al.*[100] explored the tunability of photodetection in halide perovskite single crystals. Electrical poling induces ionic migration and interfacial polarization, which can significantly modulate the Schottky barrier height at the metal, semiconductor junction. This, in turn, enables dynamic control of the photocurrent and photodetectivity. The findings highlight the intrinsic ferroionic behavior of these materials and their potential for reconfigurable and self-powered photodetector applications. Such tunable responses open new pathways for developing adaptive optoelectronic systems with integrated memory and sensing functionalities.

2. Electro-optical modulators

Electro-optic modulators (EOMs) represent a natural and compelling application area for ferroionic materials. Unlike conventional

modulators that rely on carrier injection or thermo-optic effects, ferroionic systems exploit both ferroelectric polarization and mobile ionic species to achieve low-voltage, nonvolatile, and often polarization-sensitive modulation. These effects enable enhanced phase shifting, resonance tuning, and refractive index control, key functions in photonic circuits.

a. CCPS (Table I). Dushaq *et al.*[173] reported electric-field-induced refractive index tuning in hybrid silicon photonics using CCPS. Integrated into microring resonators, CCPS enabled reversible and efficient modulation while maintaining low optical losses. This platform achieved compact, energy-efficient modulation with potential for polarization-sensitive designs. In a detailed experimental study, Dushaq *et al.*[169] integrated CCPS into silicon microring resonators (Fig. 15), achieving electro-optic modulation through Cu^{+} ion displacement. The system showed a refractive index change of $\sim 2.8 \times 10^{-3}$ RIU with high modulation efficiency (0.25 V·cm) and polarization-sensitive behavior between transverse electric (TE) and transverse magnetic I modes.[169] These attributes surpass traditional transition metal dichalcogenide (TMD)-based modulators and point toward energy-efficient and compact solutions for integrated optics. Recently, Dushaq *et al.* have achieved non-reciprocal electro-optic modulation in CCPS-based resonators at short-wave infrared (SWIR) wavelengths. By leveraging ferroionic asymmetry, the device exhibited unidirectional light propagation without magnetic bias, a key milestone toward reconfigurable and nonvolatile photonic circuits. While challenges such as switching speed and ion drift remain, the latter work demonstrates the feasibility of using ferroionic materials for multifunctional and directional light control.

b. BTO (Table I). Cook *et al.*[174] demonstrated the synthesis of single-domain ferroelectric $BaTiO_3$ nanoparticles stabilized by internal strain and incorporated them into liquid crystal systems. Their strong internal dipole fields led to significant enhancements in electro-optic behavior, including reduced Fréedericksz transition voltages and improved optical gain in photorefractive two-beam coupling. These findings highlight how ferroionic nanoparticles can serve as effective functional dopants for modulating light propagation in composite media. Kelley *et al.*[175] investigated how the piezoelectric coefficient in $BaTiO_3$ thin films varies with thickness and strain. Their findings revealed a strong suppression of the converse piezoelectric coefficient, d_{33}, in ultrathin films, attributed to depolarization field screening. This insight is critical for electro-optic modulators relying on strain-mediated optical control, as it emphasizes the need for careful engineering of film thickness and interface conditions to maintain effective modulation performance.[175]

c. $MaPbX_3$ (Table I). Vasiljevic *et al.*[176] showed that organometallic perovskites ($MAPbX_3$) can display light-enhanced piezoelectric-like responses under electric field and UV illumination, driven by ionic redistribution. This coupling between light and ionic dynamics allows for direct optical control over polarization, opening the door for all-optical modulation strategies where light modulates piezoelectric response through ferroionic effects.[176]

d. $KTiOPO_4$. Among other interesting material systems is the work by Lindgren *et al.*,[177] which explores elasticity modulation in the ferroelectric superionic conductor $KTiOPO_4$ (KTP), where polarization reversal is coupled with K^{+} ion migration. This ionic movement led to softening of the lattice and surface charge redistribution, accentuating how ionic transport modulates electromechanical properties. These effects, in turn, influence optical parameters such as birefringence, suggesting the utility of KTP and similar materials for dynamic optical tuning.

e. $Bi_{1-x}Sm_xFeO_3$. Additionally, Morozovska *et al.*[178] explored reentrant polar phases in $Bi_{1-x}Sm_xFeO_3$ nanoparticles. Though focused on phase transitions, the study's emphasis on ferroionic coupling and external tunability reinforces the concept of field-controllable optical behavior, essential for adaptive EOMs.[178]

3. Nonlinear optics

Nonlinear optics (NLO) provides a powerful lens to investigate the dynamic responses and symmetry-breaking behaviors of ferroionic materials. These systems, distinguished by their coupled ionic and ferroelectric characteristics, offer rich opportunities for manipulating nonlinear susceptibilities [$\chi^{(2)}$ and $\chi^{(3)}$] through electric fields, strain, doping, or ion migration.[179] Compared to conventional ferroelectrics or electro-optic crystals, ferroionic materials uniquely combine spontaneous polarization with ionic mobility, enabling field-reconfigurable nonlinearities, optical bistability, and enhanced harmonic generation.

a. WS_2 (Table I). Chen *et al.*[180] investigated WS_2 matter coupling (nanofiber hybrids exhibiting strong light). While their study focused on tunable photoluminescence under linear regimes, the confined geometry and intensity-dependent optical response suggest potential for nonlinear processes such as third-harmonic generation (THG) and exciton-enhanced susceptibility. When integrated with ferroionic substrates such as CCPS for field-tunable ferroelectrics, such hybrid systems could realize electric-field-controlled nonlinearities, paving the way for ultrafast optical switches, frequency converters, or dynamically reconfigurable nonlinear metasurfaces.[180]

b. WSe_2 (Table I). Li *et al.*[181] demonstrated how complex excitonic species, including trions, biexcitons, and dark excitons in monolayer WSe_2, can be selectively manipulated via surface plasmon polaritons (SPPs). Through tailored exciton-photon coupling, they achieved control over nonlinear emission pathways, revealing a mechanism to enhance and tune nonlinear responses at the nanoscale. When applied to ferroionic environments, where local fields, strain, or charge distribution can be externally controlled, these findings suggest the feasibility of multi-modal nonlinear devices for frequency conversion, optical switching, and quantum photonic applications.[181]

c. CIPS (Table I). Hou *et al.*[182] demonstrate how interfacial strain and polarization coupling in 2D $CuInP_2S_6$ can be optically probed through photoluminescence spectroscopy, revealing strain-mediated bandgap modulation. Although not a direct nonlinear optical device study, their work provides key insight into how ferroionic strain polarization interactions can dynamically tailor the electronic and optical landscape of layered materials, laying important groundwork for tunable nonlinear optical responses in future adaptive photonic systems.[182]

d. CCPS (Table I). Wang *et al.*[183] explored CCPS and revealed coupled ferroelectric and antiferromagnetic order with strong anisotropy. These characteristics imply the presence of robust second-order nonlinearities, making $CuCrP_2S_6$ a promising platform for SHG and magneto-optical switching. The authors highlighted that the dynamic interplay between ionic transport and polarization in such materials allows for real-time modulation of nonlinear optical coefficients, enabling adaptive photonic functionalities such as electro-optic Kerr effects and field-tunable harmonic generation in nanoscale devices. Aoki *et al.*[184] provided direct evidence of tunable second-harmonic generation in CCPS through magnetoelectric coupling. The SHG response was strongly dependent on temperature and magnetic field, confirming that the nonlinear optical behavior of the material is sensitive to external stimuli. Furthermore, the study revealed layer-dependent modulation of SHG efficiency, linking the number of atomic layers to symmetry and magnetoelectric interactions. These results highlight the potential of 2D multiferroic ferroionic materials for precise, field-tunable nonlinear optics in integrated systems.[184]

Overall, these findings feature the transformative potential of ferroionic materials across multiple domains of photonic technology. In photodetectors, they enable a new generation of light-responsive devices with integrated memory, sensing, and modulation capabilities, paving the way for multifunctional and reconfigurable optoelectronic systems. In electro-optic modulators, the coupling between ionic motion and polarization switching imparts a unique combination of tunability, sensitivity, and energy efficiency, offering a promising route toward compact and adaptive modulators, particularly as integration with silicon photonics advances.[106,169,184]

In the realm of nonlinear optics, ferroionic materials emerge as highly versatile platforms capable of supporting electric-, magnetic-, and strain-tunable nonlinearities. This intrinsic adaptability opens new frontiers for ultrafast modulation, harmonic generation, and programmable nonlinear metasurfaces. Complementing these functionalities, ferroionic materials also show great promise for tunable optical filters, where their ability to induce localized refractive index changes and nonvolatile tuning supports the development of reconfigurable, high-performance filter architectures for modern photonic systems.[106,169,184] Other emergent ferroionics also show promising optical response in small demonstrators (Fig. 16).

B. Electrical

Ferroionic materials, due to their unique combination of ferroelectricity and ionic conductivity, are highly responsive to external electrical stimuli. Their ferroelectric nature enables the reversible switching of spontaneous polarization under an applied electric field, allowing for precise detection of electric field variations.[87]

1. Memristors

Memristors have emerged as essential components in neuromorphic computing, owing to their ability to emulate synaptic plasticity through conductance tuning (Fig. 17).[186] Their strong appeal lies in key performance advantages, including high switching ratios,

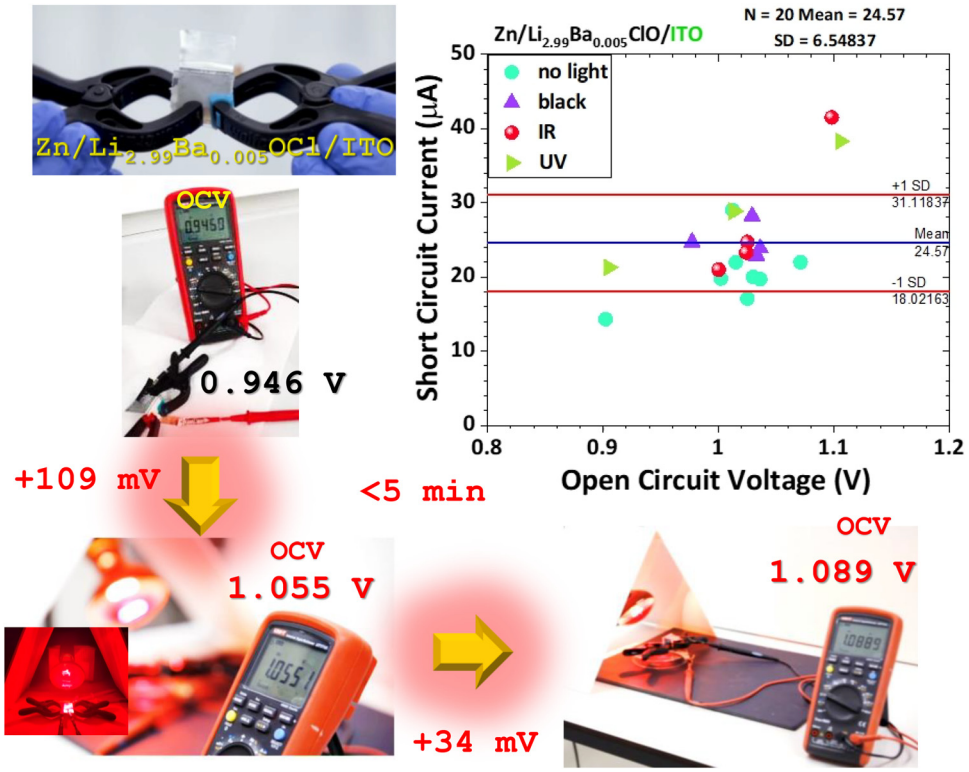

FIG. 16. Optical response of a $Zn/Li_{2.99}Ba_{0.005}OCl/ITO$ demonstrator photovoltaic cell ($2 \times 2\,cm^2$). Short circuit current for different electromagnetic radiation wavelengths. Schematics obtained for this study.

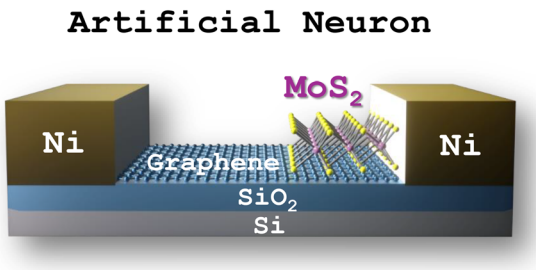

FIG. 17. Neural networks (schematics designed for this study). Vertical (v)-MoS_2/graphene threshold switching memristor artificial neuron. Reproduced with permission from Kalita *et al.*, Sci. Rep. **9**(53), 53 (2019). Copyright 2019 Author(s), licensed under a Creative Commons Attribution (CC BY 4.0) license.[185]

exceptional storage density, low energy consumption, and robust operational stability.[187] The emergence of 2D ferroelectric materials has created new opportunities for advancing high-performance memristor technologies. Their ability to form vdW heterostructures (Fig. 17) enables precise tuning of electronic and ferroelectric properties, which is crucial for optimizing device performance. Several studies have identified mixed ionic-electronic conduction in OIHP-based solar cells (Fig. 1, Table I),[124,188–190] indicating that ion migration plays a significant role in their operation. This property highlights the potential of OIHP materials for memristor applications.[191] Memristive behavior typically arises from two main mechanisms: ionic migration and charge trapping/detrapping, both influenced by the choice of electrode materials and the composition of the OIHP layer.[191]

a. MoS_2 (Table I). Kalita *et al.*[185] developed a two-terminal Ni/v-MoS_2/graphene memristor, utilizing vertically grown MoS_2 (v-MoS_2) as the switching layer and graphene as the bottom electrode in a vdW heterojunction structure (Fig. 18). The device exhibited volatile threshold-switching behavior, with fast and repeatable transitions between high and low resistance states, enabling key neuronal characteristics such as all-or-nothing spiking, threshold-driven firing, refractory period, and input-strength-modulated frequency response.[185] Unlike traditional complementary metal–oxide–semiconductor (CMOS), in neuron circuits, the switching mechanism is driven by oxygen ion migration along vertical grain boundaries in polycrystalline MoS_2, allowing for low-power operation and scalability in neuromorphic computing applications (Fig. 18).[185]

Abnavi *et al.*[192] reported strong resistive switching behavior in a free-standing 2H-phase single-crystalline multilayer MoS_2 device with an Au/suspended MoS_2/Au structure. The switching was attributed to adsorbed O_2 and H_2O molecules on both sides of the MoS_2 channel. The device showed an on/off ratio of $\sim 10^3$ between the low- and high-resistance states, which increased up to $\sim 10^5$ under a modulated continuous-wave laser beam, with higher laser power enhancing the effect.[192] Additionally, the memristor successfully emulated synaptic plasticity functions, including short-term memory (STM), long-term memory (LTM), and the STM-to-LTM transition, controlled by adjusting light intensity, pulse duration, and pulse count.[192]

b. WS_2 (Table I). Yan *et al.*[193] developed a two-terminal memristor based on 2H-phase 2D WS_2 with a Pd/WS_2/Pt structure, exhibiting ultrafast switching (13 ns SET, 14 ns RESET), low ON-state current (1 μA), and femtojoule-level energy consumption—making it suitable for low-power neuromorphic computing.[193] Its resistive switching is attributed to the formation of sulfur and tungsten vacancies, along with electron hopping between these defect sites. The device also mimics essential synaptic behaviors, including paired-pulse facilitation (PPF), spike-time-dependent plasticity (STDP), and short-term plasticity (STP) to long-term plasticity (LTP) transitions.[193]

c. α-In_2Se_3 (Fig. 1). Zhang *et al.*[194] developed a two-terminal Au/α-In_2Se_3/Ti memristor that exhibits dual-mode operation based on applied voltage. At low voltages, it exhibits analog resistive switching based on Schottky barrier modulation by ferroelectric polarization, enabling key synaptic functions such as excitatory postsynaptic current (EPSC), inhibitory postsynaptic current (IPSC), LTP, long-term depression (LTD), and STDP. A neural network simulation using this device achieved 93.2% recognition accuracy on the Modified National Institute of Standards and Technology (MNIST) dataset *[198].* At higher voltages, the device transitions to a digital switching mode driven by filament formation, exhibiting nonvolatile resistive switching with an on/off ratio $>10^3$, current density up to 10^5 A cm^{-2}, fast switching speed ($\sim$10 ns), and robust retention over 10^4 s.[194] Zhao *et al.*[186] fabricated an α–In_2Se_3–based memristor device by spin-coating α-In_2Se_3 onto an indium tin oxide (ITO) substrate and depositing an Ag electrode on top, resulting in an Ag/α-In_2Se_3/ITO structure. This device exhibited typical bipolar resistive switching behavior, demonstrating excellent endurance, high switching speeds (16.4 ns for the SET process and 18.0 ns for the RESET process), and continuous tunability under AC pulse stimulation.[186] Moreover, the device could implement four distinct STDP learning rules. Additionally, reinforcement learning behavior was successfully simulated, providing a foundation for future applications in brain-inspired computing and artificial intelligence.[186] Li *et al.*[195] highlighted the potential of α-In_2Se_3 for vertical memristor applications by successfully fabricating a few-layer graphene/α-In_2Se_3/few-layer graphene heterojunction. Through electrical measurements of the device, they observed hysteresis behavior, which they attributed to the formation of a Schottky-like barrier at the metal-semiconductor interface induced by polarization modulation[195]

d. CIPS (Table I). Chen *et al.*[196] developed a planar CIPS memristor device with Cr/Au electrodes, leveraging the high conductivity from Cu^+ ion migration. By precisely controlling the movement of these ions under an electric field, they were able to regulate the device's electrical conductivity and replicate various synaptic plasticity behaviors, such as STP, LTP, and STDP. The controlled movement of Cu^+ ions allows for gradual changes in conductance, replicating how synaptic weights adjust in biological neurons.[196] This mechanism enhances memory retention while enabling low-voltage operation (as low as 0.5 V) to minimize power consumption. This device demonstrated strong potential for energy-efficient neuromorphic computing, offering a retention time of up to 3500 s and durability exceeding 100 cycles.[196] Zhong *et al.*[34] developed a two-terminal Cu/CIPS/graphene memristor. This device demonstrated robust threshold-switching behavior, achieving a high on/off ratio of up to 10^4, low operating voltages, an ultra small subthreshold swing (<1.8 mV/decade), and exceptional cycling endurance.[34] Unlike conventional memristors that rely on

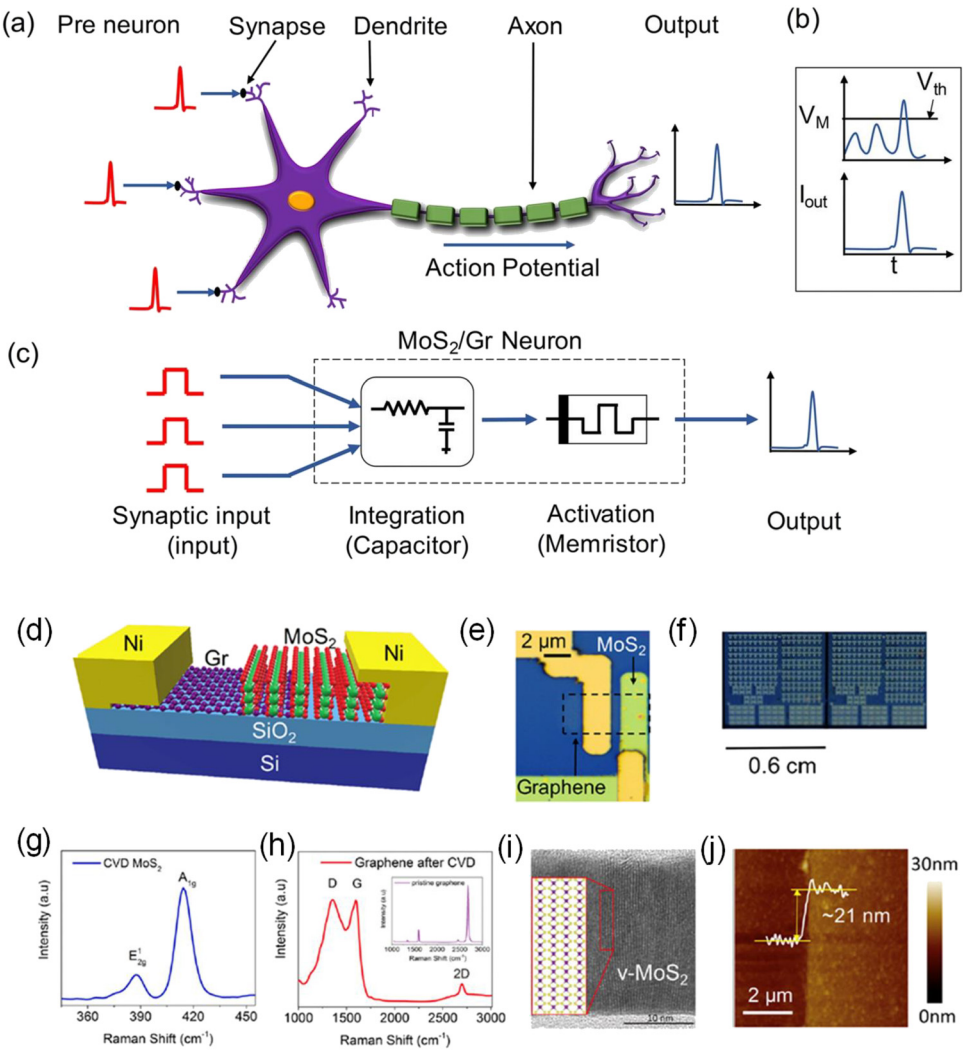

FIG. 18. (a) Schematic representation of a biological neuron, illustrating signal transmission from the pre-neuron to the output. (b) Neuronal output spiking behavior as a function of the input threshold. (c) Conceptual diagram of an artificial neuron based on a v-MoS_2/graphene memristor structure. (d) Diagram of v-MoS_2/graphene threshold switching memristor artificial neuron. (e) optical photograph of the device in (d). (f) 200 devices of (d) in a prototype chip. (g)–(h) Raman spectra of as grown MoS_2 on graphene and of graphene after chemical vapor deposition (CVD). (i) High resolution transmission electron microscopy (HR-TEM) of v-MoS_2/graphene interface. (j) AFM topography of MoS_2 to determine the thickness. Reproduced with permission from Kalita *et al.*, Sci. Rep. **9**(53), 53 (2019). Copyright 2019 Author(s), licensed under a Creative Commons Attribution (CC BY 4.0) license.[185]

conductive filament formation, its stable switching mechanism was driven by controlled Cu^+ ion migration within the ferroionic CIPS layer, enhancing reliability and performance.[34] Liu *et al.*[197] developed an Ag/CIPS/Au memristor device using Ag as the top electrode and Au as the bottom electrode. At a compliance current (maximum current limit set during electrical testing to prevent device damage) of 10 μA, the device exhibits volatile resistive switching, achieving a high rectification ratio of 10^3, sustained for up to 500 cycles.[197] However, when operated at a compliance current below 5 μA, it exhibits nonvolatile resistive switching, with an on/off ratio of 10^3 and an impressive retention time of up to 10^4 s.[197] Furthermore, the device successfully emulates synaptic plasticity, namely, STP and LTP.[197]

e. BTO (Table I). Pérez-Martínez *et al.*[198] developed a planar perovskite-based memristor with an FTO/$MAPbI_3$/PMMA/Ag structure, achieving strong performance metrics: retention time $>10^5$ s, an on/off ratio of 10^6, and endurance over 2000 cycles.[198] The device forms stable conductive filaments from iodide vacancies and metallic Pb after initial cycles, enabling reliable switching with low SET and RESET voltages. Its behavior is governed by Ohmic conduction in the low-resistance state and thermionic emission in the high-resistance state. While Ag filaments can also form under high voltage, they cause device failure due to irreversible electroforming.[198]

f. $MAPbI_3$ (Table I). Patil *et al.*[199] advanced a Pd/$MAPbI_3$/ITO diffusive memristor to mimic the operation mechanism of nociceptors

associated with biological pain perception (Fig. 19). This device presented a high on/off ratio of 10^4, a bending endurance of over $>10^2$, excellent uniformity, and forming-free behavior for a volatile diffusive memristor.[199] The device successfully emulated the key features of an artificial nociceptor, such as "threshold," "no adaptation," and "relaxation" by modulating the pulse signal, which is crucial for pain perception.[199]

2. Tunnel junctions

Ferroelectric tunnel junctions (FTJ) employ an ultrathin ferroelectric layer as the tunneling barrier, whose potential profile can be modulated by reversing the ferroelectric polarization.[200] These structures are considered promising candidates for memory and computing applications owing to their low power requirements, nonvolatile switching behavior, and nondestructive readout capability. However, achieving a high tunneling electroresistance (TER) remains a challenge in these devices.[201] Two-dimensional vdW ferroelectric materials offer significant potential for achieving large TER due to their minimal defects, the absence of interfacial states in vdW heterostructures, and the easy tunability of their chemical potentials.[202] The ABO_3-type perovskite oxides, such as $BaTiO_3$, $PbTiO_3$, and $PbZr_xTi_{1-x}O_3$ (PZT), are among the most widely used materials in FTJs. To function effectively, they must be fabricated as nanometer-thin films; however, ferroelectricity tends to degrade below a critical thickness. To overcome this, researchers have focused on enhancing polarization to improve the TER ratio, making precise control of film thickness a key priority in FTJ development.[201]

a. α-In_2Se_3 (Fig. 1). Luo *et al.*[203] developed a robust vdW FTJ based on a 2D semiconductor (2DS)/α-In_2Se_3/metal structure, which demonstrated endurance over 4000 switching cycles. They investigated various 2DS materials, including MoS_2, $PdSe_2$, $SnSe_2$, and graphene. Notably, the MoS_2-based device exhibited a room-temperature negative differential resistance (NDR) effect with a peak-to-valley ratio exceeding 100, alongside a TER exceeding 10^4, both of which are highly gate-tunable.[203] The study also reveals that the dominant current transport mechanism depends on the choice of 2D electrode: MoS_2 and $PdSe_2$ favor tunneling-dominated transport, while $SnSe_2$ and graphene are governed by thermionic emission. To address leakage issues, the authors, supported by temperature-dependent measurements, propose using less conductive 2D materials to suppress thermionic current.[203]

b. CIPS (Table I). Wu *et al.*[200] reported a FTJ based on a graphene/CIPS/Cr vdW heterostructure, achieving a TER exceeding 10^7 (Fig. 20). This performance is primarily attributed to pronounced modulation of the tunneling barrier height, enabled by ferroelectric polarization reversal in CIPS, which induces a Fermi-level shift of ∼1 eV in the graphene electrode.[200] This effect is further amplified by the large out-of-plane effective mass in CIPS and the presence of a ∼4 nm barrier, which supports low-power operation.[200]

Wang *et al.*[202] developed a FTJ based on a vdW heterostructure composed of the 2D ferroelectric CIPS and various 2D electronic materials, including graphene, MoS_2, and WSe_2. Their device demonstrated a record-high TER exceeding 10^{10} at room temperature, which is attributed to the substantial ferroelectric modulation of both the tunneling barrier height and the electronic band alignment of the 2D materials.[202] Notably, an additional order-of-magnitude increase in TER was achieved in Cr/CIPS/graphene junctions by simply inserting a monolayer of MoS_2 or WSe_2 between CIPS and graphene.[202]

c. BTO (Table I). Wang *et al.*[38] explored the thickness-dependent TER and the associated evolution of charge transport mechanisms in Pt/$BaTiO_3$/$LaNiO_3$ FTJs with $BaTiO_3$ layers of 2.0, 3.2, and 4.8 nm. A clear TER effect was observed in the 3.2 nm-thick device, yielding an on/off current ratio of approximately 170, attributed to polarization-driven modulation of the barrier height.[38] Increasing the thickness to 4.8 nm enhanced the ferroelectric modulation of the barrier, resulting in a transition of the dominant transport mechanism from quantum tunneling to thermally activated thermionic injection. This shift led to

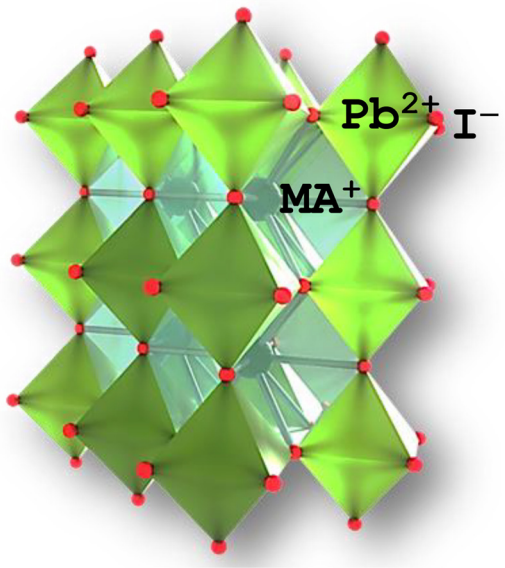

FIG. 19. Perovskite structure of $MAPbI_3$.In the perovskite structure ABX_3: $A = MA^+$, $B = Pb^{2+}$, and $X = I^-$. Schematics designed for this study.

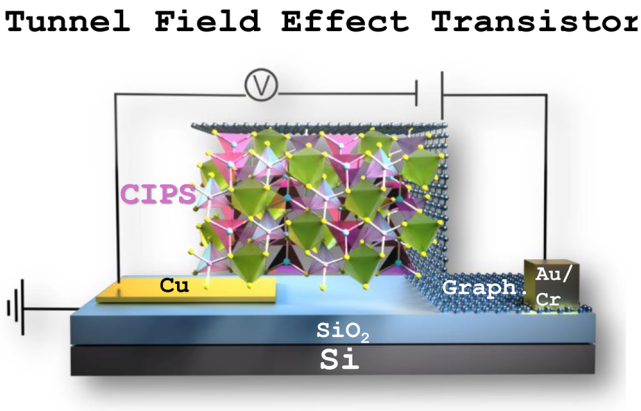

FIG. 20. Ferroelectric CIPS-based tunnel field effect transistor. Graphene/CIPS/Cr vdW heterostructure. Schematics designed for this study.

a substantial reduction in the off-state current, primarily due to the suppression of Fowler–Nordheim tunneling as the barrier became both wider and higher. Consequently, the 4.8 nm-thick FTJ demonstrated a markedly improved on/off current ratio of approximately 12500.[38]

3. Ferroelectric field-effect transistors

Transistors are fundamental to modern electronics, powering devices from computers to smartphones. Recently, ferroelectric field-effect transistors (FeFETs) have gained attention for their potential in nonvolatile memory and neuromorphic computing.[204] However, traditional ferroelectric oxide-based FeFETs face several commercialization challenges, including poor memory retention due to charge trapping and interfacial oxide formation, as well as reduced efficiency from indirect channel modulation via gate polarization.[205]

The emergence of vdW layered ferroelectrics has addressed key limitations of conventional oxide-based ferroelectric FeFETs. These materials maintain robust ferroelectricity down to atomic thickness and possess dangling bond-free surfaces, reducing charge trapping and interfacial issues, allowing for high-quality, lattice-mismatch-free vdW heterostructures.[205]

a. MoS_2-PZT. Lipatov *et al.*[206] presented MoS_2-PZT–based FeFETs as a powerful alternative to graphene-based and traditional ferroelectric random-access memory (FeRAM) devices. These devices employ monolayer or few-layer MoS_2 as the channel material and PZT as the ferroelectric gate dielectric. Due to MoS_2's sizable electronic bandgap, in contrast to graphene's zero bandgap, the FeFETs exhibit large hysteresis in electronic transport and high on/off current ratios, making them well-suited for nonvolatile memory applications. The study also reveals a reversed polarization-dependent hysteresis influenced by interfacial charge effects and shows that these memories support nondestructive readout, low-voltage operation, and dual electrical-optical switching, offering advantages for future nonvolatile memory technologies.[206]

b. α-In_2Se_3 (Table I). Baek *et al.*[205] reported a FeFET based on vdW materials, incorporating CIPS as the ferroelectric gate dielectric, α-In_2Se_3 as the ferroelectric semiconducting channel, and hexagonal boron nitride (hBN) as the insulating layer (Fig. 21). The device exhibited a wide memory window of 14.47 V, an on/off current ratio exceeding 10^6, robust data retention (>10^4 s), and excellent endurance (>10^4 cycles). These results are attributed to dipole coupling at the α-In_2Se_3/CIPS interface.[205] To further explain the observed hysteresis enhancement, the authors extended the Landau–Khalatnikov model to account for interactions between two ferroelectric layers.[6,205] Moreover, the device demonstrated neuromorphic functionality by emulating key synaptic behaviors.[205]

c. CIPS (Table I). Baek *et al.*[205] reported an all-ferroelectric FeFET device comprising CIPS, hBN, and α-In_2Se_3 flakes, serving as

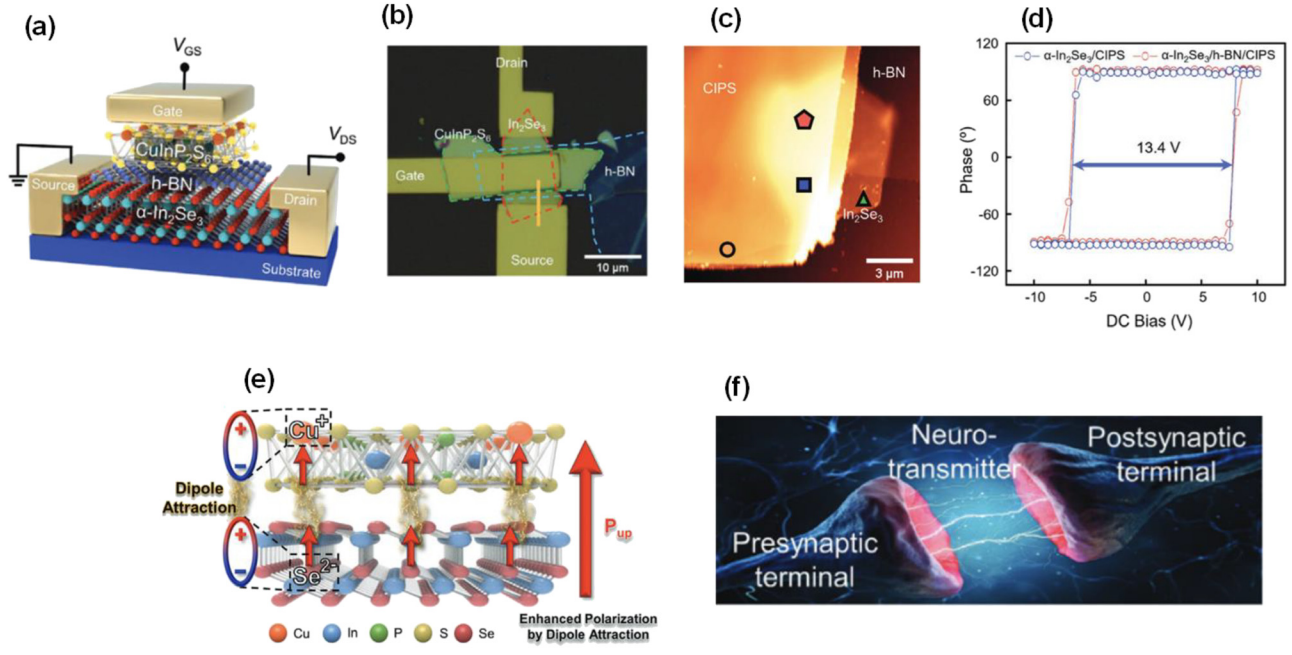

FIG. 21. Ferroelectric field effect transistors with integrated ferroelectric and ferroionic heterostructures. (a) Diagram of a three-terminal vdW heterostructure ferroelectric Fe-FET incorporating CIPS, hBN, and α-In_2Se_3. (b) Optical microscopy image of the vdW heterostructure Fe-FET constructed from an α-In_2Se_3/hBN/$CuInP_2S_6$ layered stack. (c) AFM topography of the Au/α-In_2Se_3/hBN/CIPS/AFM-tip stack, along with the locations where PFM hysteresis loops were measured. (d) Map showing the coercive width (lower right), derived from averaging nine hysteresis measurements per point. (e) Illustration of the atomic arrangement representing the upward polarization state in the α-In_2Se_3/CIPS heterostructure. (f) Comparison between the structure of a biological synapse and the architecture of a three-terminal vdWH Fe-FET functioning as an artificial synapse. Reproduced with permission from Baek *et al.*, Adv. Sci. **9**, 2200566 (2022). Copyright 2022 Author(s), licensed under a Creative Commons Attribution (CC BY 4.0) license.[205]

the ferroelectric gate dielectric, insulating layer, and ferroelectric semiconducting channel, respectively (Fig. 21). The device exhibited outstanding performance, including a high on/off current ratio exceeding 10^6, robust data retention exceeding 10^4 s, and reliable endurance over 10^4 switching cycles at room temperature.[205] These enhanced characteristics are primarily attributed to dipole coupling at the α-In_2Se_3/CIPS interface. Furthermore, the heterostructure device effectively emulated key biological synaptic behaviors, including excitatory/inhibitory post-synaptic currents (EPSC/IPSC), PPF, and LTP/LTD.[205]

Si *et al.*[207] demonstrated the fabrication of FeFETs based on a 2D vdW heterostructure comprising MoS_2 as the channel and CIPS as the ferroelectric gate insulator. The devices exhibit clear room-temperature ferroelectric behavior with counterclockwise hysteresis in their transfer characteristics, confirming nonvolatile memory functionality. The dual-gate structure enables modulation of the memory window and on/off current ratio via back-gate bias, enhancing performance. Additionally, the CIPS layer shows resistive switching with an on/off ratio exceeding four orders of magnitude, suggesting potential for resistive memory applications.[207]

d. PZT (Table I). Jo *et al.*[41] developed FeFETs using epitaxially grown single-crystal PZT films as gate insulators and amorphous indium gallium zinc oxide (a-IGZO) as channel materials to emulate biological synapses. The devices exhibited clockwise hysteresis in their transfer curves, attributed to charge trapping and ferroelectric polarization effects. Synaptic plasticity was demonstrated under voltage pulse stimulation, with nonlinearity values of 0.00 and 5.41 for 16 pulses (potentiation), and 0.51 and 7.05 for 32 pulses (depression).[41]

e. $A_{2.99}Ba_{0.005}OCl$ *(A = Li, Na, K) (Table I).* $Na_{2.99}Ba_{0.005}OCl$ has been explored in various electrode-less battery-cell configurations, which are like the device-cell in Figs. 6(c) and 6(f) or the SG circuit in the cell of Figs. 19(a). In pouch-cell format, Freitas *et al.*[156] reported a Cu/$Na_{2.99}Ba_{0.005}OCl$/Zn cell that, despite lacking traditional electrodes, exhibited an OCV of 1.2 V and was capable of undergoing charge-discharge cycles. A self-charging effect was observed during discharge. This self-charging behavior had been previously reported by Danzi *et al.*,[157] who assembled structural cells using Cu as the positive current collector and Al as the negative current collector. In their study, a self-charging cell left in discharge mode with an external resistor for approximately 8.6 months never dropped below 1.43 V, highlighting the persistent internal polarization effect of the $Na_{2.99}Ba_{0.005}OCl$ ferroionic and its potential for long-duration surface electronic feedback, maintenance-free energy systems.[157]

Although originally intended for battery applications, the ferroelectric/ferroionic nature of this electrolyte, along with the emergence of exotic surface states, makes it a promising candidate for broader technological uses, such as advanced switching applications. Braga *et al.*[6] reported two transistor-like structures: Au/$Li_{2.99}Ba_{0.005}OCl$/Au (Fig. 22) like the optical sensor Au/CCPS/Au (Fig. 22) and Zn/$Na_{2.99}Ba_{0.005}OCl$/C. Both configurations demonstrate the ability to overcome the Boltzmann tyranny, highlighting their potential for low-power electronic devices.

In summary, the studies discussed in this section highlight how the combination of mobile ions with ferroelectric character is redefining material functionalities, allowing reconfigurable states, tunable transport, and memory effects beyond conventional limits. These ferroionic architectures demonstrate the power of dynamic ionic-electronic coupling to induce new physical behaviors, from nonvolatile resistance switching to reversible polarization states. As understanding deepens, these systems are set to unlock transformative possibilities in adaptable, low-power electronic and neuromorphic applications.

C. Mechanical

Pressure sensors based on ferroionic and piezoelectric effects have attracted significant interest due to their potential for integration into flexible, wearable, and self-powered electronic systems. These sensors transduce mechanical deformation into electrical signals, taking advantage of the piezoelectricity or piezoresistivity of functional materials such as MoS_2 and $BaTiO_3$.

1. Pressure sensors

a. MoS_2 *(Table I)* MoS_2 has emerged as a promising material for pressure sensors due to its mechanical flexibility, high piezoresistive sensitivity, compatibility with flexible substrates, and very good mechanical transmittance.[208] Its tunable bandgap and strong interaction with mechanical deformation enable precise transduction of pressure stimuli into measurable electrical signals.[209] W. Park *et al.* demonstrated one of the earliest integrations of MoS_2 into pressure sensors, specifically a novel touch sensor, by fabricating a piezoelectric hybrid device using a PVDF-TrFE/MoS_2 composite stack. Additionally, the inclusion of a thin Al_2O_3 interfacial layer significantly enhanced sensitivity by enhancing interface passivation and reducing charge scattering. Optimizing the thickness of the PVDF–TrFE and Al_2O_3 layers also significantly increased the pressure sensitivity. The sensor showed high flexibility, reliable switching over 120 cycles, and suitability for tactile sensing.

M. Park *et al.*[209] created an ultrathin and flexible tactile sensor with MoS_2 and graphene electrodes using chemical vapor deposition (CVD). The design took advantage of the piezoresistive behavior of MoS_2, achieving high sensitivity and excellent mechanical properties. The sensors were tested for electronic skin (E-skin) applications and demonstrated real-time detection of pressure distributions, providing a foundation for future developments in biomedical devices and wearable electronics. In 2019, the group introduced a MoS_2-based active-matrix flexible tactile sensor, with integrated thin-film transistors and Al_2O_3 dielectrics.[210] By sandwiching MoS_2 between high-k dielectric Al_2O_3 layers, the device offered low crosstalk, high sensitivity (0.011 kPa^{-1}), fast response (~180 ms), and accurate multitouch detection on a human palm.[210] Dai *et al.*[211] showed that grain boundaries (GB) in monolayer MoS_2 enhance piezoelectric output due to polarization generated by asymmetric GBs. A flexible sensor using GB-MoS_2 on PDMS detected wrist pulses (~72 bpm), confirming its utility for self-powered sensing. Jang *et al.*[212] introduced MoS_2-based sensors integrating air-dielectric FETs and ZnS:Cu mechanoluminescent layers. This architecture achieved high spatial resolution and pressure sensitivity, from cellular motions to footsteps, via innovations like glycerol-loaded spacers and light-induced photocurrent amplification. Veeralingam *et al.*[213] developed a low-cost and flexible pressure and strain sensor using hand-written exfoliated MoS_2 on standard paper, a concept often designated as "papertronics." The device operated piezoresistively with high sensitivity, supporting compressive and tensile strain detection, and enabling disposable electronics. Chen *et al.*[214]

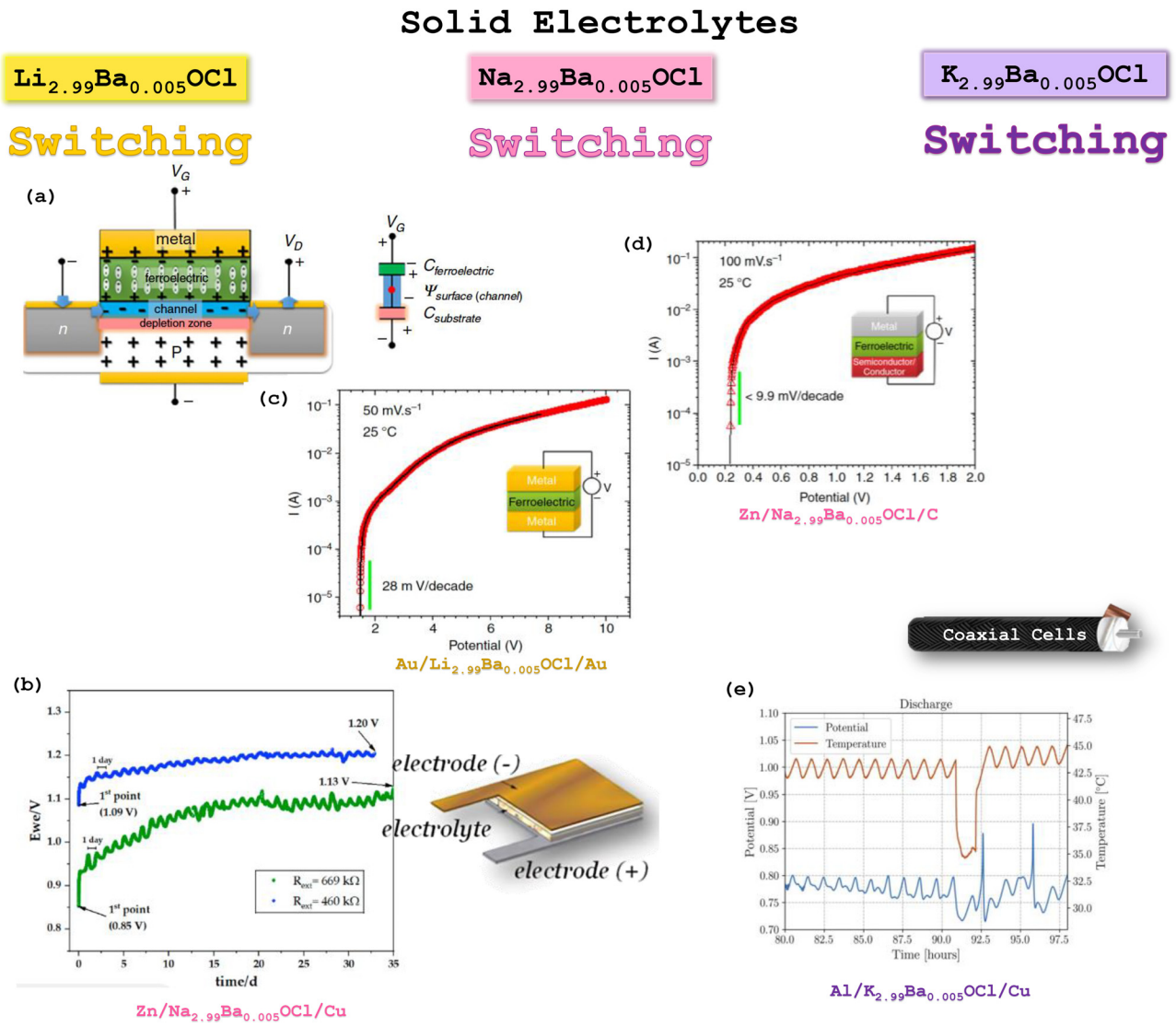

FIG. 22. Ferroionic all-solid-electrolytes for applications in switching devices. (a) Schematic of a FeFET in the "on" state: metal/ferroelectric/channel/depletion region/substrate structure modeled as two capacitors in series. (b) Discharge behavior of two pouch cells (Cu/carbon felt/$Na_{2.99}Ba_{0.005}ClO$-cellulose/Zn) with 669 kΩ (green) and 460 kΩ (blue) external resistors. Tafel plots of half gate-to-channel cells in a FeFET configuration: (c) Au/$Li_{2.99}Ba_{0.005}OCl$/Au and (d) Zn/$Na_{2.99}Ba_{0.005}OCl$/C. (e) All-solid-state Al/$K_{2.99}Ba_{0.005}ClO$ composite/Cu coaxial cell discharge profile highlighting potential vs temperature response. (b) Reproduced with permission from Freitas *et al.*, Int. J. Mol. Sci. **25**, 12694 (2024). Copyright 2024 Author(s), licensed under a Creative Commons Attribution (CC BY 4.0) license.[156] (e) Reproduced with permission from Danzi *et al.*, APL Mater. **10**, 031111 (2022). Copyright 2022 Author(s), licensed under a Creative Commons Attribution (CC BY 4.0) license.[158] (a), (c), and (d) Reproduced with permission from Braga *et al.*, Appl. Phys. Rev. **7**(1) 011406 (2020), with the permission of AIP Publishing.[6]

developed a MoS_2/HEC/PU sponge-based pressure sensor for motion tracking and speech recognition. Using a machine learning algorithm, the system classified seven spoken words with ∼97% accuracy by detecting throat vibrations. Choi *et al.*[215] combined PVDF/MoS_2/MXene layers on Nylon-6,6 fabric to create a hybrid triboelectric–piezoelectric sensor for simultaneous energy harvesting and movement detection. Integrated with a one-dimensional convolutional neural network (1D-CNN), it achieved >99% accuracy in gesture classification from body motions. Bokka *et al.*[216] designed a sustainable, water-soluble MoS_2/PVA sensor enabling reuse and full dissolution in water within 300 s, allowing for efficient recovery and recycling of MoS_2 with negligible performance loss (Fig. 23).

b. BTO (Table I) $BaTiO_3$ has been widely employed in flexible piezoelectric pressure sensors due to its high dielectric constant and ability to enhance the β-phase content in polymer matrices. Yang *et al.*[217] incorporated PDA-modified $BaTiO_3$ (PDA@BTO) into PVDF, improving nanoparticle dispersion and interfacial bonding, which significantly increased output voltage and mechanical responsiveness. Luo *et al.*[218] used near-field electrohydrodynamic writing to

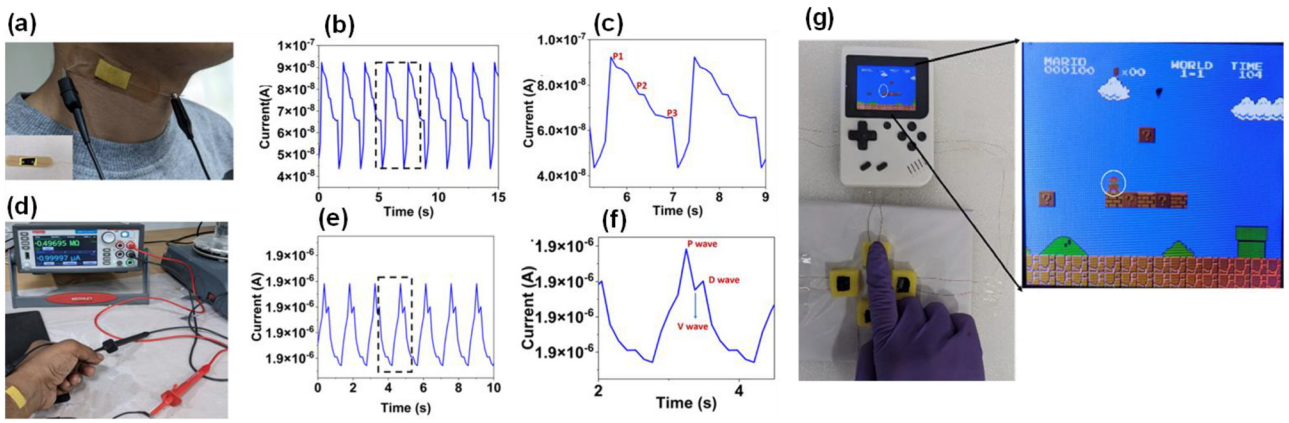

FIG. 23. (a) MoS_2/PVA pressure sensor integrated into a bandage applied to the neck area for pulse monitoring. (b) and (c) Sensor output capturing carotid pulse signals. (d)–(f) Pulse signals measured from the radial artery at the wrist. (g) Functional demonstration of the sensor as interactive input keys for a gaming application; shown here in use for controlling movement in a Mario game with the upward-direction key. Reproduced with permission from Bokka *et al.*, J. Mater. Chem. C **13**, 10804 (2025). Copyright 2025 Author(s), licensed under a Creative Commons Attribution (CC BY 4.0) license.[216]

fabricate fibrous PVDF/rGO/$BaTiO_3$ films. Here, reduced graphene oxide (rGO) enhanced conductivity and mechanical integrity, while $BaTiO_3$ retained piezoelectric functionality. Yang *et al.*[219] designed a wearable capacitive sensor using electrospun PVDF/$BaTiO_3$ fibers layered on a microstructured PDMS dielectric. Graphene-coated polyimide electrodes formed a compressible sandwich structure with enhanced dielectric performance.

He *et al.*[220] introduced a gradient multilayer structure of P(VDF-HFP)/MXene/$BaTiO_3$ nanofibers via electrospinning, improving the β-phase content and thus piezoelectric, dielectric, and mechanical properties. Liu *et al.*[221] functionalized $BaTiO_3$ with MXene nanosheets and electrospun the composite into PVDF-TrFE nanofibers. MXene improved nanoparticle dispersion, interfacial polarization, and output performance. Wang *et al.*[222] enhanced PVDF-TrFE sensors by co-doping with Sb nanosheets and $BaTiO_3$, increasing β-phase content, dielectric performance, and charge transport via interfacial polarization. Mirjalali *et al.*[223] proposed a layered sandwich design by electrospraying $BaTiO_3$ between PVDF-TrFE nanofiber layers. This configuration outperformed traditional dispersions, likely due to increased strain-induced effects in $BaTiO_3$. Yu *et al.*[224] developed a self-powered sensor combining $BaTiO_3$ and PAN in a silicone elastomer matrix. Mechanical shear and electric fields induced PAN conformational changes, enhancing piezoelectricity. Madbouly *et al.*[225] embedded rGO and $BaTiO_3$ into PU foam, achieving high sensitivity, fast response, and minimal hysteresis.

Collectively, these flexible pressure sensors, enabled by material innovations such as surface functionalization, hybrid fillers, and structured layering, have been successfully applied in real-time human motion monitoring, including finger and joint bending, walking, running, speech recognition, bite force detection, and pulse sensing. Their demonstrated performance highlights their strong potential for integration in wearable electronics, artificial skin, and soft robotics.

2. Strain sensors

Another key category of mechanical sensors is strain-based devices, which play a vital role in flexible and wearable electronics. They detect subtle deformations, such as stretching, bending, and twisting, by converting mechanical strain into measurable electrical signals. These are widely applied in health monitoring, soft robotics, and human-machine interfaces.

a. MoS_2 (Table I) Wu *et al.*[226] provided a foundational study by experimentally demonstrating the intrinsic piezoelectricity of monolayer MoS_2, mechanical strain generates voltage and current outputs only in odd-layered samples due to broken inversion symmetry. Strain-induced modulation of electrical transport (piezotronics) was further demonstrated, as well as high gauge factors for strain sensing. Wu *et al.*[227] demonstrated the piezophototronic effect in single-layer MoS_2 photodetectors, where mechanical strain modulated the Schottky barrier height at the metal-MoS_2 interface, enhancing photocurrent generation. Kim *et al.*[228] explored the directional dependence of the piezoelectric effect in CVD-grown monolayer MoS_2, showing that the magnitude of the output signal is sensitive to the strain direction relative to the crystal orientation, confirming anisotropic piezoelectric behavior critical for device design. Choi *et al.*[229] introduced asymmetry into MoS_2 films via a thermal-solvent annealing process that selectively etched sulfur atoms, breaking inversion symmetry. This defect engineering yielded an increase in output voltage, significantly enhancing piezoelectric performance in a scalable manner. Han *et al.*[230] introduced a strategy to enhance the piezoelectric output of CVD-grown monolayer MoS_2 nanogenerators via sulfur vacancy passivation. S-treatment suppressed carrier screening effects, increasing the piezoelectric coefficient, current, voltage, and power, demonstrating that defect control can dramatically enhance piezoelectric performance in scalable devices. Cao *et al.* 2022)[231] fabricated a flexible piezoelectric sensor by incorporating ZnO-encapsulated MoS_2 nanosheets into a PVDF matrix, forming a heterostructure that effectively promoted the transformation from α to β phase in PVDF. The device successfully sensed joint movement, demonstrating good flexibility and responsiveness to human motion, making it suitable for wearable sensing applications. Huang *et al.*[232] developed a highly sensitive flexible piezoelectric sensor based on a PAN/MXene/MoS_2 nanofiber film

with a novel gradient multilayer architecture. The design enhanced dipole alignment through 2D/2D heterostructure interactions, significantly improving the dielectric, ferroelectric, and piezoelectric properties, resulting in superior sensing performance and rapid response and recovery times. Tsai *et al.*[233] demonstrated highly uniform, wafer-scale flexible FETs based on trilayer MoS_2, exhibiting gate-tunable piezoresistive responses with gauge factors up to 40 and stable performance over 180 bending cycles. Strain-induced changes in the bandgap give rise to piezoresistivity in MoS_2, and tuning the Fermi level enables strain sensitivity control. Zheng *et al.*[234] employed kirigami-inspired structures in monolayer MoS_2 to achieve highly stretchable nanodevices capable of multidimensional deformation. By engineering the geometry of the 2D material, they enabled higher reversible strain ranges through a combination of in-plane stretching and out-of-plane buckling. Chhetry *et al.*[235] fabricated a highly sensitive, hysteresis-free, and durable strain sensor by laser-scribing MoS_2-decorated polyimide into porous graphene. The resulting device exhibited a giant gauge factor (∼1242), a broad strain range up to 37.5%, and long-term cycling stability (>12 000 cycles), showcasing its potential for wearable applications. Sridhar *et al.*[236] developed a highly sensitive etched fiber Bragg grating (eFBG) strain sensor enhanced by nanometer-thick MoS_2 coatings deposited via physical vapor deposition, followed by sulfurization. The optimal MoS_2 coating yielded a maximum intrinsic strain sensitivity nearly six times that of a bare FBG, due to strong evanescent field interaction and strain-induced refractive index modulation. Rana *et al.*[237] contributed with scalable fabrication of polycrystalline MoS_2 thin-film strain sensors, where tunable gauge factors (12 to 102) were achieved through variation in encapsulation thickness, making them well-suited for body motion tracking. Puneetha *et al.*[238] developed a flexible piezotronic device using CVD-grown monolayer MoS_2 thin films sandwiched between graphene layers on PET. Through strain engineering, the device exhibited high gauge factors, with the piezotronic effect being tunable via mechanical strain and temperature. The reduction of screening at cryogenic temperatures further enhanced performance, positioning the device for high-sensitivity applications in bioelectronics and soft robotics. Bhakhar *et al.*[239] introduced a biodegradable, low-cost, and flexible paper-based sensor functionalized with MoS_2 nanosheets obtained via sonochemical exfoliation. The device exhibited high responsivity and pressure sensitivity ($0.638\,kPa^{-1}$), retaining its performance after hundreds of cycles and 10 months of ambient storage, thanks to the environmental stability of MoS_2.

b. WS_2 (Table 1) Xu *et al.*[240] developed a planar photodetector based on a $WS_2/CsPbBr_3$ vdW heterostructure. The device exhibits a high on/off current ratio enabled by efficient photocarrier transfer from $CsPbBr_3$ to WS_2 and channel depletion effects that suppress dark current. Notably, when fabricated on flexible substrates, the device also demonstrates strain-tunable performance through the piezo-phototronic effect. Mechanical strain modulates interfacial charge transfer by altering band alignment via polarization in the $CsPbBr_3$, leading to significant changes in photocurrent and responsivity. These results demonstrate a novel strategy for realizing high-performance, energy-efficient systems with built-in mechanical responsiveness and multifunctional integration.

c. WSe_2 (Table 1) Lee *et al.*[241] investigated the piezoelectric properties of bilayer WSe_2 and demonstrated that a non-centrosymmetric structure, and consequently piezoelectricity, can be preserved by assembling monolayers using turbostratic stacking, rather than the usual Bernal configuration that cancels polarity. In this method, each monolayer, synthesized by CVD, is transferred independently, allowing misaligned orientations that break inversion symmetry in the bilayer. The resulting bilayers not only retain a measurable piezoelectric response but also display superior mechanical resilience. The energy harvested by these bilayers is sufficient to power small electronic components like an LCD, unlike monolayer-based devices, which degrade at lower strains. The latter work highlights the potential of turbostratically stacked WSe_2 as a scalable and durable material for flexible energy-harvesting systems.

d. α-In_2Se_3 (Fig. 1) Feng *et al.*[242] developed a scalable method for fabricating flexible, high-sensitivity strain sensor arrays using 2D α-In_2Se_3 films grown by vdW epitaxy CVD on mica. Their devices reached a gauge factor of up to 237 in a narrow strain range, outperforming conventional metal and graphene-based sensors. Patterned growth enabled arrays with high spatial resolution and mechanical durability, showing stable performance in real-time conditions such as wrist and elbow motion, and highlighting potential for E-skin applications in robotics and health monitoring. Dai *et al.*[243] introduced multilayer α-In_2Se_3 as a novel class of 2D vdW piezoelectrics with in-plane polarization alignment and strong piezoelectric response. Unlike traditional 2D materials, where interlayer dipole cancelation limits performance, α-In_2Se_3 maintains consistent polarization across layers, enabling thickness-dependent enhancement. This supports their use in flexible, durable, and self-powered sensors for wearable electronics and real-time health monitoring. Hou *et al.*[244] studied the effect of in-plane strain on the photoresponsivity of flexible transistors based on ferroelectric α-In_2Se_3. Applying small compressive strain enhanced performance under low light intensity due to the combined effects on carrier mobility and polarization-induced band structure modulation. Their findings demonstrate how static strain can be leveraged to tune optoelectronic properties in 2D ferroelectric semiconductors. Zhao *et al.*[245] explored the piezo-phototronic effect in α-In_2Se_3/WSe_2 heterostructure photodetectors. Mechanical strain modulated the band alignment at the p-n junction via α-In_2Se_3's intrinsic piezoelectricity, improving carrier separation and transport. The resulting device achieved high photoresponsivity and detectivity, showcasing its promise for strain-tunable optoelectronics.

Over the past decade, ferroionic mechanical sensors have advanced from simple stacked structures to sophisticated systems, enabling applications in electronic skin, human-machine interfaces, and wearable devices. Research highlights how incorporating ferroionic and ferroelectric materials into these sensors benefits innovations in material design, hybrid architectures, substrate engineering, and scalable fabrication techniques.

e. $Na_{2.99}Ba_{0.005}OCl$ $Na_{2.99}Ba_{0.005}OCl$ as a piezoelectric solid electrolyte is a promising candidate for mechanical sensing applications. Christoff *et al.* investigated the use of a $Zn/Na_{2.99}Ba_{0.005}OCl/Cu$ cell, traditionally studied as a battery, in a strain-sensing configuration under dynamic loading. To assess its sensing capabilities, the authors conducted vibrational tests by attaching the battery to an aluminum beam subjected to controlled excitation using a mechanical shaker, Fig. 24(a). The primary objective was to experimentally verify whether

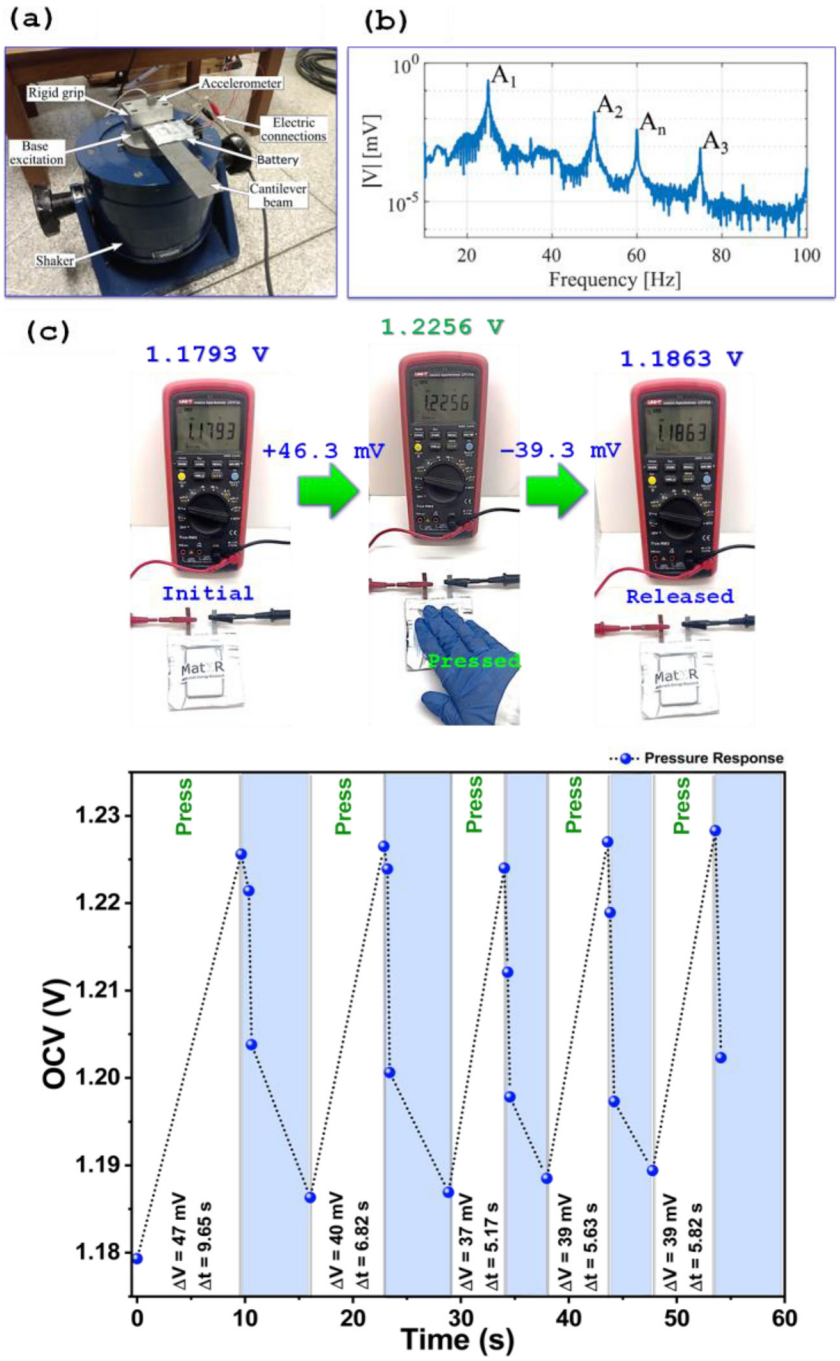

FIG. 24. (a) Illustration of a piezoelectric/ferroionic battery mounted on an aluminum beam with a shaker and accelerometer setup; (b) corresponding raw battery signal in the frequency domain. (c) Demonstration of pressure-induced response on a Cu/$Na_{2.99}Ba_{0.005}OCl$/Zn cell, highlighting the ferroionic electrolyte's piezoelectric potential (schematics obtained for this study). (a) and (b) Reproduced with permission from Christoff *et al.*, MSSP **215**, 111390 (2024). Copyright 2024 Author(s), licensed under a Creative Commons Attribution (CC BY 4.0) license.

the cell exhibits a piezoelectric response, specifically, whether it can generate a measurable voltage in response to bending-induced strain. The results showed voltage generation at lower vibration frequencies, where larger displacement amplitudes, and consequently, greater bending strains occur, Fig. 24(b). Among the tested parameters, vibration amplitude was identified as one of the most critical factors influencing the sensor's output. Authors also noted that while the tested configuration was initially designed for battery operation, optimized electrode and cell designs could further enhance sensing performance in future iterations. This material shows potential for use in pressure sensors, for example, in airplanes to detect structural failures.

An experimental setup was constructed using a battery with the configuration Zn/$Na_{2.99}Ba_{0.005}OCl$/Cu, which exhibited an initial OCV of 1.179 V, Fig. 24(c). The battery was connected to a multimeter, and

pressure was manually applied to its surface, Fig. 24(c). The user pressed the battery for a few seconds, typically between 5 and 10 h, Fig. 24(c). During the pressing period, the cell's potential difference increased, reaching a maximum of +47 mV after being pressed for 9.65 s, Fig. 24(c). Upon release, the voltage dropped back near the initial OCV. Repeating the pressure application resulted in another increase in voltage, followed again by a decrease upon release, clearly demonstrating sensor-like behavior, Fig. 24(c).

D. Thermal

Thermal sensors are used to measure physical input signals related to temperature variations, either directly or indirectly (Fig. 25). These sensors also detect temperature variations by absorbing radiation from a target object. The absorbed radiation induces changes in a temperature-dependent property of the sensor, which are then electrically measured.[246]

Pyroelectricity is the ability of certain materials to develop a temporary voltage when they are heated or cooled.[247–250] This occurs due to a change in the material's polarization caused by temperature variation. The pyroelectric mechanism is the basis for self-powered sensors sensitive to thermal perturbations, such as heat sensors, thermal imaging, and infrared (IR) sensors.[251] VdW 2D materials and different types of ferroelectric perovskites are usually applied in pyroelectric thermal sensors (PTS).[252] Other thermal sensors used in thermographic imaging rely on the optoelectronic properties of materials to determine the target's temperature, as the emission spectrum of a target varies with temperature.

a. MoS_2 (Table I). A high temperature coefficient of resistance (TCR) is just as important as low thermal hysteresis loss for rapid thermal sensing devices.[253,254] Mono-to few-layer MoS_2 nanosheets show a large direct bandgap (1.2–1.9 eV).[53,255,256] Temperature tracking in MoS_2-based sensors relies on analyzing charge carrier dynamics at specific temperatures. The carrier transport through the MoS_2 channel is affected by multiple scattering mechanisms, including phonon-phonon, electron-phonon, electron-defect, and phonon-defect interactions between the terminal electrodes.[257–260] Among these, phonon-phonon and electron-phonon scattering are the dominant temperature-dependent factors.[261]

In hybrid configurations, such as those incorporating rGO, phonon energy transfer to MoS_2 enhances carrier mobility. This reduces recombination rates and shortens carrier transit time, resulting in higher current output and improved sensor sensitivity.

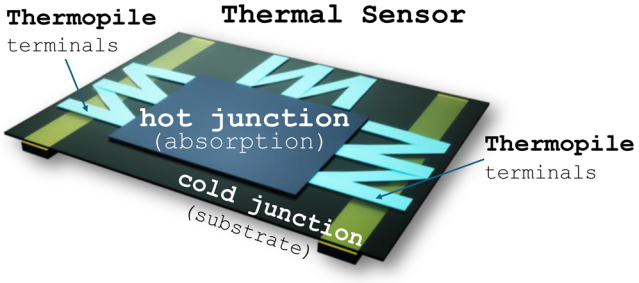

FIG. 25. Illustration of a thermal sensor. Thermal sensors used to measure physical input signals related to temperature variations, either directly or indirectly. Schematics designed for this study.

b. WS_2 (Table I). Lee *et al.*[262] investigated the use of WS_2 for fabricating on-paper thermal sensors, demonstrating their high sensitivity to temperature variations. An increase in temperature causes an abrupt decrease in the resistance of the WS_2 sensor.[262] This resistance drop cannot be described by a single exponential trend, indicating the occurrence of multiple thermally activated processes. The TCR for the WS_2 sensors reported here ranges from −20 000 to −160 000 ppm °C^{-1}.[262] In contrast, previously reported paper-based thermal sensors using graphite exhibited much lower TCR values, typically between −2500 and −3700 ppm °C^{-1}.[263,264] These results highlight the significantly higher temperature sensitivity of WS_2-based devices compared to earlier graphite-based sensors. To evaluate the response speed of the WS_2 sensor, the authors pre-heated it to 45 °C and then rapidly cooled it by blowing cool air onto its surface.[262] The sensor responded with an immediate increase in resistance, occurring within the instrumentation's acquisition time (∼0.2 s).[262] Following this sharp change, the resistance decayed exponentially as the sensor re-thermalized with the environment, exhibiting a recovery time of approximately 1 s, primarily limited by the system's specific heat and thermal conductivity.[262] The WS_2 thermal sensor is proposed for application in respiration monitoring devices. When the test user breathes over the sensor, the resistance drops by ∼8%, corresponding to a temperature increase of ∼1.5 °C.[262] During breathing tracking, the resistance oscillates due to temperature fluctuations induced by the inhaling/exhaling cycles. The magnitude of the resistance change reaches ∼2%–3%, being larger than in graphite-based (∼0.5%) and carbon nanotube-based (∼0.2%–0.3%)[265,266] thermoresistive breathing sensors.

c. WTe_2 (Table I). Faella *et al.*[267] reported the use of WTe_2 field-effect transistors (FETs) as temperature sensors operating in cryogenic regimes.[267] Recognizing that the properties of WTe_2 are sensitive to temperature variations,[268] the authors analyzed the FET resistance as a function of temperature, which was well described by a power-law relationship $(\rho(T) \propto T^{-b}$ where $b \approx 1.149 \pm 0.023)$.[267] During repeated heating and cooling cycles, the current levels remained stable, showing no significant fluctuations with increasing cycle number. The measurements demonstrated high repeatability, and no signs of sample degradation were observed.[267]

d. CIPS (Table I). Qiu *et al.*[269] reported a dual vdW heterostructure comprising $MoS_2/CuInP_2S_6/WSe_2$, which demonstrated sensitivity to subtle temperature changes induced by weak light ranging from ultraviolet to mid-infrared wavelengths. The device exhibited outstanding pyroelectric coefficients, exceeding 130 and 978 μC m^{-2}°C^{-1} for 45 and 70 nm CIPS layers, respectively.[269] This heterojunction achieved high detection accuracy, with a minimum detectable temperature change of just 0.1 K and an optical power detection range extending down to 1 μW cm^{-2}.[269] Additionally, it offered exceptional detectivity across various wavelengths. The authors also noted that the device maintained stable, self-powered detection performance for several months under natural environmental conditions, without noticeable degradation.[269]

e. PZT (Table I). Yang *et al.* manufactured a PTS sensor for detecting temperature at fingertips, composed of PZT microwires. As a result of PZT's superior pyroelectric coefficient, the PTS has a sensitivity of 0.4 K at room temperature. Succeeding the fingertip's surface temperature measurement, finger touch recognition was exhibited and applied for touch-based thermal haptics using thermal effects.[270] Due to the rapid dipole moment under thermal stimulation, the sensor demonstrated a fast response time of 0.9 s. The correlation between variation in temperature and voltage output is linear, easing effective calibration of the PTS.[270] The toxicity of lead limits the handling of these materials for wearable and epidermal applications.[247,252,254,270,271]

f. BNT (Fig. 1). Ferroelectric $Bi_{0.5}Na_{0.5}TiO_3$ (BNT) exhibits a reasonable pyroelectric coefficient of 50.74 $nC\,cm^{-2}\,°C^{-1}$ (Fig. 26).[272] Ji *et al.*[273] reported a self-powered thermal sensor based on an ITO/BNT/Ag structure, achieving a sensitivity of up to 27.6 $nC\,°C^{-1}$. This BNT-based sensor enabled a robotic hand to detect ambient temperature and assess thermal conductivity in real time, with a high accuracy of 97.2%.[273]

g. OIHPs (Fig. 1). Yakunin *et al.*[274] developed a high-speed, precise, and low-cost thermographic imaging method using *time-of-flight fluorescence lifetime imaging* (TOF-FLI) combined with thermally sensitive low-dimensional tin-halide materials such as $GuSnBr_4$ and Cs_4SnBr_6 ($Gu = Guanidinium = [C(NH_2)_3]^+$).[275] They demonstrated the technique using a compact prototype capable of video recording at up to 100 frames per second. The system successfully captured temperature dynamics through glass, something difficult for standard bolometric cameras due to IR absorption. The tin-halide materials exhibit strong temperature-dependent photoluminescence lifetimes, enabling sensitive thermal mapping over a wide temperature range (−100 to 110 °C). The latest results showed high spatial resolution and accuracy, with temperature precision comparable to commercial IR cameras.[276,277]

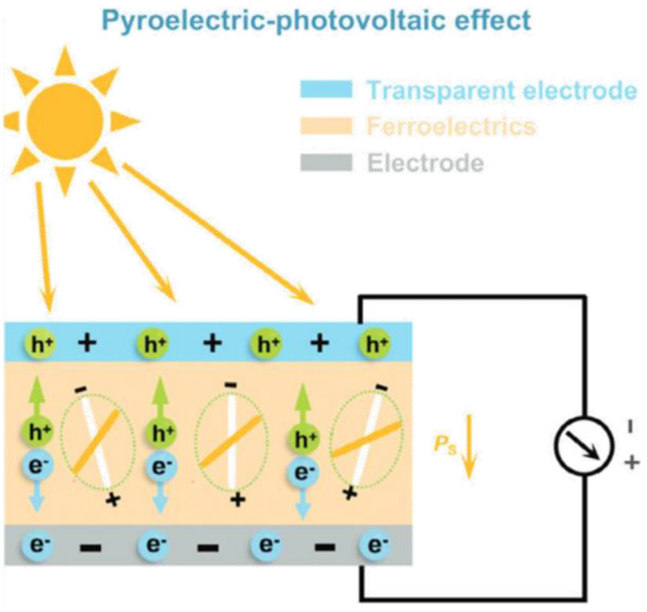

FIG. 26. Pyroelectric-photovoltaic effect working mechanism. Reproduced with permission from Yu *et al.*, Adv. Sensor Res. **3**, 2400049 (2024). Copyright 2024 Author(s), licensed under a Creative Commons Attribution (CC BY 4.0) license.[272]

The integration of ferroionic and low-dimensional materials into thermal sensing platforms has enabled a new generation of highly sensitive, fast, and self-powered devices capable of precise temperature detection across diverse operating regimes. From pyroelectric perovskites and layered TMDs to hybrid heterostructures, these systems demonstrate excellent temperature responsiveness, reproducibility, and versatility, even under challenging conditions like cryogenic temperatures or ultralow light exposure. Collectively, these advancements show the transformative potential of ferroionic materials in reshaping thermal sensing technologies, enabling innovative applications in healthcare, robotics, environmental monitoring, and beyond.

h. $K_{2.99}Ba_{0.005}OCl$ (Table I). Braga's group has been investigating the thermal response of the solid electrolyte $A_{2.99}Ba_{0.005}OCl$, where $A = Li^+$, Na^+, or K^+, for an extended period. Danzi *et al.* reported an all-solid-state coaxial cell with the composition $Al/K_{2.99}Ba_{0.005}OCl/Cu$, designed to discharge at room temperature through an external 1.8 kΩ resistor. Although the cell was intended to discharge continuously for 600 h, its potential never dropped below 0.8 V, exhibiting a self-charging behavior [Figs. 27(a) and 27(b)]. Notably, when the authors closely examined the voltage profile between 54 and 58 h, they observed that the self-charging behavior manifested as coherent oscillations, which matched with fluctuations in the cell's temperature. Specifically, during self-charging phases, when the cell voltage increased, there was a corresponding rise in temperature. Conversely, during discharge phases, the temperature decreased. This periodic temperature increase is closely associated with the self-charging cycles of the cell, and showcases the electrolytes potential to act as a thermal sensor.

i. $Na_{2.99}Ba_{0.005}OCl$ (Table I). A coaxial cell composed of $Al/Na_{2.99}Ba_{0.005}OCl/Cu$, reported by Danzi *et al.*,[157] showed outstanding thermal response by increasing the OCV from ≈0 to 0.9 V in 4.3 h just by increasing the system external temperature from 22 to 60 °C, keeping the potential difference of >0.4 V for T ≥40 °C during a period of 8 h. A maximum OCV value was achieved for 60 °C with the OCV value marking ∼1 V, Fig. 27(c). This experiment was simply reproduced, for this article, with a pouch cell battery with composition $Zn/Na_{2.99}Ba_{0.005}OCl/Cu$, showing an increase in OCV from 1.082 to 1.184 V, after warming the battery from 25.5 °C, with an external heat source to 78.4 °C in 72 s, Fig. 27(d).

E. Magnetic

Magnetic sensors are devices capable of detecting magnetic fields and converting this information into electrical signals for measurement or control applications. They are essential in a wide range of technologies, from navigation systems and medical devices to information storage and emerging quantum technologies. Their performance critically depends on material properties such as sensitivity, noise levels, and the ability to operate at room temperature.[278]

Among advanced magnetic sensing approaches, spintronic and ferroionic magnetic devices are gaining attention for their potential to

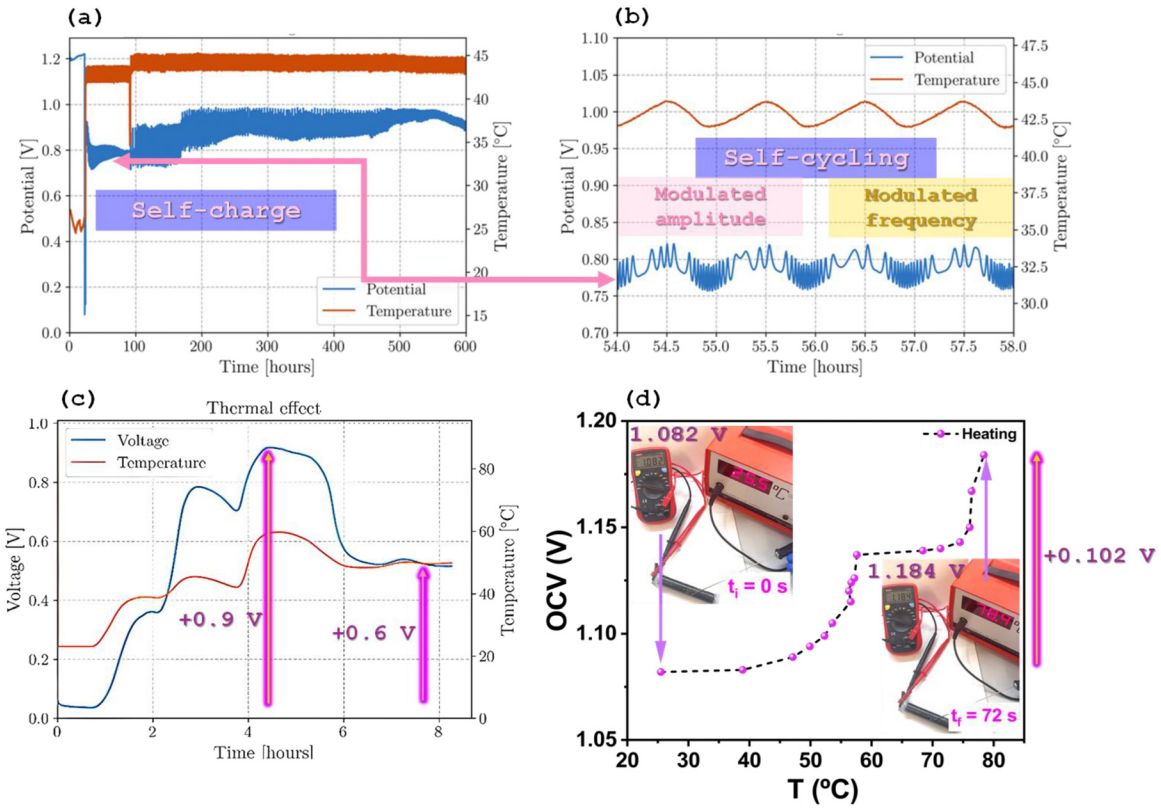

FIG. 27. All-solid-state Al/$K_{2.99}Ba_{0.005}ClO$ composite/Cu coaxial cell connected to an external 1.8 kΩ resistor self-charge profile highlighting potential vs temperature response, when the cell was heated at constant temperature of 40 °C; (a) full discharge (b) zoomed for time interval of 54–58 h. Reproduced with permission from Danzi *et al.*, APL Mater. **10**, 031111 (2022). Copyright 2022 Author(s), licensed under a Creative Commons Attribution (CC BY 4.0) license.[158] (c) Coaxial cell containing Al/$Na_{2.99}Ba_{0.005}ClO$ composite/Cu potential response vs thermal stimuli. Reproduced with permission from Danzi *et al.*, Molecules **26**(17), 5226 (2021). Copyright 2021 Author(s), licensed under a Creative Commons Attribution (CC BY 4.0) license.[157] (d) Thermal demonstrator Al/$Na_{2.99}Ba_{0.005}ClO$ composite/Cu coaxial cell, increase in 0.1 V after 72 s. Schematics obtained for this study.

combine high sensitivity, multifunctionality, and low power consumption, opening new possibilities for next-generation smart sensing systems.

a. MoS_2 (Table I). Yan *et al.*[59] demonstrated a two-dimensional spin field-effect switch based on a graphene/MoS_2 vdWs heterostructure, where spin current in graphene could be turned ON or OFF by tuning the gate voltage. This mechanism relies on gate-tunable spin absorption by MoS_2, acting as a spin sink. The latter work showcases the potential of using ferroionic 2D materials for creating reconfigurable spintronic elements that could be adapted for sensitive, field-controllable magnetic sensing applications (Fig. 28).

b. WS_2 (Table I). Zatko *et al.*[60] introduced vertical spin-valves using monolayer to trilayer WS_2 as tunnel barriers, revealing thickness-dependent spin polarization, including spin reversal in multilayers. This spin filtering arises from band structure effects and selection rules. These findings support the potential use of WS_2-based junctions in magnetic sensors where sensitivity and polarity could be tuned by atomic-layer control. Wees *et al.*[61] demonstrated a giant spin-relaxation anisotropy in bilayer-graphene/WS_2 heterostructures, enabling discrimination of in-plane and out-of-plane spin lifetimes. Although it is not a direct sensor, this anisotropy could be leveraged to design directionally sensitive quantum magnetic sensors.

c. BTO (Table I). Rouco *et al.*[279] demonstrated ferroionic control of spin polarization in a spin-memristor based on $La_{0.7}Sr_{0.3}MnO_3$ (LSMO)/$BaTiO_3$ (BTO)/ITO heterostructures. In this system, ion migration induced by electric fields modulated the spin polarization, enabling the reversal of the spin signal. Although primarily investigated for memory applications, this coupling between ionic motion and spin transport positions ferroionic perovskite structures as promising platforms for novel magnetic sensing concepts, particularly for reconfigurable and multifunctional sensors.

Additional materials with potential applications in spintronic and ferroionic magnetic devices include VSe_2, Fe_3GeTe_2 (FGT), and hBN. Jimenez *et al.*[280] demonstrated a magnetic sensor where a single-layer VSe_2 film was integrated into an LC resonator structure. The sensor operated by detecting shifts in the resonance frequency under external magnetic fields, reaching a remarkably high sensitivity of

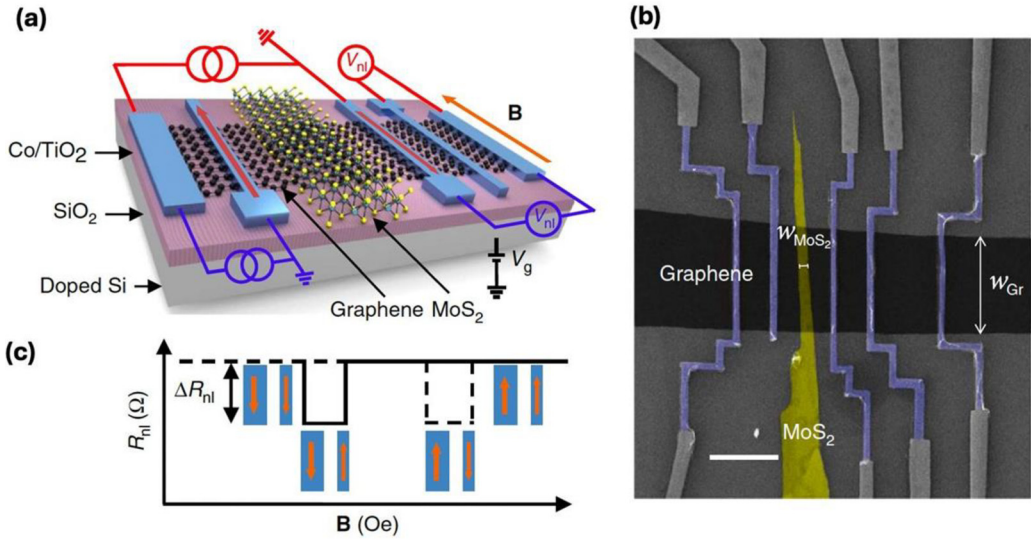

FIG. 28. (a) Schematic of a 2D vdW heterostructure to control spin transport in lateral spin valve. (b) False-color SEM image of the device. (c) Illustration of a typical non-local magnetoresistance measurement. Reproduced with permission from Yan *et al.*, Nat Commun. **7**, 13372 (2016). Copyright 2026 Author(s), licensed under a Creative Commons Attribution (CC BY 4.0) license.[59]

16×10^6 Hz.Oe^{-1}. The 2D nature of VSe_2 allowed for enhanced interaction with external stimuli, highlighting the potential of vdW magnets for compact, high-sensitivity magnetic sensors operating at ambient conditions. Wang *et al.*[281] introduced a strain-sensitive magnetization control approach using FGT. In their work, tensile strain applied to FGT flakes significantly modified the coercive field (H_c) and T_c, suggesting a pathway to design strain-controlled magnetic sensors. Although not a direct magnetic sensor yet, the strain-sensitivity of magnetization opens the door for "straintronic" magnetic sensors that could potentiate lattice deformation for magnetic field detection and control. Gottscholl *et al.*[282] explored spin defects in hBN, particularly negatively charged boron vacancies (V_B^-). These defects exhibited optically detectable magnetic resonance and sensitivity to magnetic fields, temperature, and pressure. Due to the layered nature of hBN and the proximity of defects to external environments, hBN-based spin systems are highly suited for nanoscale quantum sensing, enabling atomic-scale magnetic field imaging with high spatial resolution. Gao *et al.*[283] reported spin defects in boron nitride nanotubes (BNNTs). Unlike planar hBN, defects or diamond nitrogen-vacancy (NV) centers, BNNT spin defects possess an $S = 1/2$ ground state without a fixed quantization axis, enabling omnidirectional magnetic field sensing. Their tubular geometry and atomic-scale size offer unique opportunities for ultra-compact, orientation-independent quantum magnetic sensors.

These studies illustrate the transformative potential of spintronic and ferroionic materials in advancing magnetic sensor technology. Harnessing properties such as gate-tunability, spin filtering, strain sensitivity, and optically addressable spin defects enables high-performance, reconfigurable, and even quantum-level sensing. As research progresses, integrating these novel materials into practical devices may unlock a new generation of compact, energy-efficient, and multifunctional magnetic sensors tailored for diverse applications, from precision navigation to next-generation quantum technologies.

IV. OUTLOOK AND PERSPECTIVE

The integration of ferroelectric and ferroionic materials into quantum devices has revealed new paradigms for charge modulation, sensing, and non-contact energy transfer (Fig. 29). Among the materials discussed, the $A_{3-2x}Ba_xOCl$ family (A = Li, Na, K) has emerged as a particularly rich model system, combining ferroionic conductivity with robust, nonvolatile electrostatic behavior and long-range coherent interactions across interfaces and even air gaps. Yet, this development represents only one facet of a rapidly expanding field that now spans from layered van der Waals ferroelectrics to hybrid perovskites and classical oxide systems—each contributing unique physical mechanisms and functionalities to the ferroionic paradigm.

In Cu-based thiophosphates such as CIPS and CCPS, ferroelectricity arises from the displacement of Cu^+ ions within sulfur-based octahedra, producing vertical dipoles and switchable polarization at room temperature. These materials illustrate how layered van der Waals structures can host stable polarization in the absence of strong interlayer coupling, paving the way for ultrathin ferroelectric and multiferroic devices. However, their ionic motion is typically limited to Cu^+ hopping, resulting in modest ferroionicity and partial screening of polarization fields. The coupling of ferroelectricity to electronic states in these systems has already enabled memristive and tunneling junctions, and further interface engineering could lead to hybrid ferroelectric–ferroionic architectures with lateral ionic mobility.

Transition-metal dichalcogenides, including MoS_2 and WSe_2, represent another class of 2D ferroelectrics that exploit symmetry breaking through in-plane strain, stacking order, or atomic displacement. Their ferroelectricity, often stabilized in the 1T′ or 1T″ phases, can coexist with semiconducting or topologically non-trivial electronic bands. While their ferroionic properties are confined to ultra-thin regimes, the atomic precision and tunability of TMDs make them ideal for heterostructures where ferroelectric and ionic polarization can be controlled via interfacial gating or ionic intercalation—an emerging

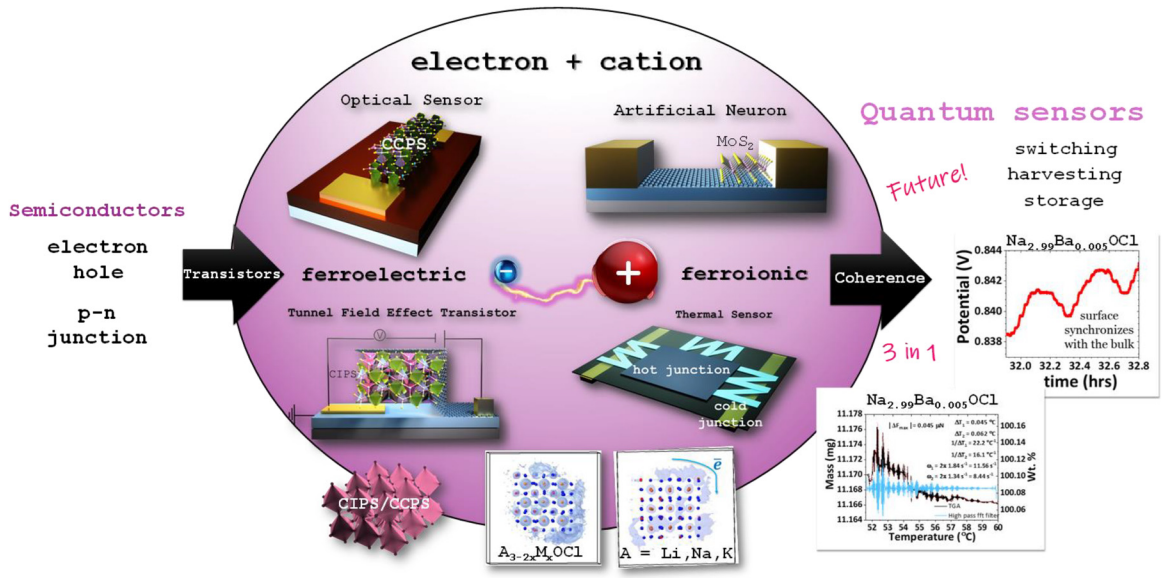

FIG. 29. Past-present-future (schematics designed for this study): from semiconductors to room temperature coherent quantum sensors with ferroelectric and ferroionic materials. The electron localization function ELF in a Na_3OCl cube, and the self-cycling graphs were adapted from M. H. Braga, Chem. Commun. **60**, 5395–5398 (2024). Copyright 2024 Author(s), licensed under a Creative Commons Attribution (CC BY 4.0) license.[64]

strategy for quantum information transduction and polarization-mediated spin control.

Hybrid halide perovskites, typified by $MAPbI_3$, bring another perspective: they exhibit dynamic molecular dipoles (from the organic A-site cation) coupled to deformable Pb–I octahedra. These materials bridge the electronic, ionic, and ferroelectric worlds naturally. Their strong photoresponse, soft lattice, and defect-tolerant chemistry enable polarization-assisted charge separation and hysteretic current–voltage behavior reminiscent of ferroionic switching. Despite challenges with environmental stability and halide migration, compositional engineering (e.g., FA/Cs alloying and Pb/Sn substitution) continues to stabilize ferroelectricity and tune ion transport, making halide perovskites central to both photoferroelectric and ferroionic photovoltaic research.

Classical perovskites such as $BaTiO_3$ remain benchmark ferroelectrics due to their well-defined Ti^{4+} displacement within oxygen octahedra, large spontaneous polarization, and established domain engineering. Doping and nanostructuring have progressively introduced ionic transport channels into these systems, yielding mixed ferroelectric-ionic conduction that could be exploited for solid-state synapses and reconfigurable capacitors. When combined with 2D or glassy ferroionics, $BaTiO_3$-based systems may provide the structural rigidity and dielectric stability needed for scalable architectures. The ferroelectricity in $Hf_{1-x}Zr_xO_2$ is a size- and strain-stabilized structural phenomenon, where the orthorhombic $Pca2_1$ phase emerges from constrained lattice distortion and selective doping, giving rise to switchable polarization at nanometer scale—a "ferroelectricity by design" rather than by intrinsic instability. It is often described as a distorted sevenfold coordination—between octahedral (sixfold) and cubic (eightfold). This kind of ferroelectricity enables FeFETs for nonvolatile memory, negative capacitance transistors that beat the Boltzmann limit, and CMOS-compatible integration, as HfO_2 is already used as a high-k gate dielectric.

In this broader landscape, $A_{3-2x}Ba_xOCl$ compounds distinguish themselves by achieving bulk ferroionicity—stable, reconfigurable polarization sustained through aliovalent doping and vacancy dynamics in semi-amorphous matrices. Unlike van der Waals or hybrid perovskites, the absence of long-range crystallinity does not suppress their polarization memory. Instead, disordered local environments enhance ionic polarizability and allow persistent electric field gradients that extend across macroscopic distances. Their mobile ions do not fully screen internal fields allowing electrons to circulate along the surface, suggesting topologically active edge states. This behavior underpins self-charging, self-cycling, and structured air-gap capacitance—phenomena pointing toward ferroelectric topological insulators and new paradigms of non-contact electrostatic communication.

From a conceptual viewpoint, all ferroionic materials—whether crystalline, layered, hybrid, or glassy—share a common octahedral coordination motif as the structural cradle of polarization. Yet, their responses diverge dramatically depending on how symmetry, dimensionality, and disorder govern the coupling between electronic and ionic degrees of freedom. This diversity emphasizes a unifying design principle: *ferroionic functionality emerges when local polar distortions are dynamically coupled to mobile ions that can mediate long-range order without electronic conduction.*

Looking ahead, several challenges and opportunities define the path forward. Achieving reversible ferroionic switching under device operation requires improved control of vacancy dynamics, interface stability, and fatigue mechanisms. The development of operando

multimodal probes-combining SKP, PFM, and time-resolved spectroscopy—will be crucial to visualize coupled ionic-electronic phenomena at the nanoscale. On the theoretical side, multiscale simulations that integrate DFT-level potential landscapes with mesoscale ionic kinetics are needed to capture ferroionic polarization dynamics beyond static approximations. Finally, hybrid heterostructures that combine van der Waals ferroelectrics, oxide ferroionics, and halide perovskites could yield programmable devices with tunable charge–ion coupling for neuromorphic, quantum-sensing, and self-powered architectures.

In conclusion, the emerging field of ferroionics bridges long-separated domains—ferroelectricity, ionics, and topology—into a unified physical framework. From ordered oxides to disordered halides and chalcogenides, these materials redefine what constitutes a polar solid, introducing functionalities that transcend conventional dielectric or electrochemical limits. The continued exploration of this class promises not only to deepen our understanding of collective charge phenomena but also to catalyze the design of autonomous, adaptive, and sustainable quantum devices for the next technological era.

ACKNOWLEDGMENTS

During the preparation of this manuscript, the authors used ChatGPT (August 2025 versions, developed by OpenAI) to enhance the fluency of the text. All generated content was reviewed and edited by the authors, who take full responsibility for the final publication. This work was supported by the Portuguese Foundation for Science and Technology FCT UID/50022/2025 LAETA–Thematic line 06. This work supported by Agenda NGS—New Generation Storage (Investment Project No. 58), financed by the Recovery and Resilience Plan (PRR) (Grant No. C644936001-00000045), European Union—NextGeneration EU by FEDER - Fundo Europeu de Desenvolvimento Regional funds through the COMPETE 2030 in the framework of the project COMPETE2030-FEDER-00890300, "Hybrid optical fibEr seNsors for monItorinG in real tiMe the next generation of solid-stAte cells"—ENIGMA (Project No. 15239), and the European Union's Horizon Europe research and innovation program (PULSELiON) (Grant No. 101069686). The views and opinions expressed are those of the authors and do not necessarily reflect those of the European Union or CINEA. Neither the European Union nor the granting authority can be held responsible for them.

AUTHOR DECLARATIONS

Conflict of Interest

The authors have no conflicts to disclose.

Author Contributions

Beatriz M. Gomes and Tomás Prior contributed equally to this paper.

Beatriz M. Gomes: Writing – original draft (equal); Writing – review & editing (equal). **Tomás Prior:** Writing – original draft (equal). **Ângela Freitas:** Writing – original draft (supporting). **António B. Vale:** Writing – original draft (supporting). **Beatriz A. Maia:** Writing – original draft (supporting). **Hugo Lebre:** Writing – original draft (supporting). **Manuela C. Baptista:** Writing – original draft (supporting). **Raquel Dantas:** Writing – original draft (supporting). **Maria Helena Braga:** Conceptualization (lead); Funding acquisition (lead); Supervision (lead); Writing – original draft (equal); Writing – review & editing (equal).

DATA AVAILABILITY

Data sharing is not applicable to this article as no new data were created or analyzed in this study.

REFERENCES

[1]Y. Zhou *et al.*, "Out-of-plane piezoelectricity and ferroelectricity in layered α-In2Se3 nanoflakes," Nano Lett. **17**(9), 5508–5513 (2017).
[2]H. Sun *et al.*, "Prominent size effects without a depolarization field observed in ultrathin ferroelectric oxide membranes," Phys. Rev. Lett. **130**(12), 126801 (2023).
[3]Y. Sun *et al.*, "Hybrid System combining two-dimensional materials and ferroelectrics and its application in photodetection," ACS Nano **15**(7), 10982–11013 (2021).
[4]W. Niu *et al.*, "Recent advances in memristors based on two-dimensional ferroelectric materials," Front. Phys. (Beijing) **19**(1), 13402 (2024).
[5]D. Damjanovic, "Ferroelectric, dielectric and piezoelectric properties of ferroelectric thin films and ceramics," Rep. Prog. Phys. **61**(9), 1267 (1998).
[6]M. H. Braga, J. E. Oliveira, A. J. Murchison, and J. B. Goodenough, "Performance of a ferroelectric glass electrolyte in a self-charging electrochemical cell with negative capacitance and resistance," Appl. Phys. Rev. **7**(1), 011406 (2020).
[7]T.-X. Xu *et al.*, "Emerging van der Waals material CuInP2S6: Physical properties, theories and applications," J. Mater. Chem. A Mater. **12**(45), 31028–31058 (2024).
[8]J. F. Scott, "Applications of modern ferroelectrics," Science (1979) **315**(5814), 954–959 (2007).
[9]Z. Wen *et al.*, "2D Van Der Waals ferroelectric materials and devices for neuromorphic computing," Small **21**(29), 2412761 (2025).
[10]A. N. Morozovska *et al.*, "Dynamic control of ferroionic states in ferroelectric nanoparticles," Acta Mater. **237**, 118138 (2022).
[11]A. N. Morozovska, E. A. Eliseev, N. V. Morozovsky, and S. V. Kalinin, "Ferroionic states in ferroelectric thin films," Phys. Rev B **95**(19), 195413 (2017).
[12]D. K. Kushvaha, S. K. Rout, and B. Tiwari, "Density dependent ionic transport in polycrystalline SrNb2O6 ceramic," Phys. B: Condens. Matter **579**, 411910 (2020).
[13]A. P. dos Santos, F. Jiménez-Ángeles, A. Ehlen, and M. Olvera de la Cruz, "Modulation of ionic conduction using polarizable surfaces," Phys. Rev. Res. **5**(4), 43174 (2023).
[14]Z. Wang, Q. Wang, L. Quan, and S. Ren, "reversible ferroelectric polarization modulation of chiral molecular ferroelectrics by circularly polarized light," Adv. Sci. **12**(10), 2414977 (2025).
[15]M. Asif and A. Kumar, "Resistive switching in emerging materials and their characteristics for neuromorphic computing," Mater. Today Electron. **1**, 100004 (2022).
[16]R. K. Mishra, K. Verma, and D. Sethi Singh, "Defect engineering in nanomaterials: Impact, challenges, and applications," Smart Mater. Manuf. **2**, 100052 (2024).
[17]A. N. Morozovska, E. A. Eliseev, A. K. Tagantsev, S. L. Bravina, L.-Q. Chen, and S. V. Kalinin, "Thermodynamics of electromechanically coupled mixed ionic-electronic conductors: Deformation potential, Vegard strains, and flexoelectric effect," Phys. Rev. B **83**(19), 195313 (2011).

[18]J. Lee *et al.*, "Free-standing two-dimensional ferro-ionic memristor," Nat. Commun. **15**(1), 5162 (2024).
[19]T. Eshita *et al.*, "Development of ferroelectric RAM (FRAM) for mass production," in Proceedings of the *2014 Joint IEEE International Symposium on the Applications of Ferroelectric, International Workshop on Acoustic Transduction Materials and Devices and Workshop on Piezoresponse Force Microscopy, ISAF/IWATMD/PFM 2014* (Institute of Electrical and Electronics Engineers Inc., 2014).
[20]"2017 Mass production of FeRAM s that can operate at temperatures of up to 125 °C started (RAMXEED)," Semiconductor History Museum of Japan, Management: SSIS, History Museum Committee, see https://www.shmj.or.jp/en/integrated-circuits/ic201001e.html; accessed: Nov. 13, 2025.
[21]M. H. Park, Y. H. Lee, T. Mikolajick, U. Schroeder, and C. S. Hwang, "Review and perspective on ferroelectric HfO2-based thin films for memory applications," MRS Commun. **8**(3), 795–808 (2018).
[22]B. M. Gomes, J. Holtz, M. L. Pinto, and M. H. Braga, "Polaronic and electrochemical signatures in group IVB (Ti, Zr, Hf) oxides: Unified SKP–DFT Insights for tunable transport in energy and electronic devices," Adv. Funct. Mater. **n/a**, e09853 (2025).
[23]T. S. Böscke, J. Müller, D. Bräuhaus, U. Schröder, and U. Böttger, "Ferroelectricity in hafnium oxide thin films," Appl. Phys. Lett. **99**(10), 102903 (2011).
[24]J. Lee *et al.*, "Role of oxygen vacancies in ferroelectric or resistive switching hafnium oxide," Nano Converg. **10**(1), 55 (2023).
[25]B. Mandal, A.-M. Philippe, N. Valle, E. Defay, T. Granzow, and S. Glinsek, "Ferroelectric HfO2–ZrO2 multilayers with reduced wake-up," ACS Omega **10**(13), 13141–13147 (2025).
[26]S. Zhukov, Y. A. Genenko, and H. von Seggern, "Experimental and theoretical investigation on polarization reversal in unfatigued lead-zirconate-titanate ceramic," J. Appl. Phys. **108**(1), 014106 (2010).
[27]S. Beyer *et al.*, "FeFET: A versatile CMOS compatible device with game-changing potential," in Proceedings of the *2020 IEEE International Memory Workshop (IMW)* (IEEE, 2020), pp. 1–4.
[28]P. Meng *et al.*, "Sliding induced multiple polarization states in two-dimensional ferroelectrics," Nat. Commun. **13**(1), 7696 (2022).
[29]L. Molino, L. Aggarwal, V. Enaldiev, R. Plumadore, V. I. Fal'ko, and A. Luican-Mayer, "Ferroelectric switching at symmetry-broken interfaces by local control of dislocations networks," Adv. Mater. **35**(38), 2207816 (2023).
[30]R. Frisenda, Y. Niu, P. Gant, M. Muñoz, and A. Castellanos-Gomez, "Naturally occurring van der Waals materials," NPJ 2D Mater. Appl. **4**(1), 38 (2020).
[31]Y. Hassan *et al.*, "Twist-controlled ferroelectricity and emergent multiferroicity in WSe2 bilayers," Adv. Mater. **36**(46), 2406290 (2024).
[32]Q. Zhou *et al.*, "Enhanced polarizability and tunable diamagnetic shifts from charged localized emitters in WSe2 on a relaxor ferroelectric," arXiv:2409.07687 (2024).
[33]A. Simon, J. Ravez, V. Maisonneuve, C. Payen, and V. B. Cajipe, "Paraelectric-ferroelectric transition in the lamellar thiophosphate CuInP2S6," Chem. Mater. **6**(9), 1575–1580 (1994).
[34]Z. Zhong *et al.*, "Robust threshold-switching behavior assisted by Cu migration in a ferroionic CuInP2S6 heterostructure," ACS Nano **17**(13), 12563–12572 (2023).
[35]K. Cho, S. Lee, R. Kalaivanan, R. Sankar, K.-Y. Choi, and S. Park, "Tunable ferroelectricity in Van der Waals layered antiferroelectric CuCrP2S6," Adv. Funct. Mater. **32**(36), 2204214 (2022).
[36]W. F. Io *et al.*, "Direct observation of intrinsic room-temperature ferroelectricity in 2D layered CuCrP2S6," Nat. Commun. **14**(1), 7304 (2023).
[37]S. W. Kim *et al.*, "Electrical properties and phase of BaTiO3–SrTiO3 solid solution," Ceram. Int. **39**, S487–S490 (2013).
[38]X. Wang *et al.*, "Electroresistance of Pt/BaTiO3/LaNiO3 ferroelectric tunnel junctions and its dependence on BaTiO3 thickness," Mater. Res. Express **6**(4), 046307 (2019).
[39]I. Tenreiro *et al.*, "Photovoltaic sensing of a memristor based in LSMO/BTO/ITO ferroionic tunnel junctions," Appl. Phys. Lett. **120**(3), 034101 (2022).
[40]K. Wasa, T. Matsushima, H. Adachi, T. Matsunaga, T. Yanagitani, and T. Yamamoto, "High-Tc/high-coupling relaxed PZT-based single crystal thin films," J. Appl. Phys. **117**(12), 124106 (2015).
[41]Y. Jo *et al.*, "Epitaxial PZT film-based ferroelectric field-effect transistors for artificial synapse," ACS Appl. Electron. Mater. **5**(8), 4549–4555 (2023).
[42]J. Breternitz, F. Lehmann, S. A. Barnett, H. Nowell, and S. Schorr, "Role of the iodide–methylammonium interaction in the ferroelectricity of CH3NH3PbI3," Angew. Chem. Int. Ed. **59**(1), 424–428 (2020).
[43]D. Zhang, P. Schoenherr, P. Sharma, and J. Seidel, "Ferroelectric order in van der Waals layered materials," Nat. Rev. Mater. **8**(1), 25–40 (2022).
[44]Y.-T. Huang *et al.*, "Two-dimensional In2Se3: A rising advanced material for ferroelectric data storage," InfoMat **4**(8), e12341 (2022).
[45]Q. H. Wang, K. Kalantar-Zadeh, A. Kis, J. N. Coleman, and M. S. Strano, "Electronics and optoelectronics of two-dimensional transition metal dichalcogenides," Nat. Nanotechnol. **7**(11), 699–712 (2012).
[46]W. Han *et al.*, "Recent advances of phase transition and ferroelectric device in two-dimensional In2Se3," Appl. Phys. Rev. **11**(2), 021314 (2024).
[47]C. Xu *et al.*, "Two-dimensional antiferroelectricity in nanostripe-ordered In2Se3," Phys. Rev. Lett. **125**(125), 047601 (2020).
[48]F. Xue *et al.*, "Multidirection piezoelectricity in mono- and multilayered hexagonal α-In2Se3," ACS Nano **12**(5), 4976–4983 (2018).
[49]Z. Tang, M. Dai, Y. Chen, Q. He, X. Luo, and Y. Zheng, "Strain engineering the ferroelectric polarization and optical absorption in the FEβ-In2Se3 monolayer," J. Phys. Chem. C **126**(24), 10181–10189 (2022).
[50]C. Xu *et al.*, "Two-dimensional ferroelasticity in van der Waals β'-In2Se3," Nat. Commun. **12**(1), 3665 (2021).
[51]X. He *et al.*, "Proton-mediated reversible switching of metastable ferroelectric phases with low operation voltages," Sci. Adv. **9**(21), eadg4561 (2023).
[52]Y. Long *et al.*, "Competing ferroelectric polarization and defect migration induced resistive switching in β'-In2Se3," Nano Lett. **25**(7), 2922–2930 (2025).
[53]K. F. Mak, C. Lee, J. Hone, J. Shan, and T. F. Heinz, "Atomically thin ${\mathrm{MoS}}_{2}$: A new direct-gap semiconductor," Phys. Rev. Lett. **105**(13), 136805 (2010).
[54]B. Radisavljevic, A. Radenovic, J. Brivio, V. Giacometti, and A. Kis, "Single-layer MoS2 transistors," Nat. Nanotechnol. **6**(3), 147–150 (2011).
[55]O. Lopez-Sanchez, D. Lembke, M. Kayci, A. Radenovic, and A. Kis, "Ultrasensitive photodetectors based on monolayer MoS2," Nat. Nanotechnol. **8**(7), 497–501 (2013).
[56]S. Bertolazzi, J. Brivio, and A. Kis, "Stretching and breaking of ultrathin MoS2," ACS Nano **5**(12), 9703–9709 (2011).
[57]A. Lipatov *et al.*, "Direct observation of ferroelectricity in two-dimensional MoS2," NPJ 2D Mater. Appl. **6**(1), 18 (2022).
[58]W. Zhao *et al.*, "Evolution of electronic structure in atomically thin sheets of WS2 and WSe2," ACS Nano **7**(1), 791–797 (2013).
[59]W. Yan, O. Txoperena, R. Llopis, H. Dery, L. E. Hueso, and F. Casanova, "A two-dimensional spin field-effect switch," Nat. Commun. **7**(1), 13372 (2016).
[60]V. Zatko *et al.*, "Band-structure spin-filtering in vertical spin valves based on chemical vapor deposited WS2," ACS Nano **13**(12), 14468–14476 (2019).
[61]S. Omar, B. N. Madhushankar, and B. J. van Wees, "Large spin-relaxation anisotropy in bilayer-graphene/WS_2 heterostructures," Phys. Rev. B **100**(15), 155415 (2019).
[62]D. Puggioni and J. M. Rondinelli, "Designing a robustly metallic noncenstrosymmetric ruthenate oxide with large thermopower anisotropy," Nat. Commun. **5**(1), 3432 (2014).
[63]M. H. Braga, "Coherence in the ferroelectric A3ClO (A = Li, Na) family of electrolytes," Materials **14**(9), 2398 (2021).
[64]M. H. Braga, "Energy harnessing and storage from surface switching with a ferroelectric electrolyte," Chem. Commun. **60**(41), 5395–5398 (2024).
[65]V. Maisonneuve, M. Evain, C. Payen, V. B. Cajipe, and P. Molinié, "Room-temperature crystal structure of the layered phase CuIInIIIP2S6," J. Alloys Compd. **218**(2), 157–164 (1995).
[66]A. Grzechnik, V. B. Cajipe, C. Payen, and P. F. McMillan, "Pressure-induced phase transition in ferrielectric CuInP2S6," Solid State Commun. **108**(1), 43–47 (1998).
[67]В. Біганич, І. Куриця, В. Шуста, and О. Герзанич, "Phase transitions of CuInP2(SexS1-x)6 in diapazon crystals at comprehensive compression and p,T,x-diagrams," Sci. Herald Uzh. Univ. Ser. Phys. **27**, 21–28 (2010).
[68]P. P. Guranich, A. G. Slivka, V. S. Shusta, O. O. Gomonnai, and I. P. Prits, "Optical and dielectric properties of CuInP2S6 layered crystals at high hydrostatic pressure," J. Phys.: Conf. Ser. **121**(2), 022015 (2008).

[69]A. Dziaugys, J. Banys, and Y. Vysochanskii, "Broadband dielectric investigations of indium rich CuInP2S6 layered crystals," Crystalline Materials, **226**(2), 171–176 (2011).
[70]L. You *et al.*, "Origin of giant negative piezoelectricity in a layered van der Waals ferroelectric," Sci. Adv. **5**(4), eaav3780 (2019).
[71]J. A. Brehm *et al.*, "Tunable quadruple-well ferroelectric van der Waals crystals," Nat. Mater. **19**(1), 43–48 (2020).
[72]S. Zhou, L. You, H. Zhou, Y. Pu, Z. Gui, and J. Wang, "Van der Waals layered ferroelectric CuInP2S6: Physical properties and device applications," Front. Phys. (Beijing) **16**(1), 13301 (2021).
[73]F. Liu *et al.*, "Room-temperature ferroelectricity in CuInP2S6 ultrathin flakes," Nat. Commun. **7**, 1–6 (2016).
[74]S. M. Neumayer *et al.*, "Alignment of polarization against an electric field in van der Waals ferroelectrics," Phys. Rev. Appl. **13**(6), 64063 (2020).
[75]P. Liu *et al.*, "Switchable diode effect in 2D van der Waals ferroelectric CuCrP2S6," Appl. Phys. Lett. **124**(9), 091901 (2024).
[76]N. Nuraje and K. Su, "Perovskite ferroelectric nanomaterials," Nanoscale **5**(19), 8752–8780 (2013).
[77]B. Cherdhirunkorn, S. Surakulananta, J. Tangsritrakul, D. Hall, and S. Intarasiri, "The effect of nitrogen ion implantation on the physical and dielectric properties of cobalt-doped PZT ceramics," Results Phys. **16**, 102851 (2020).
[78]Q. Chen *et al.*, "Under the spotlight: The organic–inorganic hybrid halide perovskite for optoelectronic applications," Nano Today **10**(3), 355–396 (2015).
[79]J. Huang, Y. Yuan, Y. Shao, and Y. Yan, "Understanding the physical properties of hybrid perovskites for photovoltaic applications," Nat. Rev. Mater. **2**(7), 17042 (2017).
[80]W. Li, Z. Wang, F. Deschler, S. Gao, R. H. Friend, and A. K. Cheetham, "Chemically diverse and multifunctional hybrid organic–inorganic perovskites," Nat. Rev. Mater. **2**(3), 16099 (2017).
[81]J. M. Frost, K. T. Butler, F. Brivio, C. H. Hendon, M. van Schilfgaarde, and A. Walsh, "Atomistic origins of high-performance in hybrid halide perovskite solar cells," Nano Lett. **14**(5), 2584–2590 (2014).
[82]C. S. Ponseca, Jr. *et al.*, "Organometal halide perovskite solar cell materials rationalized: Ultrafast charge generation, high and microsecond-long balanced mobilities, and slow recombination," J. Am. Chem. Soc. **136**(14), 5189–5192 (2014).
[83]Y. Zhao and K. Zhu, "Organic–inorganic hybrid lead halide perovskites for optoelectronic and electronic applications," Chem. Soc. Rev. **45**(3), 655–689 (2016).
[84]D.-Y. Son *et al.*, "Self-formed grain boundary healing layer for highly efficient CH3NH3PbI3 perovskite solar cells," Nat. Energy **1**(7), 16081 (2016).
[85]Y.-H. Kim *et al.*, "Multicolored organic/inorganic hybrid perovskite light-emitting diodes," Adv. Mater. **27**(7), 1248–1254 (2015).
[86]A. Bulloch, S. Wang, P. Ghosh, and L. K. Jagadamma, "Hysteresis in hybrid perovskite indoor photovoltaics," Philos. Trans. R. Soc. A **380**(2221), 20210144 (2022).
[87]M. Manzi, G. Pica, M. De Bastiani, S. Kundu, G. Grancini, and M. I. Saidaminov, "Ferroelectricity in hybrid perovskites," J. Phys. Chem. Lett. **14**(14), 3535–3552 (2023).
[88]Y. Liu, D. Kim, A. V. Ievlev, S. V. Kalinin, M. Ahmadi, and O. S. Ovchinnikova, "Ferroic halide perovskite optoelectronics," Adv. Funct. Mater. **31**(36), 2102793 (2021).
[89]R. Singh and M. Parashar, *Soft-Matter Thin Film Solar Cells: Physical Processes and Device Simulation* (AIP Publishing, 2020).
[90]M. Vasilopoulou *et al.*, "Neuromorphic computing based on halide perovskites," Nat. Electron. **6**(12), 949–962 (2023).
[91]Z. Fan *et al.*, "Ferroelectricity of CH3NH3PbI3 perovskite," J. Phys. Chem. Lett. **6**(7), 1155–1161 (2015).
[92]G. A. Sewvandi, K. Kodera, H. Ma, S. Nakanishi, and Q. Feng, "Antiferroelectric nature of CH3NH3PbI3−xClx perovskite and its implication for charge separation in perovskite solar cells," Sci. Rep. **6**(1), 30680 (2016).
[93]Y. Kutes, L. Ye, Y. Zhou, S. Pang, B. D. Huey, and N. P. Padture, "Direct observation of ferroelectric domains in solution-processed CH3NH3PbI3 perovskite thin films," J. Phys. Chem. Lett. **5**(19), 3335–3339 (2014).
[94]I. M. Hermes *et al.*, "Ferroelastic fingerprints in methylammonium lead iodide perovskite," J. Phys. Chem. C **120**(10), 5724–5731 (2016).
[95]J. Wei *et al.*, "Hysteresis analysis based on the ferroelectric effect in hybrid perovskite solar cells," J. Phys. Chem. Lett. **5**(21), 3937–3945 (2014).
[96]M. Coll *et al.*, "Polarization switching and light-enhanced piezoelectricity in lead halide perovskites," J. Phys. Chem. Lett. **6**(8), 1408–1413 (2015).
[97]M. T. Weller, O. J. Weber, P. F. Henry, A. M. Di Pumpo, and T. C. Hansen, "Complete structure and cation orientation in the perovskite photovoltaic methylammonium lead iodide between 100 and 352 K," Chem. Commun. **51**(20), 4180–4183 (2015).
[98]G. Sharada, M. Pratibha, P. K. Bhushan *et al.*, S. "Is CH3NH3PbI3 polar?," J. Phys. Chem. Lett. **7**(13), 2412–2419 (2016).
[99]C. Lan *et al.*, "Revealing electrical-poling-induced polarization potential in hybrid perovskite photodetectors," Adv. Mater. **32**(47), 2005481 (2020).
[100]A. Mahapatra *et al.*, "Revealing the variation of photodetectivity in MAPbI3 and MAPb(I0.88Br0.12)3 single crystal based photodetectors under electrical poling-induced polarization," J. Phys. Chem. C **126**(31), 13458–13466 (2022).
[101]H. Röhm, T. Leonhard, M. J. Hoffmann, and A. Colsmann, "Ferroelectric poling of methylammonium lead iodide thin films," Adv. Funct. Mater. **30**(5), 1908657 (2020).
[102]R. Saraf, C. Saguy, V. Maheshwari, H. Elangovan, and Y. Ivry, "Intrinsic-polarization origin of photoconductivity in MAPbI3 thin films," Appl. Phys. Lett. **118**, 151903 (2021).
[103]G. Xia *et al.*, "Nanoscale insights into photovoltaic hysteresis in triple-cation mixed-halide perovskite: Resolving the role of polarization and ionic migration," Adv. Mater. **31**(36), 1902870 (2019).
[104]M. Ahmadi *et al.*, "Exploring anomalous polarization dynamics in organometallic halide perovskites," Adv. Mater. **30**(11), 1705298 (2018).
[105]G. Pica *et al.*, "Photo-ferroelectric perovskite interfaces for boosting VOC in efficient perovskite solar cells," Nat. Commun. **15**(1), 8753 (2024).
[106]J. Beilsten-Edmands, G. E. Eperon, R. D. Johnson, H. J. Snaith, and P. G. Radaelli, "Non-ferroelectric nature of the conductance hysteresis in CH3NH3PbI3 perovskite-based photovoltaic devices," Appl. Phys. Lett. **106**(17), 173502 (2015).
[107]T. Zhang *et al.*, "Understanding the relationship between ion migration and the anomalous hysteresis in high-efficiency perovskite solar cells: A fresh perspective from halide substitution," Nano Energy **26**, 620–630 (2016).
[108]B. Wu *et al.*, "Charge accumulation and hysteresis in perovskite-based solar cells: An electro-optical analysis," Adv. Energy Mater. **5**(19), 1500829 (2015).
[109]J. M. Azpiroz, E. Mosconi, J. Bisquert, and F. De Angelis, "Defect migration in methylammonium lead iodide and its role in perovskite solar cell operation," Energy Environ. Sci. **8**(7), 2118–2127 (2015).
[110]L. Zuo, Z. Li, and H. Chen, "Ion migration and accumulation in halide perovskite solar cells," Chin. J. Chem. **41**(7), 861–876 (2023).
[111]X. Yan *et al.*, "Ion migration in hybrid perovskites: Classification, identification, and manipulation," Nano Today **44**, 101503 (2022).
[112]W. Zhu, S. Wang, X. Zhang, A. Wang, C. Wu, and F. Hao, "Ion migration in organic–inorganic hybrid perovskite solar cells: Current understanding and perspectives," Small **18**(15), 2105783 (2022).
[113]E. T. Hoke, D. J. Slotcavage, E. R. Dohner, A. R. Bowring, H. I. Karunadasa, and M. D. McGehee, "Reversible photo-induced trap formation in mixed-halide hybrid perovskites for photovoltaics," Chem. Sci. **6**(1), 613–617 (2015).
[114]C. Cardenas-Daw, T. Simon, J. K. Stolarczyk, and J. Feldmann, "Migration of constituent protons in hybrid organic–inorganic perovskite triggers intrinsic doping," J. Am. Chem. Soc. **139**(46), 16462–16465 (2017).
[115]N. Vicente and G. Garcia-Belmonte, "Organohalide perovskites are fast ionic conductors," Adv. Energy Mater. **7**(19), 1700710 (2017).
[116]T. Zhang *et al.*, "Profiling the organic cation-dependent degradation of organolead halide perovskite solar cells," J. Mater. Chem. A Mater. **5**(3), 1103–1111 (2017).
[117]L. Liang, Y. Cai, X. Li, M. K. Nazeeruddin, and P. Gao, "All that glitters is not gold: Recent progress of alternative counter electrodes for perovskite solar cells," Nano Energy **52**, 211–238 (2018).
[118]X. Zhu, J. Lee, and W. D. Lu, "Iodine vacancy redistribution in organic–inorganic halide perovskite films and resistive switching effects," Adv. Mater. **29**(29), 1700527 (2017).
[119]C. Eames, J. M. Frost, P. R. F. Barnes, B. C. O'Regan, A. Walsh, and M. S. Islam, "Ionic transport in hybrid lead iodide perovskite solar cells," Nat. Commun. **6**(1), 7497 (2015).

[120]J. Haruyama, K. Sodeyama, L. Han, and Y. Tateyama, "First-principles study of ion diffusion in perovskite solar cell sensitizers," J. Am. Chem. Soc. **137**(32), 10048–10051 (2015).
[121]D. A. Egger, L. Kronik, and A. M. Rappe, "Theory of hydrogen migration in organic–inorganic halide perovskites," Angew. Chem. Int. Ed. **54**(42), 12437–12441 (2015).
[122]M. Bag *et al.*, "Kinetics of ion transport in perovskite active layers and its implications for active layer stability," J. Am. Chem. Soc. **137**(40), 13130–13137 (2015).
[123]E. Mosconi, D. Meggiolaro, H. J. Snaith, S. D. Stranks, and F. De Angelis, "Light-induced annihilation of Frenkel defects in organo-lead halide perovskites," Energy Environ. Sci. **9**(10), 3180–3187 (2016).
[124]D. W. deQuilettes *et al.*, "Photo-induced halide redistribution in organic–inorganic perovskite films," Nat. Commun. **7**(1), 11683 (2016).
[125]Y. Yuan *et al.*, "Electric-field-driven reversible conversion between methylammonium lead triiodide perovskites and lead iodide at elevated temperatures," Adv. Energy Mater. **6**(2), 1501803 (2016).
[126]Y. Feng *et al.*, "Proton migration in hybrid lead iodide perovskites: From classical hopping to deep quantum tunneling," J. Phys. Chem. Lett. **9**(22), 6536–6543 (2018).
[127]Y.-C. Zhao, W.-K. Zhou, X. Zhou, K.-H. Liu, D.-P. Yu, and Q. Zhao, "Quantification of light-enhanced ionic transport in lead iodide perovskite thin films and its solar cell applications," Light Sci. Appl. **6**(5), e16243 (2016).
[128]D. Li, H. Wu, H.-C. Cheng, G. Wang, Y. Huang, and X. Duan, "Electronic and ionic transport dynamics in organolead halide perovskites," ACS Nano **10**(7), 6933–6941 (2016).
[129]T.-Y. Yang, G. Gregori, N. Pellet, M. Grätzel, and J. Maier, "The significance of ion conduction in a hybrid organic–inorganic lead-iodide-based perovskite photosensitizer," Angew. Chem. Int. Ed. **54**(27), 7905–7910 (2015).
[130]C. Li *et al.*, "Iodine migration and its effect on hysteresis in perovskite solar cells," Adv. Mater. **28**(12), 2446–2454 (2016).
[131]S. Meloni *et al.*, "Ionic polarization-induced current–voltage hysteresis in CH3NH3PbX3 perovskite solar cells," Nat. Commun. **7**(1), 10334 (2016).
[132]J. Xing, Q. Wang, Q. Dong, Y. Yuan, Y. Fang, and J. Huang, "Ultrafast ion migration in hybrid perovskite polycrystalline thin films under light and suppression in single crystals," Phys. Chem. Chem. Phys. **18**(44), 30484–30490 (2016).
[133]A. Pockett, G. E. Eperon, N. Sakai, H. J. Snaith, L. M. Peter, and P. J. Cameron, "Microseconds, milliseconds and seconds: Deconvoluting the dynamic behaviour of planar perovskite solar cells," Phys. Chem. Chem. Phys. **19**(8), 5959–5970 (2017).
[134]Z. Xiao *et al.*, "Giant switchable photovoltaic effect in organometal trihalide perovskite devices," Nat. Mater. **14**(2), 193–198 (2015).
[135]Y. Shao *et al.*, "Grain boundary dominated ion migration in polycrystalline organic–inorganic halide perovskite films," Energy Environ. Sci. **9**(5), 1752–1759 (2016).
[136]Y. Yuan *et al.*, "Photovoltaic switching mechanism in lateral structure hybrid perovskite solar cells," Adv. Energy Mater. **5**(15), 1500615 (2015).
[137]C. G. Bischak *et al.*, "Origin of reversible photoinduced phase separation in hybrid perovskites," Nano Lett. **17**(2), 1028–1033 (2017).
[138]H. Tsai *et al.*, "Light-induced lattice expansion leads to high-efficiency perovskite solar cells," Science (1979) **360**(6384), 67–70 (2018).
[139]D. Yang, W. Ming, H. Shi, L. Zhang, and M.-H. Du, "Fast diffusion of native defects and impurities in perovskite solar cell material CH3NH3PbI3," Chem. Mater. **28**(12), 4349–4357 (2016).
[140]C. Zhao, B. Chen, X. Qiao, L. Luan, K. Lu, and B. Hu, "Revealing underlying processes involved in light soaking effects and hysteresis phenomena in perovskite solar cells," Adv. Energy Mater. **5**(14), 1500279 (2015).
[141]D. Moia and J. Maier, "Ion transport, defect chemistry, and the device physics of hybrid perovskite solar cells," ACS Energy Lett. **6**(4), 1566–1576 (2021).
[142]A. Senocrate, E. Kotomin, and J. Maier, "On the way to optoionics," Helv. Chim. Acta **103**(7), e2000073 (2020).
[143]D. Toth *et al.*, "Nanoscale charge accumulation and its effect on carrier dynamics in tri-cation perovskite structures," ACS Appl. Mater. Interfaces **12**(42), 48057–48066 (2020).
[144]X. Li, J. M. Hoffman, and M. G. Kanatzidis, "The 2D halide perovskite rulebook: How the spacer influences everything from the structure to optoelectronic device efficiency," Chem. Rev. **121**(4), 2230–2291 (2021).
[145]S. Han *et al.*, "Visible-photoactive perovskite ferroelectric-driven self-powered gas detection," J. Am. Chem. Soc. **145**(23), 12853–12860 (2023).
[146]Y. Liu *et al.*, "Giant polarization sensitivity via the anomalous photovoltaic effect in a two-dimensional perovskite ferroelectric," J. Am. Chem. Soc. **145**(29), 16193–16199 (2023).
[147]W. Guo *et al.*, "Electrically switchable persistent spin texture in a two-dimensional hybrid perovskite ferroelectric," Angew. Chem. Int. Ed. **62**(17), e202300028 (2023).
[148]F. Jia *et al.*, "Persistent spin-texture and ferroelectric polarization in 2D hybrid perovskite benzylammonium lead-halide," J. Phys. Chem. Lett. **11**(13), 5177–5183 (2020).
[149]W.-Q. Liao *et al.*, "A lead-halide perovskite molecular ferroelectric semiconductor," Nat. Commun. **6**(1), 7338 (2015).
[150]K. Leng, R. Li, S. P. Lau, and K. P. Loh, "Ferroelectricity and Rashba effect in 2D organic–inorganic hybrid perovskites," Trends Chem. **3**(9), 716–732 (2021).
[151]H.-Y. Zhang, Z.-X. Zhang, X.-J. Song, X.-G. Chen, and R.-G. Xiong, "Two-dimensional hybrid perovskite ferroelectric induced by perfluorinated substitution," J. Am. Chem. Soc. **142**(47), 20208–20215 (2020).
[152]H.-Y. Zhang, Z.-X. Zhang, X.-G. Chen, X.-J. Song, Y. Zhang, and R.-G. Xiong, "Large electrostrictive coefficient in a two-dimensional hybrid perovskite ferroelectric," J. Am. Chem. Soc. **143**(3), 1664–1672 (2021).
[153]J. Y. Park *et al.*, "A lead-free ferroelectric 2D Dion–Jacobson tin iodide perovskite," Adv. Mater. **36**(29), 2314292 (2024).
[154]R. S. Muddam and L. K. Jagadamma, "Ferroelectric polarization in 2D halide hybrid perovskites: Influence on bulk crystals, thin films, and applications," J. Mater. Chem. C **13**(21), 10488–10506 (2025).
[155]Y. Hu *et al.*, "A 2D hybrid perovskite ferroelectric with switchable polarization and photoelectric robustness down to monolayer," Nat. Commun. **16**(1), 3028 (2025).
[156]Â. Freitas, M. C. Baptista, and M. H. Braga, "Sustainable solid-state sodium-ion batteries featuring ferroelectric electrolytes," Int. J. Mol. Sci. **25**(23), 12694 (2024).
[157]F. Danzi, P. P. Camanho, and M. H. Braga, "An all-solid-state coaxial structural battery using sodium-based electrolyte," Molecules **26**(17), 5226 (2021).
[158]F. Danzi, M. Valente, S. Terlicka, and M. H. Braga, "Sodium and potassium ion rich ferroelectric solid electrolytes for traditional and electrode-less structural batteries," APL Mater. **10**(3), 031111 (2022).
[159]M. C. Baptista, B. M. Gomes, A. B. Vale, and M. H. Braga, "In-series all-solid-state anode-less cells," J. Energy Storage **102**, 113983 (2024).
[160]B. G. Christoff, D. Marques, J. P. Carmo, M. H. Braga, and V. Tita, "On the strain-sensing capabilities of a novel all-solid-state sodium-based-electrolyte battery under vibration loads," Mech. Syst. Signal Process. **215**, 111390 (2024).
[161]M. C. Baptista *et al.*, "Conditioning solid-state anode-less cells for the next generation of batteries," Batteries **9**(8), 402 (2023).
[162]M. H. Braga, J. A. Ferreira, V. Stockhausen, J. E. Oliveira, and A. El-Azab, "Novel Li_3 ClO based glasses with superionic properties for lithium batteries," J. Mater. Chem. A **2**(15), 5470–5480 (2014).
[163]Z. Lu, C. Chen, Z. M. Baiyee, X. Chen, C. Niu, and F. Ciucci, "Defect chemistry and lithium transport in Li3OCl anti-perovskite superionic conductors," Phys. Chem. Chem. Phys. **17**(48), 32547–32555 (2015).
[164]M. H. Braga, V. Stockhausen, J. C. E. Oliveira, and J. A. Ferreira, "The role of defects in Li3ClO solid electrolyte: Calculations and experiments," MRS Online Proc. Library **1526**(1), 905 (2013).
[165]B. M. Gomes, J. F. R. Moutinho, and M. H. Braga, "A perspective on the building blocks of a solid-state battery: From solid electrolytes to quantum power harvesting and storage," J. Mater. Chem. A Mater. **12**, 690–722 (2024).
[166]C. Chi *et al.*, "Selectively tuning ionic thermopower in all-solid-state flexible polymer composites for thermal sensing," Nat. Commun. **13**(1), 221 (2022).
[167]R. V. Carreón, O. Cortázar-Martínez, A. G. Rodríguez-Hernández, L. E. Serrano de la Rosa, J. J. Gervacio-Arciniega, and S. K. Krishnan, "Ionic liquid-assisted thermal evaporation of bimetallic Ag–Au nanoparticle films as a highly reproducible SERS substrate for sensitive nanoplastic detection in complex environments," Anal. Chem. **96**(15), 5790–5797 (2024).
[168]G. Dushaq, S. Serunjogi, S. R. Tamalampudi, and M. Rasras, "Non-reciprocal response in silicon photonic resonators integrated with 2D CuCrP2S6 at short-wave infrared," Light Sci. Appl. **14**(1), 157 (2025).

[169]G. Dushaq, S. Serunjogi, S. R. Tamalampudi, and M. Rasras, "Electro-optic tuning in composite silicon photonics based on ferroionic 2D materials," Light Sci. Appl. **13**(1), 92 (2024).
[170]J. Liu, L. Su, X. Zhang, D. V. Shtansky, and X. Fang, "Ferroelectric–optoelectronic hybrid system for photodetection," Small Methods **8**(2), 2300319 (2024).
[171]Y. Liu *et al.*, "Linear electro-optic effect in 2D ferroelectric for electrically tunable metalens," Adv. Mater. **36**(29), 2401838 (2024).
[172]Y. Gao, M. Gao, and Y. Lu, "Two-dimensional multiferroics," Nanoscale **13**(46), 19324–19340 (2021).
[173]G. Dushaq, S. Serunjogi, S. R. Tamalampudi, and M. Rasras, "Unlocking electro-optic tuning in hybrid silicon photonics based on ferroionic 2D materials," arXiv:2310.07382 (2023).
[174]G. Cook *et al.*, "Harvesting single ferroelectric domain stressed nanoparticles for optical and ferroic applications," J. Appl. Phys. **108**(6), 064309 (2010).
[175]K. P. Kelley *et al.*, "Thickness and strain dependence of piezoelectric coefficient in $BaTiO_3$ thin films," Phys. Rev. Mater. **4**(2), 24407 (2020).
[176]M. Vasiljevic *et al.*, "'Forbidden' polarisation and extraordinary piezoelectric effect in organometallic lead halide perovskites," Adv. Funct. Mater. **32**(40), 2204898 (2022).
[177]G. Lindgren *et al.*, "Elasticity modulation due to polarization reversal and ionic motion in the ferroelectric superionic conductor KTiOPO4," ACS Appl. Mater. Interfaces **10**(38), 32298–32303 (2018).
[178]A. N. Morozovska *et al.*, "Reentrant polar phase induced by the ferroionic coupling in $Bi_{1-x}Sm_xFeO_3$ nanoparticles," Phys. Rev. B **110**(22), 224110 (2024).
[179]Y. Zhang and Y. Wang, "Nonlinear optical properties of metal nanoparticles: A review," RSC Adv. **7**(71), 45129–45144 (2017).
[180]J. Chen, J. Tan, G. Wu, X. Zhang, F. Xu, and Y. Lu, "Tunable and enhanced light emission in hybrid WS2-optical-fiber-nanowire structures," Light Sci. Appl. **8**(1), 8 (2019).
[181]Z. Li *et al.*, "Versatile optical manipulation of trions, dark excitons and biexcitons through contrasting exciton-photon coupling," Light Sci. Appl. **12**(1), 295 (2023).
[182]X. Hou *et al.*, "Optical evidence of interfacial strain-induced ferroelectric tuning and enhancement in CuInP2S6 via ferroelectric substrate," Small **21**(5), 2409879 (2025).
[183]X. Wang *et al.*, "Electrical and magnetic anisotropies in van der Waals multiferroic CuCrP2S6," Nat. Commun. **14**(1), 840 (2023).
[184]S. Aoki *et al.*, "Giant modulation of the second harmonic generation by magnetoelectricity in two-dimensional multiferroic CuCrP2S6," Adv. Mater. **36**(21), 2312781 (2024).
[185]H. Kalita *et al.*, "Artificial neuron using vertical MoS2/graphene threshold switching memristors," Sci. Rep. **9**(1), 53 (2019).
[186]Y. Zhao *et al.*, "Memristor based on α-In2Se3 for emulating biological synaptic plasticity and learning behavior," Sci. China Mater. **65**(6), 1631–1638 (2022).
[187]K. Sun, J. Chen, and X. Yan, "The future of memristors: Materials engineering and neural networks," Adv. Funct. Mater. **31**(8), 2006773 (2021).
[188]W. Tress, "Metal halide perovskites as mixed electronic–ionic conductors: Challenges and opportunities—From hysteresis to memristivity," J. Phys. Chem. Lett. **8**(13), 3106–3114 (2017).
[189]C. Li *et al.*, "Real-Time observation of iodide ion migration in methylammonium lead halide perovskites," Small **13**(42), 1701711 (2017).
[190]G. Y. Kim, A. Senocrate, T.-Y. Yang, G. Gregori, M. Grätzel, and J. Maier, "Large tunable photoeffect on ion conduction in halide perovskites and implications for photodecomposition," Nat. Mater. **17**(5), 445–449 (2018).
[191]X. Zhao, H. Xu, Z. Wang, Y. Lin, and Y. Liu, "Memristors with organic-inorganic halide perovskites," InfoMat **1**(2), 183–210 (2019).
[192]A. Abnavi *et al.*, "Free-standing multilayer molybdenum disulfide memristor for brain-inspired neuromorphic applications," ACS Appl. Mater. Interfaces **13**(38), 45843–45853 (2021).
[193]X. Yan *et al.*, "Vacancy-induced synaptic behavior in 2D WS2 nanosheet–based memristor for low-power neuromorphic computing," Small **15**(24), e1901423 (2019).
[194]Y. Zhang, L. Wang, H. Chen, T. Ma, X. Lu, and K. P. Loh, "Analog and digital mode α-In2Se3 memristive devices for neuromorphic and memory applications," Adv. Electron. Mater. **7**(12), 2100609 (2021).
[195]Z. Li *et al.*, "Ferroelectric switching behavior in two-dimensional semiconductor α-In2Se3 for nonvolatile memory," ACS Appl. Electron. Mater. **6**(4), 2507–2513 (2024).
[196]J. Chen *et al.*, "Mimicking neuroplasticity via ion migration in van der Waals layered copper indium thiophosphate," Adv. Mater. **34**(25), 2104676 (2022).
[197]Y. Liu *et al.*, "Versatile memristor implemented in van der Waals CuInP2S6," Nano Res. **16**(7), 10191–10197 (2023).
[198]J. C. Pérez-Martínez, D. Martín-Martín, B. Arredondo, and B. Romero, "Unraveling conductive filament formation in high performance halide perovskite memristor," Adv. Electron. Mater. **10**(9), 2400067 (2024).
[199]H. Patil *et al.*, "Flexible organic–inorganic halide perovskite-based diffusive memristor for artificial nociceptors," ACS Appl. Mater. Interfaces **15**(10), 13238–13248 (2023).
[200]J. Wu *et al.*, "High tunnelling electroresistance in a ferroelectric van der Waals heterojunction via giant barrier height modulation," Nat. Electron. **3**(8), 466–472 (2020).
[201]S. H. Park, H. J. Lee, M. H. Park, J. Kim, and H. W. Jang, "Ferroelectric tunnel junctions: Promise, achievements and challenges," J. Phys. D: Appl. Phys. **57**(25), 253002 (2024).
[202]Q. Wang *et al.*, "Extraordinary tunnel electroresistance in layer-by-layer engineered van der Waals ferroelectric tunnel junctions," Matter **5**(12), 4425–4436 (2022).
[203]Y. Luo *et al.*, "Robust giant tunnel electroresistance and negative differential resistance in 2D semiconductor/α-In2Se3 ferroelectric tunnel junctions," Adv. Funct. Mater. **34**(34), 2407253 (2024).
[204]X. Lin, X. Huang, Q. Zhang, J. Yi, S. Liu, and Q. Liang, "Two-dimensional van der Waals ferroelectric field-effect transistors toward nonvolatile memory and neuromorphic computing," Appl. Phys. Lett. **123**(18), 180501 (2023).
[205]S. Baek *et al.*, "Ferroelectric field-effect-transistor integrated with ferroelectrics heterostructure," Adv. Sci. **9**(21), 2200566 (2022).
[206]A. Lipatov, P. Sharma, A. Gruverman, and A. Sinitskii, "Optoelectrical molybdenum disulfide (MoS2)—Ferroelectric memories," ACS Nano **9**(8), 8089–8098 (2015).
[207]M. Si, P.-Y. Liao, G. Qiu, Y. Duan, and P. D. Ye, "Ferroelectric field-effect transistors based on MoS2 and CuInP2S6 two-dimensional van der Waals heterostructure," ACS Nano **12**(7), 6700–6705 (2018).
[208]W. Park *et al.*, "Characteristics of a pressure sensitive touch sensor using a piezoelectric PVDF-TrFE/MoS2 stack," Nanotechnology **24**(47), 475501 (2013).
[209]M. Park, Y. J. Park, X. Chen, Y.-K. Park, M.-S. Kim, and J.-H. Ahn, "MoS2-based tactile sensor for electronic skin applications," Adv. Mater. **28**(13), 2556–2562 (2016).
[210]Y. J. Park *et al.*, "All MoS2-based large area, skin-attachable active-matrix tactile sensor," ACS Nano **13**(3), 3023–3030 (2019).
[211]M. Dai *et al.*, "enhanced piezoelectric effect derived from grain boundary in MoS2 monolayers," Nano Lett. **20**(1), 201–207 (2020).
[212]J. Jang *et al.*, "Mechanoluminescent, air-dielectric MoS2 transistors as active-matrix pressure sensors for wide detection ranges from footsteps to cellular motions," Nano Lett. **20**(1), 66–74 (2020).
[213]S. Veeralingam, P. Sahatiya, and S. Badhulika, "Papertronics: Hand-written MoS_2 on paper based highly sensitive and recoverable pressure and strain sensors," IEEE Sens. J. **21**(7), 8943–8949 (2021).
[214]X. Chen, D. Zhang, H. Luan, C. Yang, W. Yan, and W. Liu, "Flexible pressure sensors based on molybdenum disulfide/hydroxyethyl cellulose/polyurethane sponge for motion detection and speech recognition using machine learning," ACS Appl. Mater. Interfaces **15**(1), 2043–2053 (2023).
[215]S. Bin Choi *et al.*, "Rapid-response hybrid piezo-triboelectric pressure sensor using all-fabric materials for enhanced sensing and power generation," Nano Energy **140**, 111000 (2025).
[216]N. Bokka, N. J. Singh, C. S. R. Kolli, and P. Sahatiya, "Highly transient and recyclable MoS2/PVA pressure sensor for sustainable healthcare and consumer electronic applications," J. Mater. Chem. C Mater. **13**(21), 10804–10816 (2025).
[217]Y. Yang *et al.*, "Flexible piezoelectric pressure sensor based on polydopamine-modified BaTiO3/PVDF composite film for human motion monitoring," Sens. Actuators A Phys. **301**, 111789 (2020).

[218]J. Luo *et al.*, "Flexible electronic skin with high performance pressure sensing based on PVDF/rGO/BaTiO3 composite thin film," Org. Electron. **98**, 106296 (2021).
[219]C.-R. Yang, M.-F. Lin, C.-K. Huang, W.-C. Huang, S.-F. Tseng, and H.-H. Chiang, "Highly sensitive and wearable capacitive pressure sensors based on PVDF/BaTiO3 composite fibers on PDMS microcylindrical structures," Measurement **202**, 111817 (2022).
[220]Y. He, Y. Huang, R. Xue, Q. Shi, Y. Wu, and R. Liu, "Flexible pressure sensor based on multi-layer with gradient structure P(VDF-HFP)/MXene/BaTiO3 composite film for human motion monitoring," Diam. Relat. Mater. **140**, 110536 (2023).
[221]X. Liu *et al.*, "BaTiO3/MXene/PVDF-TrFE composite films via an electrospinning method for flexible piezoelectric pressure sensors," J. Mater. Chem. C Mater. **11**(14), 4614–4622 (2023).
[222]J. Wang *et al.*, "Boosting sensing performance of flexible piezoelectric pressure sensors by Sb nanosheets and BaTiO3 nanoparticles co-doping in P(VDF-TrFE) nanofibers mat," Adv. Electron. Mater. **10**(4), 2300718 (2024).
[223]S. Mirjalali *et al.*, "Enhanced piezoelectricity of PVDF-TrFE nanofibers by intercalating with electrosprayed BaTiO3," ACS Appl. Mater. Interfaces **15**(35), 41806–41816 (2023).
[224]J. Yu *et al.*, "Synergistic piezoelectricity enhanced BaTiO3/polyacrylonitrile elastomer-based highly sensitive pressure sensor for intelligent sensing and posture recognition applications," Nano Res. **16**(4), 5490–5502 (2023).
[225]A. I. Madbouly, W. S. Hassanien, and M. Morsy, "Tailoring the polyurethane foam/rGO/BaTiO3 pressure sensor for human activities," Diam. Relat. Mater. **136**, 109940 (2023).
[226]W. Wu *et al.*, "Piezoelectricity of single-atomic-layer MoS2 for energy conversion and piezotronics," Nature **514**(7523), 470–474 (2014).
[227]W. Wu *et al.*, "Piezophototronic effect in single-atomic-layer MoS2 for strain-gated flexible optoelectronics," Adv. Mater. **28**(38), 8463–8468 (2016).
[228]S. K. Kim *et al.*, "Directional dependent piezoelectric effect in CVD grown monolayer MoS2 for flexible piezoelectric nanogenerators," Nano Energy **22**, 483–489 (2016).
[229]W. Choi, J. Kim, E. Lee, G. Mehta, and V. Prasad, "Asymmetric 2D MoS2 for scalable and high-performance piezoelectric sensors," ACS Appl. Mater. Interfaces **13**(11), 13596–13603 (2021).
[230]S. A. Han *et al.*, "Point-defect-passivated MoS2 nanosheet-based high performance piezoelectric nanogenerator," Adv. Mater. **30**(21), 1800342 (2018).
[231]S. Cao, H. Zou, B. Jiang, M. Li, and Q. Yuan, "Incorporation of ZnO encapsulated MoS2 to fabricate flexible piezoelectric nanogenerator and sensor," Nano Energy **102**, 107635 (2022).
[232]Y. Huang *et al.*, "Synergetic effect of MXene/MoS2 heterostructure and gradient multilayer for highly sensitive flexible piezoelectric sensor," Polym. (Guildf) **286**, 126399 (2023).
[233]M.-Y. Tsai *et al.*, "Flexible MoS2 Field-effect transistors for gate-tunable piezoresistive strain sensors," ACS Appl. Mater. Interfaces **7**(23), 12850–12855 (2015).
[234]W. Zheng *et al.*, "Kirigami-inspired highly stretchable nanoscale devices using multidimensional deformation of monolayer MoS2," Chem. Mater. **30**(17), 6063–6070 (2018).
[235]A. Chhetry, M. Sharifuzzaman, H. Yoon, S. Sharma, X. Xuan, and J. Y. Park, "MoS2-decorated laser-induced graphene for a highly sensitive, hysteresis-free, and reliable piezoresistive strain sensor," ACS Appl. Mater. Interfaces **11**(25), 22531–22542 (2019).
[236]S. Sridhar, S. Sebastian, A. K. Sood, and S. Asokan, "A study on MoS_2 nanolayer coated etched fiber Bragg grating strain sensor," IEEE Sens. J. **21**(7), 9171–9178 (2021).
[237]V. Rana *et al.*, "A highly sensitive wearable flexible strain sensor based on polycrystalline MoS2 thin film," Nanotechnology **31**(38), 385501 (2020).
[238]P. Puneetha *et al.*, "Strain-engineered piezotronic effects in flexible monolayer MoS2 continuous thin films," Nano Energy **103**, 107863 (2022).
[239]S. A. Bhakhar, M. Tannarana, P. M. Pataniya, N. F. Patel, B. Chauhan, and G. K. Solanki, "Flexible paper-based piezo-resistive sensor functionalized by MoS2 nanosheets," J. Mater. Sci.: Mater. Electron. **34**(11), 994 (2023).
[240]Q. Xu *et al.*, "WS2/CsPbBr3 van der Waals heterostructure planar photodetectors with ultrahigh on/off ratio and piezo-phototronic effect-induced strain-gated characteristics," Nano Energy **65**, 104001 (2019).
[241]J.-H. Lee *et al.*, "Reliable piezoelectricity in bilayer WSe2 for piezoelectric nanogenerators," Adv. Mater. **29**(29), 1606667 (2017).
[242]W. Feng *et al.*, "Sensitive electronic-skin strain sensor array based on the patterned two-dimensional α-In2Se3," Chem. Mater. **28**(12), 4278–4283 (2016).
[243]M. Dai *et al.*, "Two-dimensional van der Waals materials with aligned in-plane polarization and large piezoelectric effect for self-powered piezoelectric sensors," Nano Lett. **19**(8), 5410–5416 (2019).
[244]P. Hou *et al.*, "In-plane strain-modulated photoresponsivity of the α-In2Se3-based flexible transistor," ACS Appl. Electron. Mater. **2**(1), 140–146 (2020).
[245]Y. Zhao *et al.*, "Piezo-phototronic effect in 2D α-In2Se3/WSe2 van der Waals heterostructure for photodetector with enhanced photoresponse," Adv. Opt. Mater. **9**(20), 2100864 (2021).
[246]E. Moisello, P. Malcovati, and E. Bonizzoni, "Thermal sensors for contactless temperature measurements, occupancy detection, and automatic operation of appliances during the COVID-19 pandemic: A review," Micromachines (Basel) **12**(2), 148 (2021).
[247]Y. Yang, S. Wang, Y. Zhang, and Z. L. Wang, "Pyroelectric nanogenerators for driving wireless sensors," Nano Lett. **12**(12), 6408–6413 (2012).
[248]Y. Yang, Y. Zhou, J. M. Wu, and Z. L. Wang, "Single micro/nanowire pyroelectric nanogenerators as self-powered temperature sensors," ACS Nano **6**(9), 8456–8461 (2012).
[249]Y. J. Ko *et al.*, "Flexible Pb(Zr0.52Ti0.48)O3 films for a hybrid piezoelectric-pyroelectric nanogenerator under harsh environments," ACS Appl. Mater. Interfaces **8**(10), 6504–6511 (2016).
[250]H. Zhang *et al.*, "Single-electrode-based rotating triboelectric nanogenerator for harvesting energy from tires," ACS Nano **8**(1), 680–689 (2014).
[251]A. Bora, L. P. L. Mawlong, and P. K. Giri, "Highly suppressed dark current and fast photoresponse from Au nanoparticle-embedded, Si/Au/WS2 quantum-dot-based, self-biased schottky photodetectors," ACS Appl. Electron. Mater. **3**(11), 4891–4904 (2021).
[252]Y. Yang *et al.*, "Pyroelectric nanogenerators for harvesting thermoelectric energy," Nano Lett. **12**(6), 2833–2838 (2012).
[253]P. Sehrawat and S. S. Islam, "Gel-cast—A promising technique to develop highly sensitive temperature sensor," Mater. Res. Bull. **80**, 72–79 (2016).
[254]F. Khan, Abid, P. Sehrawat, C. M. Julien, and S. S. Islam, "External boosting of free carriers and phonon energy in MoS2/reduced graphene oxide nanosheet-based composite films: Implications for thermal management," ACS Appl. Nano Mater. **6**(1), 96–109 (2023).
[255]H. S. Lee *et al.*, "MoS2 nanosheet phototransistors with thickness-modulated optical energy gap," Nano Lett. **12**(7), 3695–3700 (2012).
[256]C. Lee, H. Yan, L. E. Brus, T. F. Heinz, J. Hone, and S. Ryu, "Anomalous lattice vibrations of single- and few-layer MoS2," ACS Nano **4**(5), 2695–2700 (2010).
[257]Abid, P. Sehrawat, S. S. Islam, P. Mishra, and S. Ahmad, "Reduced graphene oxide (rGO) based wideband optical sensor and the role of temperature, defect states and quantum efficiency," Sci. Rep. **8**(1), 3537 (2018).
[258]P. Sehrawat, Abid, S. S. Islam, and P. Mishra, "Reduced graphene oxide based temperature sensor: Extraordinary performance governed by lattice dynamics assisted carrier transport," Sens. Actuators B Chem. **258**, 424–435 (2018).
[259]T. Q. Trung, S. Ramasundaram, B.-U. Hwang, and N.-E. Lee, "An all-elastomeric transparent and stretchable temperature sensor for body-attachable wearable electronics," Adv. Mater. **28**(3), 502–509 (2016).
[260]Abid, P. Sehrawat, C. M. Julien, and S. S. Islam, "WS2 quantum dots on e-textile as a wearable UV photodetector: How well reduced graphene oxide can serve as a carrier transport medium?," ACS Appl. Mater. Interfaces **12**(35), 39730–39744 (2020).
[261]J. Peng, W. R. Deskins, M. H. Braga, and A. El-Azab, "Effect of electron–phonon coupling on thermal transport in metals: A Monte Carlo approach for solving the coupled electron–phonon Boltzmann transport equation," AIP Adv. **15**(2), 025108 (2025).
[262]M. Lee, A. Mazaheri, H. S. J. van der Zant, R. Frisenda, and A. Castellanos-Gomez, "Drawing WS2 thermal sensors on paper substrates," Nanoscale **12**(43), 22091–22096 (2020).
[263]T. Dinh, H.-P. Phan, D. V. Dao, P. Woodfield, A. Qamar, and N.-T. Nguyen, "Graphite on paper as material for sensitive thermoresistive sensors," J. Mater. Chem. C Mater. **3**(34), 8776–8779 (2015).
[264]Y. Xu *et al.*, "Laser-induced graphene for bioelectronics and soft actuators," Nano Res. **14**(9), 3033–3050 (2021).

[265]T. Dinh *et al.*, "Solvent-free fabrication of biodegradable hot-film flow sensor for noninvasive respiratory monitoring," J. Phys. D Appl. Phys. **50**(21), 215401 (2017).
[266]T. Dinh *et al.*, "Environment-friendly carbon nanotube based flexible electronics for noninvasive and wearable healthcare," J. Mater. Chem. C Mater. **4**(42), 10061–10068 (2016).
[267]E. Faella *et al.*, "Electric transport properties in few-layers WTe2 field effect transistors affected by temperature," in *Proceedings of the IEEE Nanotechnology Materials and Devices Conference (NMDC)* (IEEE, 2023), pp. 553–557.
[268]A. Kumar and D. Mandal, "2D-pyroelectric materials for waste thermal energy harvesting and beyond," Adv. Energy Mater. **14**(42), 2403319 (2024).
[269]D. Qiu and P. Hou, "Ferroelectricity-driven self-powered weak temperature and broadband light detection in MoS2/CuInP2S6/WSe2 van der Waals heterojunction nanoarchitectonics," ACS Appl. Mater. Interfaces **15**(51), 59671–59680 (2023).
[270]K. Parida, H. Bark, and P. S. Lee, "Emerging thermal technology enabled augmented reality," Adv. Funct. Mater. **31**(39), 2007952 (2021).
[271]K. Zhang, S. Wang, and Y. Yang, "A one-structure-based piezo-tribo-pyro-photoelectric effects coupled nanogenerator for simultaneously scavenging mechanical, thermal, and solar energies," Adv. Energy Mater. **7**(6), 1601852 (2017).
[272]X. Yu *et al.*, "Ferroelectric Nanomaterials for energy harvesting and self-powered sensing applications," Adv. Sensor Res. **3**(12), 2400049 (2024).
[273]Y. Ji, S. Yin, Y. Liu, C. R. Bowen, and Y. Yang, "Dual-mode temperature sensor based on ferroelectric Bi0.5Na0.5TiO3 materials for robotic tactile perception," Nano Energy **128**, 109982 (2024).
[274]S. Yakunin *et al.*, "High-resolution remote thermometry and thermography using luminescent low-dimensional tin-halide perovskites," Nat. Mater. **18**(8), 846–852 (2019).
[275]O. Nazarenko *et al.*, "Guanidinium and mixed cesium–guanidinium tin(II) bromides: Effects of quantum confinement and out-of-plane octahedral tilting," Chem. Mater. **31**(6), 2121–2129 (2019).
[276]A. Bhandari, C. Barsi, and R. Raskar, "Blind and reference-free fluorescence lifetime estimation via consumer time-of-flight sensors," Optica **2**(11), 965–973 (2015).
[277]D. D.-U. Li *et al.*, "Time-domain fluorescence lifetime imaging techniques suitable for solid-state imaging sensor arrays," Sensors **12**(5), 5650–5669 (2012).
[278]K. S. Burch, D. Mandrus, and J.-G. Park, "Magnetism in two-dimensional van der Waals materials," Nature **563**(7729), 47–52 (2018).
[279]V. Rouco *et al.*, "Ferroionic inversion of spin polarization in a spin-memristor," APL Mater. **9**(3), 031110 (2021).
[280]V. O. Jimenez *et al.*, "A magnetic sensor using a 2D van der Waals ferromagnetic material," Sci. Rep. **10**(1), 4789 (2020).
[281]Y. Wang *et al.*, "Strain-sensitive magnetization reversal of a van der Waals magnet," Adv. Mater. **32**(42), 2004533 (2020).
[282]A. Gottscholl *et al.*, "Spin defects in hBN as promising temperature, pressure and magnetic field quantum sensors," Nat. Commun. **12**(1), 4480 (2021).
[283]X. Gao *et al.*, "Nanotube spin defects for omnidirectional magnetic field sensing," Nat. Commun. **15**(1), 7697 (2024).